ABSTRACT

Title of dissertation: NONEQUILIBRIUM MANYBODY
DYNAMICS WITH ULTRACOLD ATOMS
IN OPTICAL LATTICES
AND SELECTED PROBLEMS
IN ATOMIC PHYSICS

Roger Brown, Doctor of Philosophy, 2014

Dissertation directed by: Dr. J.V. Porto and Professor S.L. Rolston
Joint Quantum Institute,
National Institute of Standards and Technology
and
University of Maryland Department of Physics

This thesis is a collection of three separate projects ordered according to the historical development of atomic physics, covering first spectroscopy, then laser cooling, and finally the exploration of quantum dynamics of many-particle states of ultra-cold atoms in optical lattices. We begin with a description of the theory of atomic line shapes with unresolvable hyperfine structure. We apply this theory to experimentally measured spectra of the Lithium D lines and report improved determination of the absolute transition frequencies and an improved bound of the difference in ^{6}Li-^{7}Li nuclear charge radius. We then discuss multi-photon processes in laser cooling and report experimental implementation of multi-photon laser cooling and magneto optical trapping using short lived excited to excited transitions in ^{133}Cs. We present a theoretical proposal to laser cool (Anti-) Hydrogen using a Doppler selective 1S-2S excitation and the Sisyphus effect on the 2S-3P transition.

Finally, we detail the construction and operation of an ultracold ^{87}Rb apparatus with a double well optical lattice. We use this lattice to prepare excited many-body states with Néel antiferromagnetic order and to study the resulting non-equilibrium magnetization dynamics. We observe regimes where the dynamics is dominated by superexchange mediated magnetic interactions.

NONEQUILIBRIUM MANYBODY DYNAMICS WITH ULTRACOLD ATOMS IN OPTICAL LATTICES AND SELECTED PROBLEMS IN ATOMIC PHYSICS

by

Roger Charles Brown

Dissertation submitted to the Faculty of the Graduate School of the
University of Maryland, College Park in partial fulfillment
of the requirements for the degree of
Doctor of Philosophy
2014

Advisory Committee:
Adjunct Professor J. V. Porto, Co-Chair
Professor Steve Rolston, Co-Chair
Professor Chris Monroe
Adjunct Professor Ian B. Spielman
Professor Millard Alexander

Foreword

"What these graduate students always do with my problems, if I turn them over to them, is either to spoil the problem for me because they haven't the capacity to handle it as I want it handled ... or ... they get good results and at once begin to think the problem is theirs instead of mine, when in fact knowing what kind of a problem it is worthwhile to attack is in general more important than the mere carrying out of the necessary steps."

-A. A. Michelson as recalled by R. A. Millikan in Reingold N., *Science in Nineteenth Century America* (New York: Hill and Wang, 1964)

Dedication

To Richard and Judy Brown.

Acknowledgments

I'd like to thank my advisor, Trey Porto for all of the opportunities he provided me through the years. He has been a fine example as a researcher and I have grown to enjoy his hands off, but duty-cycle-modulated, approach to lab management. I can also credit him with convincing me to keep up with the news, even if I haven't made it to NPR.

I would like to thank the thermodynamic limit of excellent post-docs with whom I have had the pleasure of working directly: Jamie Williams for creating a research shallow end into which I could wade; Ippei Danshita for encouragement and discussions; Ludwig Mathey for always having time to talk about problem selection and correlation functions; Rafel Pooser for guidance in tapered amplifier construction; Saijun Wu for being the perfect intermediary between theory and experiment, sharing his work ethic and passion for laser cooling; Steve Olmschenk for being my guide into experimental construction (from tightening vacuum bolts to programing FPGA's); Karl Nelson for practical guidance in all matters of construction; Martin Zelan for showing me how hard one should push for results once there is an appratus, opto-mechanics excellence, and good times camping; Bob Wylie for being the set of measure zero able to debate the relative merits of Henry Rowland's achievements versus those of Henry Rollins (and infinite lab view programming); David Norris for alerting me to the fact that I should graduate after 7 years; Silvio Koller for all of his early mornings (and of course optics design knowledge); Michael Foss-Feig for his theory support (and paper torture snacks); and finally Elizabeth Goldschmidt

for being a constant driving force towards project completion.

I would also like to thank my collaborators in the atomic spectroscopy group; Craig Sansonetti, John Gillaspy, Clayton Simien, Joseph Tan, and Sam Brewer for being so kind with their time and allowing me broaden my atomic physics horizons.

I would be remiss in my duties if I did not thank the important senior people. I appreciate Bill Phillips for teaching me about scientific writing in the form paper torture and about asking questions in the form of all the time. I have benefited immensely from the brain trust of the central committee including Kris Helmerson, Paul Lett, Gretchen Campbell, and I am particularly indebted to Ian Spielman who could turn even the most boring of my half-questions into meaningful discussions of physics. I thank Steve Rolston for assuming UMD paper work responsibility for me despite my vanishing UMD physical presence. I must thank Charles Clark and Mike Coplan for bringing me to NIST and the University of Maryland. I would also like to thank Catherine Gebbie for creating a wonderful NIST laboratory environment including semiannual hams.

Shout outs to fellow laser-coolers: Neil Vladimir Corzo-Trejo, Karina Jimenez-Garcia, Lucas Beguin, Ross Williams, Lindsay LeBlanc, Yu-Ju Lin, Seiji Sugawa, Matt Beeler, Dina Genkina, Lauren Aycock, Paco y Marcell Gall, Ben Stuhl, Hsin-I Lu, Nathan Lundblad, Ryan Glasser, Uli Vogl, Jeremy Clark, Prasoon Gupta, Meng Chang, Quentin Glorieux, Brian Anderson from the University of Arizona (no not that one), Travis Horrom, Heywon Pechkis, Arne Schwettmann, Paul Griffin, Jonathan Wrubel, Kevin Wright, Brad Blakestad, Fred Jendrzejewski, Stephen Eckel, Avinash Kumar, and Tian Lee.

Mom, Julie, Lalo and Abby ♡.

Table of Contents

List of Tables

List of Figures

List of Abbreviations

AOM	acousto-optic modulator
BEC	Bose-Einstein Condensate
DD	Dynamical Decoupling
DDS	direct digital synthesizer
EOM	electro-optic modulator
FPGA	field programmable gate array
JQI	Joint Quantum Institute
MBR	Monolithic Block Resonator
MI	Mott insulator
MOT	Magneto-Optical Trap
NIST	National Institute of Standards and Technology
PC	Pockels Cell
PLL	phase locked loop
RF	radio frequency
SF	super fluid
TEBD	time evolving block decimation
TTL	transistor-transistor logic
UHV	ultra-high vacuum

Chapter 1: Introduction

As a Ph.D. student at the University of Maryland, I worked in the lab of Trey Porto, as part of the laser cooling group, at the National Institute of Standards and Technology (NIST) in Gaithersburg Maryland from 2009 to 2014. From 2010 to 2013, I also collaborated with the laser spectroscopy group. My research in atomic physics was divided into three distinct projects: I will summarize them with extra emphasis on my final project which was the construction and operation of an experiment using Bose-Einstein condensates in optical lattices as a quantum simulator of many-body dynamics.

High resolution optical spectroscopy of atoms has long contributed to nuclear physics, from the optical discovery of deuterium in 1932 [1] to the present discrepancy between the proton charge radius inferred from muonic-hydrogen and electronic hydrogen [2]. My collaboration with the atomic spectroscopy group began with a series of discrepant measurements in atomic Lithium where the transition frequencies were measured with a suitable precision to infer the difference in nuclear charge radius between ^{6}Li and ^{7}Li. The measurements revealed a transition frequency that apparently changed with the polarization of the light used to probe it. We noted that the hyperfine structure of atomic lithium is of the order the natural linewidth of

the transition, thus the excited state of atomic lithium realizes a frequency domain version of the double slit experiment where multiple excitation and decay paths cannot be distinguished. Preforming a perturbative analysis of a single excitation-decay process though all possible paths revealed a polarization dependent matrix element which allowed us to quantitatively model the observed spectra. This systematic effect had not previously been accounted for and resolves the discrepancy between theory and experiment, enabling a more reliable extraction of the difference in nuclear charge radius between ^{6}Li and ^{7}Li (see [3,4] and [5,6] for details).

Laser cooling is a well-established field with many milestone achievements including; Doppler cooling of trapped ions, sub-Doppler cooling and Magneto-optical trapping (MOT) of neutral atoms, and recently laser cooling to quantum degeneracy. The general principle of laser cooling is the transfer of momentum from photons to the center of mass motion of atoms. Gas phase alkali atoms have approximately ten thousand times more momentum than the photons that they most strongly absorb. This disparity in momenta focused most initial research on ground to excited state transitions where angular momentum selection rules allow the atoms to scatter many photons while returning to the same initial state. Our research focused on using short-lived excited states for laser cooling. This was motivated by a desire to improve detection of single laser cooled atoms, which has applications in quantum gas microscopy as well as measuring the concentrations of rare radioactive isotopes using atom trap trace analysis. The concept was to apply multiple colors of cooling light to single atoms and observe fluorescence at another, distinct wavelength not used in cooling. Using this process, atomic detection by florescence would have no

background from stray cooling light.

In our initial studies we applied two wavelengths of cooling light. In a modification of a standard six beam MOT, we replaced the typical ground to excited state cooling and trapping light (on the $6S_{1/2} \rightarrow 6P_{3/2}$ in cesium) with light coupling two excited states (the $6P_{3/2}$ and $8S_{1/2}$) along the $\hat{z}$ direction of our trap. This process required stepwise two-photon excitation to achieve cooling and trapping in the $\hat{z}$ direction. Unexpectedly, we found the polarization of the light required to trap the atoms to be reversed from the standard MOT configuration, which can be understood with a simple model. At higher excited to excited state intensity, we were able to observe a novel 2n + 1 photon cooling process where a single ground to excited state photon allowed the atoms to experience a stimulated 2n photon process due to multiple scattering of excited state photons before decay. This process is remarkable in that it works on both sides of two-photon resonance as opposed to only on the low frequency side of single photon resonance. These studies are reported in [7].

The success of our proof of concept experiment in cesium encouraged us to consider other open problems in laser cooling, especially the laser cooling of trapped anti-hydrogen. The standard theory of laser cooling using the 1S to 2P transition demands a technically challenging vacuum-ultra-violet laser and requires hours to cool to mK temperatures. Using a two photon Doppler selective excitation between 1S and 2S and applying dressing light from the 2S to the 3P creates a large volume for excited state Sisyphus cooling thereby decreasing the total cooling time from hours to 100s of ms and simplifies the required laser system. This proposal is detailed in [8].

My main project in graduate school was on the construction and operation of an experiment to study quantum many-body dynamics. This work aspires to realize Feynman's grand vision of quantum simulators where well-controlled quantum systems are engineered to behave in the same manner as theoretically intractable or experimentally difficult to control systems. In our case, ultracold atoms in an optical lattice are designed to mimic spins in a quantum magnet.

In the experiment we create a Bose-Einstein condensate (BEC) of ^{87}Rb by laser cooling in a standard six beam MOT, followed by evaporative cooling to degeneracy in a magnetic and then optical trap. We then load a three dimensional optical lattice with the atom number chosen such that one atom is loaded per lattice site. This unit filling is confirmed by high resolution microwave spectroscopy of a set of magnetically insensitive states. By changing the lattice beam polarization, the lattice can be staggered in a two-dimensional internal-state-dependent checkerboard pattern allowing atoms on one sub lattice (all black sites on the checkerboard) to be spin flipped. This prepares a Néel ordered anti-ferromagnetic state. We then turn off the internal-state-dependent tilt on black sites and apply an internal-state-independent offset on all red sites. This sublattice offset, if large enough, suppresses tunneling between sites leaving the spins in an energetically excited state where they are not able to release their energy by direct tunneling. We then allow the system to evolve from this initial state for a variable period of time and readout the spin and sublattice populations.

We observe a decay of the initial well-defined spin order. By carefully controlling the atom number and temperature as well as the lattice frequency, amplitude,

and polarization, we can control the underlying Hamiltonian governing the decay dynamics. The Bose-Hubbard Hamiltonian, a celebrated minimal model of strongly correlated Bosons, has three distinct parameters; a tunneling energy J, an onsite interaction U, and a sublattice dependent energy offset Δ. Remarkably, the decay time scale of the initial spin order scales with the inverse of the super exchange energy $J^2U/(\Delta^2 - U^2)$. Super exchange is a second order virtual process where atoms lower their energy by first tunneling to an intermediate state with two atoms on a site, undergoing an onsite interaction, and then tunneling back with their spins flipped relative to the initial configuration. Such a process is believed to be responsible for ferromagnetism in numerous materials but the dynamics of superexchange processes remain largely unexplored. (Publication of apparatus development for this work is reported in [9] additionally, a summary of our experimental observations has been submitted [10] and is contained in chapter 7.)

Chapter 2:   Laser Spectroscopy of Atomic Li

High precision spectroscopy, one of the earliest atomic experiments, still provides data that shapes our understanding of physics, from tests of fundamental symmetries, to atomic clocks, to the determination of nuclear charge radii. In this chapter, we examine one of the most conceptually foundational atomic physics experiments, where a tunable single frequency laser is scanned across an atomic resonance and the amount of scattered light is recorded (see [11, 12] and references therein). The system we study is atomic Lithium. Improved spectroscopy of the Li D lines is of broad interest in physics because the isotope shift of these lines serves as a nuclear-model-independent method to measure relative nuclear charge radii, which are especially interesting in the neutron rich ^{8,9,11}Li [13]. Measured isotope shifts for the lithium 2s-2p (D lines) [14–18] or 2s-3s [19–22] transitions can be combined with precise theoretical calculations [13, 23, 24] to determine relative nuclear charge radii of lithium isotopes. Additionally, measured D-line transition frequencies are used as input for the calculation of species-specific "tune in/out" optical lattices for mixtures of quantum degenerate gases [25–27]. While systematics associated with motional and external field shifts have long been understood and removed or reduced, surprisingly, we find a long overlooked systematic due to interference ef-

fects in light scattering that impact a range of experiments. This interference effect makes measurements much more sensitive to the intensity and polarization of the spectroscopy laser and possibly explains previous experimental discrepancies . Most of this chapter is taken from the author's manuscript [5, 6].

Determining transition frequencies better than a natural line width requires a sufficient understanding of the transition line shape. In particular, the Lorentzian line shape is of fundamental importance in the analysis of resonant phenomena in many areas of physics [28]. When two or more resonances are separated on the order of a natural line width, unresolvable in a fundamental sense not limited by instrumentation, there arises the possibility of interference. The resulting line shape is, in general, no longer a simple sum of Lorentzians, even in the low intensity limit. Although this effect has been known in different contexts for many years [29–32], it has typically been ignored in the interpretation of Doppler free spectra. In previous spectroscopic measurements [3, 4], NIST atomic spectroscopy group demonstrated that spectra were polarization sensitive, which we explain was due to quantum interference. This effect limits accuracy when not properly accounted for, because the lineshape is no longer Lorentzian. In section 2.1, we derive a more general set of line-shapes and estimate the systematic errors incurred if strictly Lorentzian line shapes are assumed. In section 2.2, we use the more complete line shapes to extract absolute optical transition frequencies from new experimental ^{6,7}Li data and quantify errors associated with incomplete line shapes. Finally, in section 2.3, we use our new measurement of the ^{6,7}Li D line isotope shift to extract the relative ^{6,7}Li difference in mean square nuclear charge radius. The unresolvable hyperfine structure in the

D2 lines of hydrogen [33], lithium [3,4], potassium [34], francium [35], singly-ionized beryllium [36], magnesium [37] and excited to further excited transitions such as the H 2s-4p [38] are additional examples where interference modified Lorentzian line shapes are expected.

2.1 Dipole Scattering line shape

We begin with a derivation of the corrected line shape, including quantum interference terms, using the Kramers-Heisenberg formula [39] which describes the differential scattering rate of light incident on an atom initially in the state $|i\rangle$ and ending in the state $|f\rangle$. It can be derived from Fermi's golden rule [40]

$$\frac{dR_{i \to f}}{d\Omega_s} = \frac{2\pi}{\hbar} |M_{fi}|^2 \rho_s, \tag{2.1}$$

where $\hbar$ is Plank's constant(h) divided by 2π and ρ_s is the density of scattered photon states into a solid angle $d\Omega_s$ along the scattering direction $\mathbf{k}_s$. The scattering matrix element M_{fi} is calculated to second order in the electric dipole coupling. The scattering matrix element depends on the frequency, wavevector and polarization of the incident light $(\omega_{\mathrm{L}}, \mathbf{k}_{\mathrm{L}}, \hat{\epsilon}_{\mathrm{L}})$ and scattered light $(\omega_s, \mathbf{k}_s, \hat{\epsilon}_s)$. The resulting scattering rate is:

$$\frac{dR_{i \to f}}{d\Omega_s} = \frac{\pi E_{\mathrm{L}}^2 \omega_s^3}{h^3 c^3 \epsilon_0} \left| \sum_j \frac{(\hat{\epsilon}_s^* \cdot \mathbf{D}_{fj})(\mathbf{D}_{ji} \cdot \hat{\epsilon}_{\mathrm{L}})}{\omega_{ji} - \omega_{\mathrm{L}} - i\Gamma_j/2} \right|^2 \tag{2.2}$$

where c is the speed of light, ϵ_0 is the permittivity of free space, and E_{L} is the amplitude of the electric field of the incident light. The sum is over excited inter-

mediate states $|j\rangle$ with transition frequencies ω_{ji} and atomic dipole matrix elements $\mathbf{D}_{ji} = \langle j|e\mathbf{r}|i\rangle$. Here e is the electron charge and $\mathbf{r}$ is the position operator of the valence electron. The finite lifetime of the excited states $|j\rangle$ are accounted for [39] by including the imaginary part $i\Gamma_j/2$ in the transition frequency ω_{ji} [1]. Here Γ_j is the inverse lifetime (or full width half maximum for an isolated Lorentzian line) of $|j\rangle$. Equation 2.2, valid in the low excitation intensity limit, does not include multiple scattering effects like optical pumping. Additionally, we make the rotating wave approximation, which is appropriate for near resonant excitation. While Eq. 2.2 is a Lorentzian distribution if only one term of the sum is considered, since the sum over intermediate states is *inside* the square, one can see that interference from different excited states $|j\rangle$ is possible.

For a concrete experimental comparison, we restrict our analysis to the case where states $|i\rangle$ and $|f\rangle$ are hyperfine states of a single electronic ground state with electronic angular momentum J, and the intermediate hyperfine states $|j\rangle$ belong to a single excited electronic state with angular momentum J'. The states are labeled by their total angular momentum and z-projection of angular momentum $|F_i, m_i\rangle$, $|F_f, m_f\rangle$, and $|F', m'\rangle$.

One can evaluate the atom field coupling matrix element by repeatedly applying the Wigner-Eckhart theorem. The reduced matrix elements can be written in

---

[1]One may consider whether the interference effects described in this paper could also modify the simple replacement $\omega_{ji} \to \omega_{ji}+i\Gamma_j/2$ when accounting for the coupling to the continuum. However, in the cases considered here (a single electronic state split by fine and hyperfine structure), the effect of interference disappears when integrated over all solid angle. Since the inclusion of Γ_j results from summing the coupling to the continuum over all solid angle, it is probable that the addition of $i\Gamma_j/2$ correctly accounts for the continuum, although a more detailed calculation would be needed to confirm this. Empirically, the line shapes presented here well fit the observed data

terms of the electronic excited state linewidth Γ and a reference intensity I_0 (see 2.4).

(For a closed transition such as the Li 2s-2p transitions considered here, $\Gamma = \Gamma_j$.)

This gives

$$\frac{dR_{i \to f}}{d\Omega_s} = \frac{3}{8\pi} \frac{I}{I_0} \left(\frac{\Gamma}{2}\right)^3 \left| \sum_{F'm'} \frac{(\hat{\epsilon}_s \cdot \mathbf{A}^{F'm'}_{F_f m_f}) \, (\mathbf{A}^{F'm'}_{F_i m_i} \cdot \hat{\epsilon}_{\mathrm{L}})}{\Delta^{F'}_{F_i} + i\Gamma/2} \right|^2 . \tag{2.3}$$

Here $\Delta^{F'}_{F_i} = \omega_{\mathrm{L}} - \omega_{F'F_i}$, and $\mathbf{A}^{F'm'}_{F_f m_f}$ are the normalized dipole matrix elements

containing all the angular dependence of the atomic dipole. The explicit form for

$\mathbf{A}^{F'm'}_{F_i m_i}$ is given in 2.4.

Since the denominator in Eq. 2.3 is independent of m', we can sum the nu-

merator over m'. Defining the function

$$C^{F'}_{i \to f}(\hat{\epsilon}_s, \hat{\epsilon}_{\mathrm{L}}) = \sum_{m'} (\hat{\epsilon}_s \cdot \mathbf{A}^{F'm'}_{F_f m_f})(\mathbf{A}^{F'm'}_{F_i m_i} \cdot \hat{\epsilon}_{\mathrm{L}}), \tag{2.4}$$

we have

$$\frac{dR_{i \to f}}{d\Omega_s} = \frac{3}{8\pi} \frac{I}{I_0} \left(\frac{\Gamma}{2}\right)^3 \left| \sum_{F'} \frac{C^{F'}_{i \to f}(\hat{\epsilon}_s, \hat{\epsilon}_{\mathrm{L}})}{\Delta^{F'}_{F_i} + i\Gamma/2} \right|^2 , \tag{2.5}$$

where $C^{F'}_{i \to f}(\hat{\epsilon}_s, \hat{\epsilon}_{\mathrm{L}})$ depends on the initial and final state quantum numbers F_i, m_i,

F_f and m_f.

Equation 2.5 describes the differential scattering rate of light into solid angle

$d\Omega_s$ (along $\mathbf{k}_s$) with polarization $\hat{\epsilon}_s$ for atoms starting in state $|F_i, m_i\rangle$ and ending

in $|F_f, m_f\rangle$. In a typical spectroscopy experiment, the final scattering state is unre-

solved, so the scattering rate $R_{F_i m_i \to F_f m_f}$ is summed over final states F_f and m_f. To

further simplify the discussion, we assume the detection is polarization insensitive

and sum over the two scattered polarizations $\hat{\epsilon}_s \perp \mathbf{k}_s$ for a given detection direction $\mathbf{k}_s$. If, in addition, we assume an unpolarized atomic sample, we must average over all initial m_i. Summing and evaluating the square in Eq. 2.5, gives rise to sums of Lorentzian components and cross-terms

$$
\frac{dR_{F_i}(\hat{\epsilon}_L)}{d\Omega_s} = \frac{1}{4\pi} \frac{I}{I_0} \left(\frac{\Gamma}{2}\right)^3 \left(\sum_{F'} \frac{f(\mathbf{k}_s, \hat{\epsilon}_L, F_i, F')}{(\Delta_{F_i}^{F'})^2 + (\Gamma/2)^2} + \right.
$$
$$
\left. \sum_{F' \neq F''} 2Re\left[\frac{g(\mathbf{k}_s, \hat{\epsilon}_L, F_i, F', F'')}{(\Delta_{F_i}^{F'} + i\Gamma/2)(\Delta_{F_i}^{F''} - i\Gamma/2)}\right]\right),
\tag{2.6}
$$

where the line strengths $f(\mathbf{k}_s, \hat{\epsilon}_L, F_i, F')$ and cross-term strengths $g(\mathbf{k}_s, \hat{\epsilon}_L, F_i, F', F'')$ for a particular laser polarization and detected direction are given by

$$
f(\mathbf{k}_s, \hat{\epsilon}_L, F_i, F') = \frac{3}{2g_T} \sum_{s, m_i F_f m_f} \left|C_{i \to f}^{F'}(\hat{\epsilon}_s, \hat{\epsilon}_L)\right|^2
$$
$$
g(\mathbf{k}_s, \hat{\epsilon}_L, F_i, F', F'') = \frac{3}{2g_T} \sum_{s, m_i F_f m_f} C_{i \to f}^{F'}(\hat{\epsilon}_s, \hat{\epsilon}_L) \left[C_{i \to f}^{F''}(\hat{\epsilon}_s, \hat{\epsilon}_L)\right]^*,
\tag{2.7}
$$

where $g_T = \sum_i (2F_i + 1)$ is the total number of Zeeman states in the ground electronic state, assumed here to be uniformly thermally populated. When the excited state hyperfine splitting is not well resolved, $\Delta_{F_i}^{F'} - \Delta_{F_i}^{F''} \equiv \Delta_{F'}^{F''} \approx \Gamma$, then the cross-terms are not necessarily negligible, as implicitly assumed in the latter portion of [41].

2.1.1   Angular dependence

Dipole scattering of light follows a dipole radiation pattern [42], which for linearly polarized light depends only on the angle γ between excitation laser polariza-
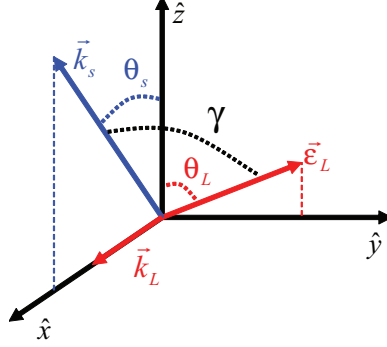
Figure 2.1: Coordinate system: The excitation laser propagates along $\hat{x}$, so that the linear polarization direction $\hat{\epsilon}_L$ lies in the $\hat{y}$-$\hat{z}$ plane, parameterized by θ_L. The detection direction k_s lies in the $\hat{x}$-$\hat{z}$ plane and is parameterized by θ_s. In the apparatus light collection is centered along $\hat{z}$ with an angular spread determined by the numerical aperture of the imaging system. The atomic beam is along $\hat{y}$.

tion ϵ_L and the fluorescence collection direction $\mathbf{k}_s$. The angular dependence of the

dipole scattering is proportional to $\cos^2 \gamma$, and it can always be written as a sum of

a spherically symmetric component and a dipole component $(A_{\text{tot}} + BP_2(\cos \gamma))/4\pi$.

Here A_{tot} is the total line strength integrated over all solid angle, $P_2(x) = (3x^2 - 1)/2$

is the second Legendre polynomial (which has zero integral over solid angle), and

B characterizes the amplitude of the angular dependence. By construction f con-

tains all the scattering linestrength, the integral of the cross-terms g, proportional

to $P_2(\cos \gamma)$, over solid angle vanishes. A consequence of this angular dependence

is that $f(\mathbf{k}_s, \hat{\epsilon}_L, F_i, F')$ does *not* provide the correct ratio of line strengths of the

$F_i \to F'$ transitions for an arbitrary choice of detection direction, γ, since B/A_{tot}

is not the same for different F'. As we will show, however, there exist "magic"

orientations where f does give line strengths consistent with resolved transitions.

More importantly, at these magic conditions the cross-terms g vanish, giving rise to

purely Lorentzian line shapes.

We parameterize γ in terms of angles relevant to an experimental geometry. The wave vectors $\hat{k}_\mathrm{L}$ and $\hat{k}_s$ define a plane which we take to be the $\hat{x}$-$\hat{z}$ plane. Without loss of generality we can take $\hat{k}_\mathrm{L}$ along $\hat{x}$, so that $\hat{\epsilon}_\mathrm{L}$ lies in the $\hat{y}$-$\hat{z}$ plane, making an angle θ_L with respect to $\hat{z}$, and $\hat{k}_s$ lies in the $\hat{x}$-$\hat{z}$ plane making an angle θ_s with respect to $\hat{z}$, see Fig. 2.1. The scattering is then parameterized by the linearly independent angles θ_s and θ_L; $f(\mathbf{k}_s, \hat{\epsilon}_\mathrm{L}, F_i, F') = f(\theta_\mathrm{s}, \theta_\mathrm{L}, F_i, F')$ and similarly for g [2]. The spherical harmonic addition theorem [43] can be used to relate $P_2(\cos\gamma)$ to θ_s and θ_L:

$$P_2(\cos\gamma) = \frac{1}{2}\left(3\cos^2\theta_\mathrm{s}\cos^2\theta_\mathrm{L} - 1\right). \tag{2.8}$$

The general form for f and g is then

$$
\begin{aligned}
f(\theta_\mathrm{s}, \theta_\mathrm{L}, F, F') &= A_F^{F'} + \frac{B_F^{F'}}{2}\left(3\cos^2\theta_\mathrm{s}\cos^2\theta_\mathrm{L} - 1\right) \\
g(\theta_\mathrm{s}, \theta_\mathrm{L}, F, F', F'') &= \frac{C_F^{F'F''}}{2}\left(3\cos^2\theta_\mathrm{s}\cos^2\theta_\mathrm{L} - 1\right),
\end{aligned}
\tag{2.9}
$$

where $A_F^{F'}$, $B_F^{F'}$ and $C_F^{F'F''}$ are constants determined by evaluating Eq.2.7. When $\cos\theta_\mathrm{s}\cos\theta_\mathrm{L} = 1/\sqrt{3}$, g vanishes and f correctly gives the line strength ratios. This can occur for a range of geometries. In particular, when the detection $\mathbf{k}_s$ is orthogonal to the excitation $\mathbf{k}_\mathrm{L}$ ($\theta_\mathrm{L} = \gamma$, $\theta_\mathrm{s} = 0$) as in the apparatus [3, 4], then $\theta_\mathrm{L} = \arccos(\frac{1}{\sqrt{3}}) \equiv \theta_\mathrm{M} \approx 54.73°$ is the so called "magic" angle. Similar magic angle effects occur in quantum beat spectroscopy, which could be viewed as a time domain analogue of the effect considered here, where the excitation pulse width

---

[2] Alternatively, $\hat{\epsilon}_\mathrm{L}$ could be fixed along $\hat{z}$, and $\mathbf{k}_s$ could be characterized by polar angles (θ'_s, ϕ'_s). This would have the advantage that $\theta'_s = \gamma$, but it is more convenient for a fixed scattering geometry to have θ_L be one of the free parameters.

replaces the natural width [12, 44]. Explicit expressions for $f(\theta_{\rm L}, F_i \to F')$ and $g(\theta_{\rm L}, F_i \to F', F_i \to F'')$ are evaluated for lithium with the collection along the $\hat{z}$ direction in 2.5.

2.1.2 Line shape impact on extracted frequencies

We now give a qualitative discussion of the effect of the additional interference terms on Doppler-free, or nearly free, spectra. We choose [6,7]Li as an example because of its fundamentally unresolvable structure ($\Delta_{F'}^{F''}/\Gamma \approx 1$) and because it allows for direct comparison to experimental data. Fig 2.2 illustrates two primary effects. First, the maxima of the total line shape are shifted relative to what is predicted by a simple sum of Lorentzian distributions, which can lead to errors in extracting the weighted line center. Second, peaks may vary in intensity and prominence depending on the polarization angle of the laser. For example in Fig 2.2, $\theta_{\rm L} = 0$, the amplitude of the $F = 2 \to F' = 3$ component is reduced with respect to the $F = 2 \to F' = 2$ component.

Line centers are typically determined by fitting a sum of Lorentzian functions to the observed spectral profile. We characterize the effect of cross-terms on line centers (both of individual hyperfine components and of centers of gravity of composite features) by taking a Doppler-free line shape given by Eq. 2.7 with cross-terms and fitting to it using only Lorentzian functions (amplitude, center, offset, linewidth). We then compare the centers given by Eq. 2.7 to the centers extracted from the fit to estimate the effect of the cross-terms on measured quantities. From Eq. 2.9 (with
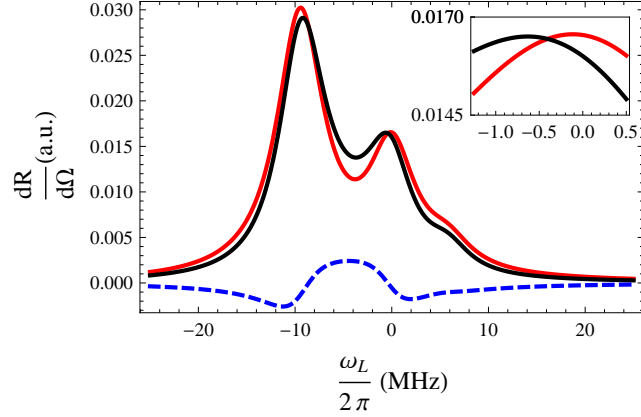
Figure 2.2: The scattering rate (or intensity), $\frac{dR}{d\Omega}$ in arbitrary units, of the $F = 2 \rightarrow F' = 1, 2, 3$ Doppler-free feature in ^{7}Li with $\theta_\mathrm{L} = 0$. Red: sum of Lorentzians with polarization independent weights, Blue dashed: sum of cross-terms, Black: sum of Lorentzians and cross-terms. The laser frequency, $\omega_\mathrm{L}/2\pi$, is the offset from the $F = 2 \rightarrow F' = 2$ peak in units of MHz. The inset is the F=2 $F = 2 \rightarrow F' = 2$ peak enlarged to show the shift in line center.

$\theta_\mathrm{L} = \gamma$, $\theta_\mathrm{s} = 0$), one can see that the magnitude of the shifts, proportional to the angular dependent terms, has maxima at $\theta_\mathrm{L} = 0, \pi/2$ and the sign of the effect changes at $\theta_\mathrm{L} = \theta_\mathrm{M}$. This will be experimentally verified in the next section. The size of the shifts in Li are on the order of 100 kHz to 1 MHz, large enough to completely overshadow effects associated with Doppler shifts and optical pumping.

To provide an estimate for other transitions not explicitly considered here, we imagine atoms with the electronic structure of ^{6}Li or ^{7}Li with variable hyperfine coupling. We consider shifts of individual hyperfine components as the hyperfine splitting is varied. We intuitively expect that degenerate resonances would not affect the measured line position. In the opposite limit, $\Delta_{F'}^{F''}/\Gamma \gg 1$ we also expect the line positions to be unperturbed. These two limits imply that there must be an intermediate hyperfine splitting that maximally affects the measured line positions. We can see in Fig. 2.3 that this happens when $\Delta_{F'}^{F''}/\Gamma$ is of order one.
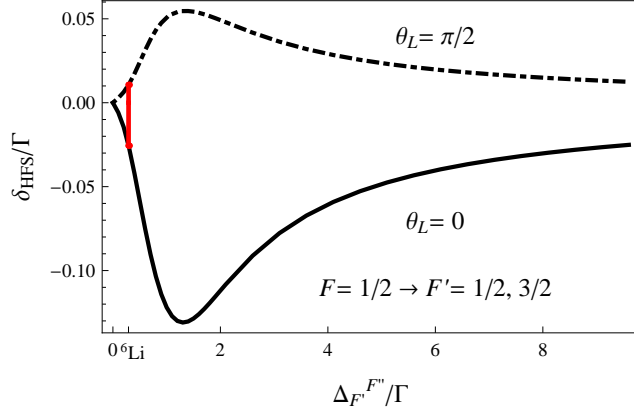
Figure 2.3: Error in the measured hyperfine splitting (in units of Γ) for a $F = 1/2 \to F' = 1/2, 3/2$ transition as a function of the assumed separation when the theoretically calculated full line shape is fit as the sum of two Lorentzians. The dash dotted (solid) curve is for laser polarization $\theta_{\rm L} = \pi/2$ (0). The error in the hyperfine splitting is greatest where the assumed separation is about 1.3 times the natural line width. The red vertical line indicates the x-position of the actual hyperfine splitting for ^{6}Li. Its vertical extent shows the range of errors that can occur when the laser polarization is varied between 0 and $\pi/2$.

To get a feel for the apparent shifts of individual components as a function of separation, we consider a simple analytically solvable line shape consisting of two Lorentzian profiles with splitting Δ and equal amplitude. We take line profiles with and without cross terms and determine the component positions for each as the zero crossings of their first derivatives. We examine the difference of the position of the first component in the Lorentzian only profile, $x_{\rm L}$, and the position of the corresponding component in the full line profile including cross terms, $x_{\rm F}$, as a function of the splitting Δ. In the limit of distantly spaced resonances, $\Delta/\Gamma \gg 1$, the difference in line centers is $x_F - x_{\rm L} \simeq \Gamma^2/4\Delta$, in agreement with the large splitting limit described in [32]. These shifts at large separation have recently been calculated at the 1 kHz level in meta-stable He [45] and in principle occur in muonic hydrogen, although at $\approx$100 MHz they are much too small to account for the discrepancy

16

between proton charge radius values [2, 46]. In alkalis with resolvable hyperfine structure, i.e. ^{87}Rb and ^{133}Cs, these shifts may also appear at the $\approx$10 kHz level which, while much smaller than in unresolvable lines is on the order of the reported experimental uncertainties [47, 48]. This zero intensity shift may also arise from fine structure interference, and for Li is $\approx$900 Hz (below our experimental uncertainty). These shifts at large separation may be particularly insidious because they would only add a weak linear dependance to the background without deforming the line shape as in the case of unresolvable features.
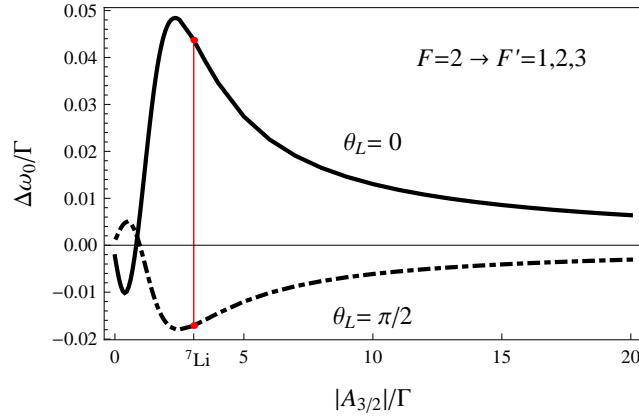
Figure 2.4: Error in the measured center of gravity (in units of Γ) for a $F = 2 \rightarrow F' = 1, 2, 3$ transition as a function of the hyperfine A constant when the theoretically calculated full line shape is fit as a sum of three Lorentzians. The dash dotted (solid) curve is for laser polarization $\theta_L = \pi/2$ (0). The red vertical line indicates the x-position of the actual A constant for ^{7}Li. Its vertical extent shows the range of errors that can occur when the laser polarization is varied between 0 and $\pi/2$.

We also investigate the dependence of an unresolved feature's extracted center of gravity on hyperfine separation as shown in Fig. 2.4. Using the same procedure, we generate the full line shape, now with three components (F=2 $\rightarrow$ F'=1,2,3). We vary the splitting via the magnetic dipole constant, $A_{3/2}$, while fixing the electric quadrupole constant at the value appropriate for ^{7}Li. The same qualitative behavior

occurs, producing extracted center of gravity shifts which are largest when $|A_{3/2}|(\propto$ $\Delta_{F'}^{F''})$ is of order Γ. There is now an additional feature, since there are two resonances that can shift relative to each other, the sign of the shift can change for a given laser polarization.

2.2 Application to ^{6,7}Li Experimental Data

Having discussed the nature and theoretical implications of quantum interference effects on the observed line shape, we apply our theoretical results to experimentally measured spectra of the lithium D lines, see Fig. 2.5 for complete level structure, taken at multiple laser polarization angles. The data that this analysis was based upon was taken in the NIST spectroscopy group [3, 49]. Our additional analysis provides a determination of the absolute transition frequencies of the ^{6,7}Li D2 lines. These new data provide an improved measure of the ^{6,7}Li excited state fine structure, 2s-2p isotope shift, and the isotopic difference in the ^{2}P fine-structure splitting, the splitting isotope shift (SIS). The SIS provides the best point of comparison between theory and experiment. We propose that the interference effect we describe here is the root cause for some disagreements between previous measurements in Li [14–17] and for the lack of internal consistency of the frequency comb based measurement in K [34].

A simplified schematic view of the spectroscopy group's apparatus [3, 4, 49] is shown in Fig. 2.6. Light from a single frequency diode laser intersects a collimated thermal beam of lithium atoms at a right angle. A half wave plate controls the angle
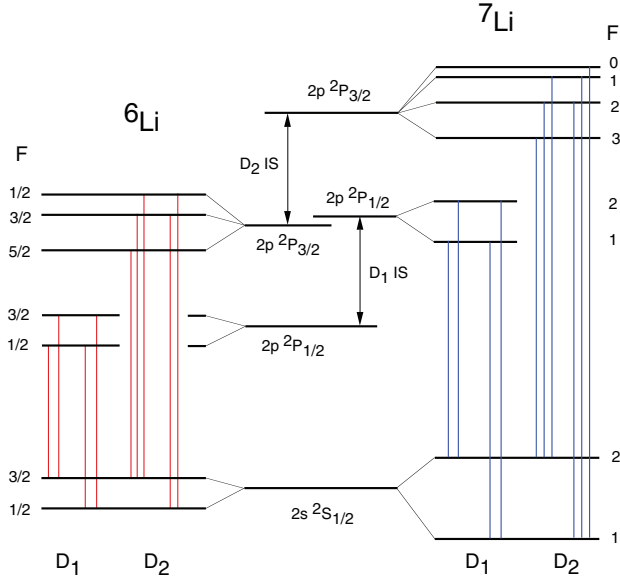
Figure 2.5: Relevant ^{6,7}Li level structure. The hyperfine components for the D2 transition have natural widths of order the hyperfine splitting. IS (isotope shift)

of polarization of the light. The laser beam is retroreflected by a precise corner cube that provides a return beam anti parallel to better than 1.45 μrad. The return beam is chopped by a mechanical chopper. The spectrum is observed by scanning the laser frequency over a lithium component and recording the fluorescence along an axis approximately orthogonal to both the laser and atomic beams. The frequency of the spectroscopy laser is referenced to a single tooth of an optical frequency comb which is in turn referenced to a Cesium atomic clock. To minimize stray light and magnetic field, the interaction region is surrounded by a three level mu metal shield and the atomic beam florescence is imaged on a photocathode through 670 nm interference filters. Figure 2.7, taken from [3], shows typical data for both the F=2→ F'=1,2,3 D2 feature as well as the F=1→ F'=1 and 2 D1 features. When fit with Voigt functions the D2 features show significant residuals away from the empirically determined magic angle. This effect is not evident in any of the D1
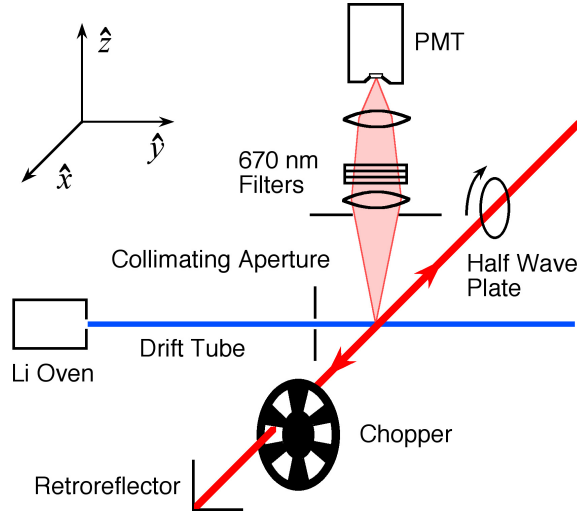
Figure 2.6: Simplified schematic diagram of the NIST spectroscopy group's experimental apparatus. The interaction region is surrounded by three layers of mu-metal (not shown) to minimize the magnetic field. The coordinate system shown is consistent with Fig.2.1

features.

Doppler free spectra of the Li D lines were taken at different laser polarization angles θ_{L} and fit using the line shapes presented here convolved with a Gaussian to account for the residual Doppler broadening present in the experiment, typically ≈ 4 MHz. For resolved resonance features without a polarization dependence, such as the D1 lines, the independent fitting parameters are the line center, the overall amplitude, a constant background offset, the natural width, and the Doppler width. The polarization angle of any given data set was fixed. For the unresolved fluorescence features, we limited the number of fitting parameters by fixing the excited state hyperfine splittings to values calculated in [50] and in agreement with [51]. In addition we fixed the ratio of the unresolved amplitudes to values given by Eq. 2.9, with numerical values for $A_F^{F'}$, $B_F^{F'}$, and $C_F^{F',F''}$ tabulated in 2.5. A small correction was made to account for the effect of the finite collection angle of the detector (see 2.6).
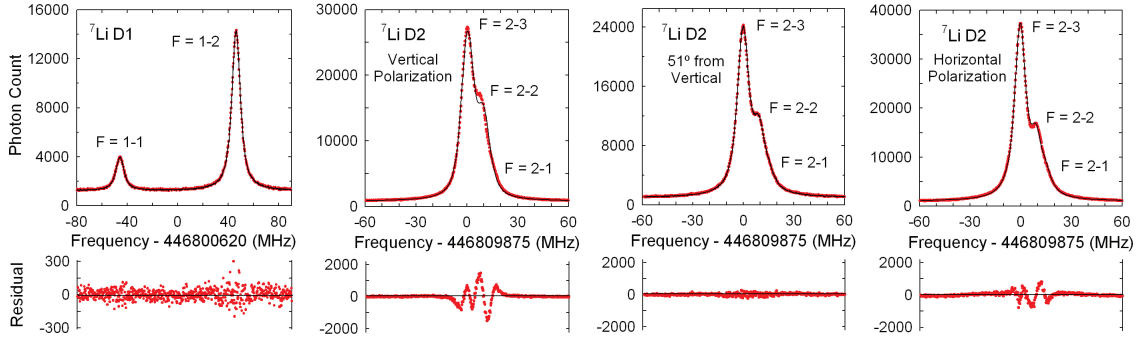
Figure 2.7: Lorentzian only fits to D1 and D2 data. Note the scale of the residuals is nearly a factor of ten larger on the D2 feature.

2.2.1 Apparent line-strength and frequency variation with θ_{L}

One of the most striking features present in the more complete line shapes is the change in the amount of scattered light with excitation polarization. A single fit to five spectra at different laser polarization angles demonstrates good overall agreement, including relative line-strengths. Fig. 2.8 shows the $F = 1/2 \rightarrow F' = 1/2, 3/2$ D2 feature of ^{6}Li (center, $\omega_{\mathrm{L}}/2\pi \approx 0$ MHz) and the $F = 2 \rightarrow F' = 1, 2$ D1 peaks of ^{7}Li (left and right, $\omega_{\mathrm{L}}/2\pi \approx \pm 50$ MHz). The ^{7}Li D1 lines have no angular dependence (in general no D1 lines have angular dependence). The presence of the D1 lines enable the single fit to multiple data sets because they allow the effect of background light levels and laser intensity fluctuations to be compensated for in multiple spectra taken at different times. The fit to these five data sets used only one natural width and one (mass scaled) Doppler width.

To demonstrate the apparent transition frequency shifts resulting from analysis

21
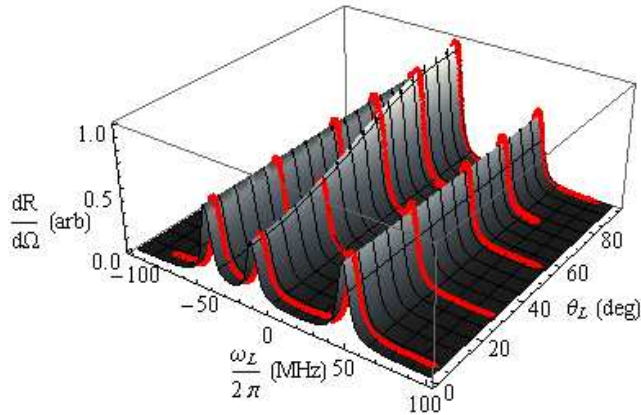
Figure 2.8: Amplitude of scattered light, proportional to Eq. 2.7, as a function of laser frequency ω_L and laser polarization angle θ_L. The laser frequency is offset from the ^{6}Li F = 1/2 ground state by 446 THz (see table 2.1 for optical frequencies). The gray scale surface is the complete theoretical line shape including cross-terms and the red points are experimental data taken at $\theta_L = 0°, 25°, 51°, 75°$ and $90°$. The central feature is the $F = 1/2 \rightarrow F' = 1/2, 3/2$ transitions in ^{6}Li while the two constant amplitude side peaks are the F = 1 $\rightarrow$ F' = 1, 2 D1 lines of ^{7}Li.

with an incomplete line shape in measured ^{7}Li D2 data, we fit the same spectra taken at different laser polarizations and extract the line centers, with and without the cross-terms. In Fig. 2.9, the red points are line centers fit without cross-terms and the black points are the same data fit with the full theory. The black points are self consistent, independent of laser polarization while the red points exhibit a strong polarization dependence. The fit to the red data is of the form $A + BP_2(\cos\theta_L)$. The amplitude of the laser polarization dependent shift is of order 1 MHz. Near the magic angle $\theta_L = \theta_M \approx 54.7$ the Lorentzian fits give the same linecenter as the full line shape.
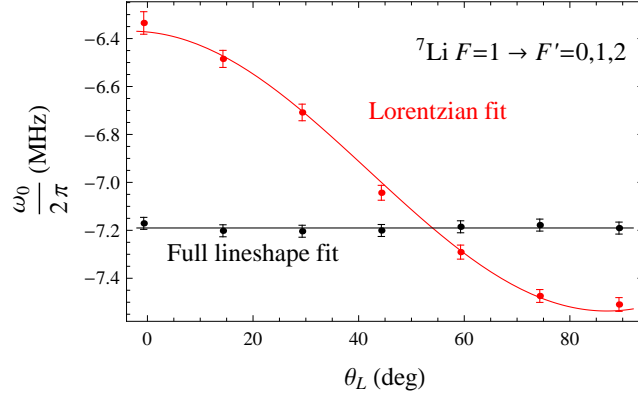
Figure 2.9: Line center of the ^{7}Li $F = 1 \rightarrow F' = 0, 1, 2$ feature fit from experimentally measured spectra as function of laser polarization angle with respect to the collection direction. Transition frequencies are offset from the ^{7}Li F=1 ground state by 446 THz (see table 2.1 for optical frequencies). The black (red) data points were extracted by fitting the data to functions with (without) interference cross-terms. Error bars represent the uncertainties given in table 2.1.

2.2.2 Discussion of Systematics

Angular offset: To accurately extract line positions at all polarizations, the angle θ_L between the laser polarization and the detection optics must be controlled and understood. Using a waveplate, θ_L could only be measured up to a small unknown offset angle θ_0. After our theoretical analysis indicated that the offset angle was an important source of systematics, the spectroscopists made an improved estimate of θ_0 [3, 4] by geometric measurements made when they disassembled the apparatus, finding $\theta_0 = -0.7(10)$ degrees.

As a consistency check, we compared the well known ground state hyperfine intervals (GHI) to GHI values we measure by subtracting optical frequencies at multiple angles θ_L. We note that for small offsets θ_0, the line shifts near $\theta_\mathrm{L} = 0, \pi/2$ are insensitive to first order in θ_0 because the derivative of the angular dependence ($\propto \sin\theta_\mathrm{L} \cos\theta_\mathrm{L}|_{\theta_\mathrm{L}=\gamma,\ \theta_\mathrm{s}=0}$) vanishes. This is of practical utility since data fit at $\theta_\mathrm{L} =$

$0, \pi/2$ with the complete line shape including cross-terms should be accurate as well as equal to each other. We found that while the GHI's derived from measurements of the resolved D1 lines [3, 4] were consistent with known values [52], the GHI's derived from the unresolved D2 lines at $\theta_{\mathrm{L}} = 0, \pi/2$ differed from the known values by as much as 30 kHz. This disagreement indicates the importance of intensity dependent shifts on the fitted line shapes when cross-terms are significant.

Intensity dependent shifts: For isolated lines, the fitted amplitudes are taken to be free parameters and the fitted line centers are independent of fitted amplitude. As a consequence, the centers of the resolved lines are not sensitive to intensity dependent effects like optical pumping that modify the line ratios from their theoretical values. For unresolvable lines, however, the fitted line positions depend on the fixed relative values of f and g used in the fit. The unresolvable lines are therefore sensitive to intensity dependent effects. To explore the impact of excitation laser intensity on extracted line centers, a subset of spectra were measured at multiple laser powers and we performed a full optical Bloch equation (OBE) simulation of the scattering, including all the ground and excited Zeeman levels [53, 54]. We numerically solve the OBE with a time-dependent Rabi frequency proportional to the Gaussian intensity profile seen by the atom as it transverses the excitation laser beam. We then generate a Doppler free line shape by calculating the directional photon scattering rates derived from the OBE, as a function of laser frequency. At the intensities used here and in [3, 4], we find these intensity dependent effects are small but important ($\approx$ 20 kHz). However, we suggest that larger previously reported uncertainties ($\approx$ 100 kHz) in ^{39,41}K [34] ascribed to optical pumping could

likely be removed by using a line shape that includes crossterms.

To quantitatively account for intensity dependent light shifts and optical pumping effects on the line positions, we generate numerical OBE data at several different intensities and fit the numerical data using the analytically calculated line strengths f and g appropriate for low intensity. (We confirm that in the low intensity limit, the numerical data matches both the expected line positions and line strengths.) We then determine the linear intensity-dependent line shifts from this numerical data, and apply this shift to the measured line positions [3]. The laser intensities were determined experimentally from the relative line strengths of the resolved features taken at different laser intensities. This estimate of the intensity is somewhat lower than estimates based on measured beam waists and laser power (typically 3.5 mm and 3 μW respectively) but removes uncertainty associated with secondary measurements of beam waist and power. For most features, the shift was of order a few kHz/μW, but for the ^{7}Li D2 $F = 1 \rightarrow F' = 0, 1, 2$ transitions it was as large as 6.7 kHz/μW (for our beam waist). The uncertainty in this correction was set equal to the value of the applied shift and represents one of the largest sources of uncertainty in the experiment. For the unresolvable lines considered here, we find that optical pumping can have a larger systematic effect than the light shifts alone. Future experiments should be careful to work at low intensities to avoid these shifts on unresolvable lines.

Doppler correction: The correction of the first order Doppler effect was deter-

---

[3]Another approach might be to fit the numerical data with free line weights and use the determined intensity dependent line weight ratios in the experimental fits. This provides a large number of free parameters, however, and the fits to numerical data were unstable in some cases.

mined from simultaneously recorded forward and reverse beam signals using a corner cube to retro-reflect the excitation laser beam. For the polarization independent D1 lines [3,4] the systematic contribution to the uncertainty of this correction is 1.4 kHz due to imperfections of the corner cube retroreflector. Because the retroreflector does not preserve the laser polarization, the Doppler correction for the polarization sensitive unresolved D2 lines could not be determined using the corner cube, and is taken instead from a linear fit of correction versus time for resolved components measured on the same day. This is necessary because the laser alignment drifts slightly over hours of data taking, and results in a larger Doppler uncertainty of about 10 kHz.

2.2.3 Results, absolute transition frequencies

Including the Doppler corrections and the power dependent shifts, the GHI values at $\theta_{\rm L} = 0, \pi/2$ are in agreement with each other and the known values [52] (see Figs. 2.10 and 2.11). The value of θ_0 that minimizes the $\sin\theta_{\rm L}\cos\theta_{\rm L}$ angular dependence is consistent with the geometrically determined value. The final reported line positions, shown in table 2.1, represent an average over $\theta_{\rm L}$. A representative uncertainty budget is given in table 2.2.

Measurements at multiple laser polarizations analyzed with the correct line shape provide an important tool to independently estimate systematic errors associated with the offset angle θ_0. For example, power-dependent shifts such as optical pumping can partially cancel the effect of θ_0 on the line shape and GHI. Minimizing
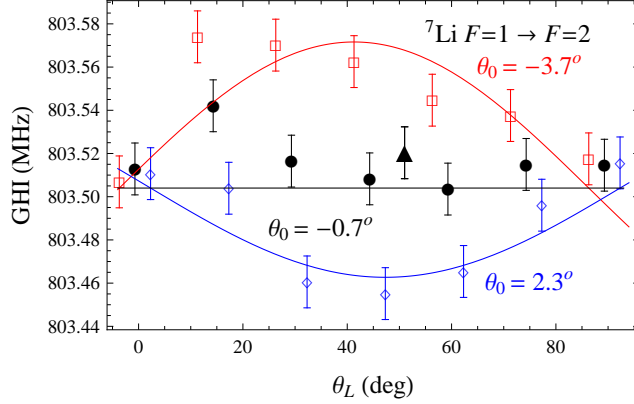
Figure 2.10: ^{7}Li ground state hyperfine interval ($F = 1 \rightarrow F = 2$) as function of laser polarization angle. The measured GHI was determined by subtracting absolute measurements of the excited state $F = 1 \rightarrow F' = 0, 1, 2$ and $F = 2 \rightarrow F' = 1, 2, 3$ features including Doppler and intensity dependent corrections (see the text). The red (black, blue) data is for an angular offset of $-3.7°$ ($-0.7°$,$2.3°$). The red (black,blue) curve is of the form $A_{\theta_0} \sin(\theta) \cos(\theta) + \text{GHI}_0$, where GHI_0 is the value measured in [52] and A_{θ_0} is fit to the data. The triangular point is data from [3, 4] re-analyzed using the procedure described in the present work. Error bars represent the uncertainties given in table 2.1.

residuals and comparing the GHI near θ_m can still lead to small systematic shifts in the line positions. These effects are more prominent in ^{7}Li than ^{6}Li, and our new determinations of the absolute cog transition frequencies differ from our previous results [3, 4], by 83 kHz and 19 kHz, respectively. From the absolute frequencies the excited state fine structure splitting (Table 2.3), as well as the 2s-2p IS and the SIS (Table 2.4) are calculated and compared to the existing literature. As discussed in [24], both quantum electrodynamic and nuclear size corrections largely cancel when calculating the SIS. It is, therefore, the most reliable result of theory and has been suggested as a benchmark for testing the internal consistency of experimental data. Previously reported results have disagreed with each other and with theory far beyond their reported uncertainties (Table 2.4). Our current result resolves these discrepancies and is in full agreement with the most recent theoretical result [50].
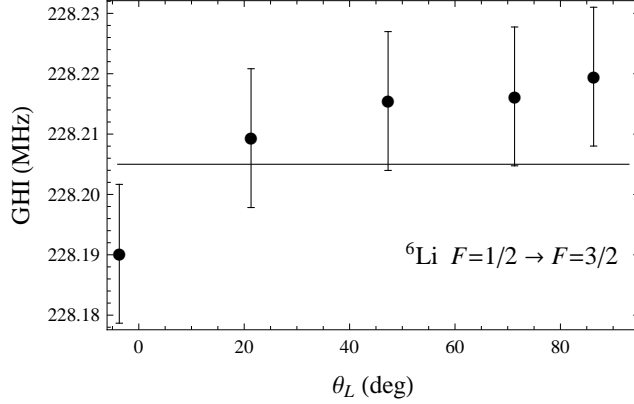
Figure 2.11: ^{6}Li ground state hyperfine interval ($F = 1/2 \to F = 3/2$) as function of laser polarization angle. The measured GHI was determined by subtracting absolute measurements of the excited state $F = 1/2 \to F' = 1/2$, $3/2$ and $F = 3/2 \to F' = 1/2$, $3/2$, $5/2$ features. The solid line is the value measured in [52]. Error bars represent the uncertainties given in table 2.1.

This supports the theory that underlies the use of D-line IS's to determine mean square nuclear charge radii for short lived Li isotopes.

2.3 Extraction of relative nuclear charge radii

Finally, we calculate the difference in the ^{6,7}Li nuclear charge radii using the measured D2 isotope shifts reported in Table 2.4 and the D1 shifts reported in [3, 4]. This serves as a point of comparison amongst different types of measurements including elastic electron scattering [57], optical isotope shift measurements on the $^3S_1 \to^3 P_{0,1,2}$ transition in Li$^+$ [58], and optical isotope shift measurements of the 2s-3s, D1, and D2 transitions in neutral Li [14–22] as shown in Fig. 2.12. We calculate the difference in nuclear charge radius using Eq. (40) of [13],

$$\delta\langle r_{\rm c}^2\rangle(^{7,6}{\rm Li}) = \langle r_{\rm c}^2\rangle(^{7}{\rm Li}) - \langle r_{\rm c}^2\rangle(^{6}{\rm Li}) = \frac{(E_{\rm meas} - E_0)}{C_0} \qquad (2.10)$$

Table 2.1: Measured frequencies of hyperfine components and centers of gravity (cog) of the ^{6,7}Li D2 lines.

Line	F	F'	Frequency (MHz)
^{6}Li D2	3/2	5/2	446799571.067(21)
	3/2	3/2	446799573.962(21)
	3/2	1/2	446799575.673(21)
	1/2	3/2	446799802.172(16)
	1/2	1/2	446799803.883(16)
^{6}Li D2 cog			446799648.870(15)
^{7}Li D2	2	3	446809874.895(20)
	2	2	446809884.357(20)
	2	1	446809890.170(20)
	1	2	446810687.873(25)
	1	1	446810693.687(25)
	1	0	446810696.445(25)
^{7}Li D2 cog			446810183.163(16)

Table 2.2: Representative uncertainty budget (kHz).

Uncertainty Component	^{6}Li D2 $F = 3/2 \to F' = 5/2, 3/2, 1/2$
Statistical variation	4
First order Doppler effect	10
Estimate of θ_m	3
Laser power dependent shifts[4]	17
Laser intensity variation	3
Hyperfine constant inaccuracy	2
Imaging system imperfections	2
Magnetic field shift	< 1
Fine structure interference	< 1
Reference frequency	0.089
Total	21

Table 2.3: Excited state fine-structure intervals.

Interval[5]	Splitting (MHz)	Reference
^{6}Li 2p ^{2}P fs	10052.779(17)	this work
	10052.799(22)	Sansonetti [3,4]
	10052.76(22)	Brog [55]
	10052.044(91)	Walls [16]
	10052.964(50)	Noble [17]
	10052.862(41)	Das [18]
	10050.932(8) [6]	Puchalski(theory) [50]
^{7}Li 2p ^{2}P fs	10053.310(17)	this work
	10053.393(21)	Sansonetti [3,4]
	10053.184(58)	Orth [56]
	10052.37(11)	Walls [16]
	10053.119(58)	Noble [17]
	10051.999(41)	Das [18]
	10051.477(8)	Puchalski(theory) [50]

Table 2.4: ^{7,6}Li isotope shifts.

Transition	Shift (MHz)	Reference
D2 IS	10534.293(22)	this work
	10534.357(29)	Sansonetti [3,4]
	10533.59(14)	Walls [16]
	10534.194(104)	Noble [17]
	10533.352(68)	Das [18]
SIS[7]	0.531(24)	this work
	0.594(30)	Sansonetti [3,4]
	-0.67(14)	Walls [16]
	0.155(60)	Noble [17]
	-0.863(79)	Das [18]
	0.396(9)	Yan(theory) [24]
	0.5447(1)	Puchalski(theory) [50]

where $\langle r_c^2 \rangle(^i\mathrm{Li})$ is the mean square nuclear charge radius of the ith isotope in fm^2,

$\mathrm{E_{meas}}$ is the measured isotope shift in MHz, $E_0 = -10532.5682(-10532.0237)$ MHz

is the theoretically calculated isotope shift excluding the finite size corrections for

the D2(D1) transitions [59] and $C_0 = -2.4658$ MHz/fm^2 [59].
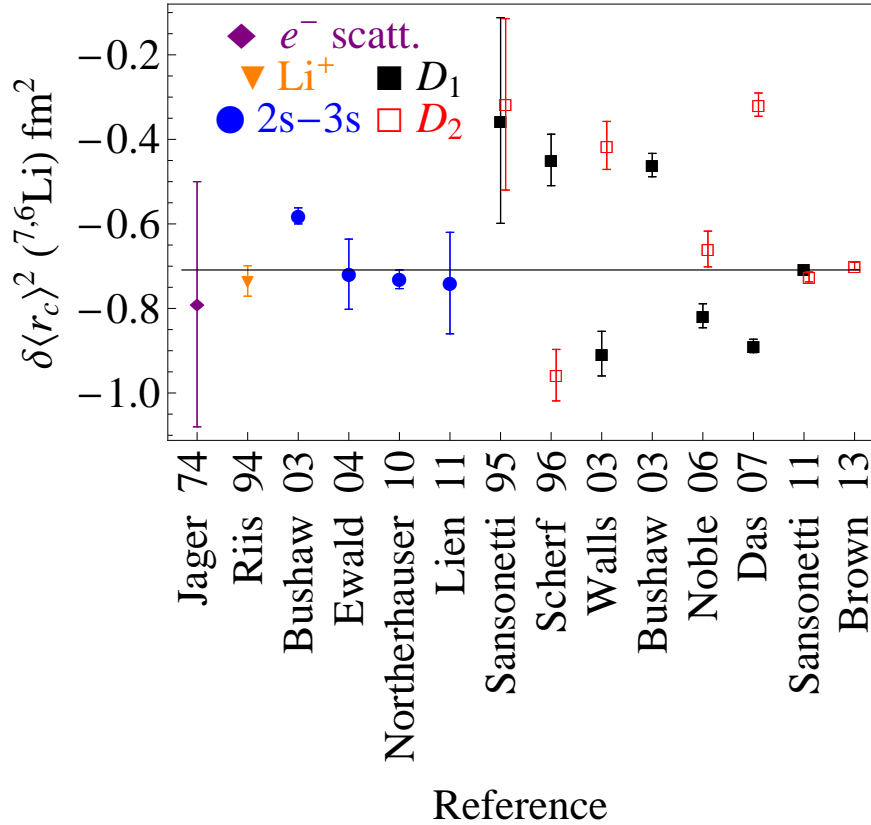
Figure 2.12: Measurements of the difference in mean square charge radius between ^{7}Li and ^{6}Li. The points are grouped by type of measurement and are then ordered chronologically within different types of measurement. The solid black line is the weighted average of the results of references [23, 57, 58], along with the D1 value from [3,4] and the D2 value from this work. Error bars for the present work represent the uncertainties given in table 2.4, all other error bars represent the uncertainties given in the original references.

The values of the difference in mean square nuclear charge radius are

$-0.705(3)$ fm^2 for the D1 and $-0.700(9)$ fm^2 for the D2 lines. These values are

self consistent and have the smallest uncertainties yet reported. They bring the D-

line measurements into full agreement with the best values from electron scattering and optical IS measurements on 2s-3s and $^3S_1 \rightarrow^3 P_{0,1,2}$ transitions in Li and Li$^+$ respectively.

2.4 Calculation of the reduced matrix element

Expressions for the normalized dipole matrix elements: The vector components of $\mathbf{A}$ are easiest to describe in the spherical vector basis A_q appropriate for σ^+, π and σ^- light, where

$$
\begin{aligned}
A_1 &= -(A_x + iA_y)/\sqrt{2} \\
A_0 &= A_z \\
A_{-1} &= (A_x - iA_y)/\sqrt{2}.
\end{aligned}
\tag{2.11}
$$

Using the Wigner-Eckart theorem, the dipole matrix elements are given in terms of reduced matrix elements as

$$
(D_{Fm}^{F'm'})_q = \frac{\langle F'||\mathbf{D}||F\rangle}{\sqrt{2F'+1}}\langle Fm; 1q|F'm'\rangle,
\tag{2.12}
$$

where $\langle Fm; 1q|F'm'\rangle$ is the Clebsch-Gordan coefficient for adding $|F, m\rangle$ to $|1, q\rangle$ to get $|F', m'\rangle$. Under the assumption that the hyperfine interaction does not modify the electronic structure of the state, the F-reduced matrix elements can be written

in terms of J-reduced elements

$$\langle F'||\mathbf{D}||F\rangle = \langle J'||\mathbf{D}||J\rangle\sqrt{f_F^{F'}}, \qquad (2.13)$$

where the reduced oscillator strength $f_F^{F'}$ for the F-F' transition can be written in terms of Wigner 6-j symbols:

$$\sqrt{f_F^{F'}} = (-1)^{F+I+1+J'}\sqrt{2F+1}\sqrt{2F'+1}\begin{Bmatrix} J' & J & 1 \\ F & F' & I \end{Bmatrix}. \qquad (2.14)$$

Defining the components of the matrix elements $(\mathbf{A}_{Fm}^{F'm'})_q$ for each $J \to J'$ transition

$$(\mathbf{A}_{Fm}^{F'm'})_q = \frac{\sqrt{2J'+1}}{\sqrt{2F'+1}}\langle Fm;1q|F'm'\rangle\sqrt{f_F^{F'}}, \qquad (2.15)$$

the dipole matrix elements can be written as

$$(D_{Fm}^{F'm'})_q = \frac{\langle J'||\mathbf{D}||J\rangle}{\sqrt{2J'+1}}(\mathbf{A}_{Fm}^{F'm'})_q . \qquad (2.16)$$

Pulling the reduced matrix element $\langle J'||\mathbf{D}||J\rangle$ out of the sum, Eq. 2.2 can be written in terms of the inverse scattering rate Γ and a saturation intensity I_0,

$$\Gamma = \frac{1}{\tau} = \frac{\omega^3}{3\pi\epsilon_0\hbar c^3}\frac{|\langle J'||\mathbf{D}||J\rangle|^2}{(2J'+1)}, \qquad (2.17)$$

and

$$I_0 = \frac{\pi hc\Gamma}{3\lambda^3}, \qquad (2.18)$$

giving Eq. 2.3, where ω and λ are the frequency and wavelength of the transition.

2.5   Tables of lineweights and cross-terms for I = 1/2, 1, 3/2

Calculation of weights f and g: The dipole radiation weights f and g are calculated using the expression for $\mathbf{A}_{Fm}^{F'm'}$ (Eq. 2.15) to determine $C_{i \to f}^{F'}$ (Eq. 2.4), evaluating the sums in Eq. 2.7 and then comparing to the dipole radiation pattern Eq. 2.9. Taking k_s along $\hat{z}$, (i.e. $\theta_s = 0$), with the two scattered polarizations $\hat{\epsilon}_{s1} = \hat{x}$ and $\hat{\epsilon}_{s2} = \hat{y}$, and $\hat{\epsilon}_L$ to lie in the $\hat{z}$-$\hat{y}$ plane as in Fig 2.1, the terms in the sum are given by

$$\hat{\epsilon}_{s1} \cdot \mathbf{A}_{Fm}^{F'm'} = \frac{-1}{\sqrt{2}} \left((\mathbf{A}_{Fm}^{F'm'})_1 - (\mathbf{A}_{Fm}^{F'm'})_{-1} \right) \tag{2.19}$$

$$\hat{\epsilon}_{s2} \cdot \mathbf{A}_{Fm}^{F'm'} = \frac{i}{\sqrt{2}} \left((\mathbf{A}_{Fm}^{F'm'})_1 + (\mathbf{A}_{Fm}^{F'm'})_{-1} \right) \tag{2.20}$$

$$\hat{\epsilon}_L \cdot \mathbf{A}_{Fm}^{F'm'} = \frac{i \sin \theta_L}{\sqrt{2}} \left((\mathbf{A}_{Fm}^{F'm'})_1 + (\mathbf{A}_{Fm}^{F'm'})_{-1} \right)$$
$$+ \cos \theta_L \left(\mathbf{A}_{Fm}^{F'm'} \right)_0 . \tag{2.21}$$

We report line weights and cross-terms for the D2 transitions, ${}^2\text{S}_{1/2} \to {}^2\text{P}_{3/2}$, of alkali atoms and hydrogen with I = $1/2, 1$, and $3/2$ in tables 2.5, 2.6, and 2.7 respectively.

Table 2.5: D2 weights and cross-terms for I = 1/2 applicable to H, ^{11}BeII

F	F'	F''	$A_F^{F'}$	$B_F^{F'}$	$C_F^{F',F''}$
0	1		1/6	-1/12	
1	1	2	1/12	1/48	-1/16
1	2		5/12	-7/48	

Table 2.6: D2 weights and cross-terms for I = 1 applicable to ^{2}H and ^{6}Li,^{28}Na

F	F'	F"	$A_F^{F'}$	$B_F^{F'}$	$C_F^{F',F"}$
1/2	1/2	3/2	8/81	0	-4/81
1/2	3/2		10/81	-1/81	
3/2	1/2	3/2	1/81	0	2/405
3/2	3/2	5/2	8/81	16/2025	-14/225
3/2	5/2	1/2	1/3	-7/75	-1/90

Table 2.7: D2 weights and cross-terms for I = 3/2 applicable to ^{7,9,11}Li,^{21,23,34}Na, ^{39,41}K and ^{87}Rb, ^{7,9}BeII

F	F'	F"	$A_F^{F'}$	$B_F^{F'}$	$C_F^{F',F"}$
1	0	1	1/24	0	0
1	1	2	5/48	-1/48	-1/32
1	2	0	5/48	0	-1/48
2	1	2	1/48	1/1200	1/160
2	2	3	5/48	0	-7/120
2	3	1	7/24	-7/100	-7/400

Note that there is no angular dependence to the D1 terms, and therefore no dipole dependence ($B_F^{F'} = C_F^{F',F''} = 0$ for D1). Also note that $C_F^{F',F''} = C_F^{F'',F'}$, physically this is because scattering through F'' is indistinguishable from scattering through F' when the F'' and F' are overlapped within the natural width.

2.6 Correction for finite numerical aperature

Collection optics correction: If fluorescence is collected over all solid angle there is no polarization dependent modification to the line shape. The equations given in the text are valid for light scattered into an infinitesimal solid angle. Here we find the modification to the angular dependent part of the line weights and cross-terms due to the finite numerical aperture of the fluorescence collection optics

assuming that collection efficiency per solid angle is constant. For a given laser polarization $\hat{\epsilon}_L$, we may integrate over the final scattering directions $\hat{k}_s$ allowed by the collection optics (parameterized by θ_s, ϕ_s).

$$
\begin{aligned}
\hat{\epsilon}_L &= \sin\theta_L \, \hat{y} + \cos\theta_L \, \hat{z} \\
\hat{k}_s &= \sin\theta_s \cos\phi_s \, \hat{x} + \sin\theta_s \sin\phi_s \, \hat{y} + \cos\theta_s \, \hat{z} \\
\hat{\epsilon}_L \cdot \hat{k}_s &= \cos\gamma
\end{aligned}
\tag{2.22}
$$

Performing the angular integrations over the isotropic part, where $d\Omega_s = d\phi d\cos(\theta_s)$, we find

$$
\iint_{0,0}^{2\pi,\theta_C} d\Omega_s = 2\pi(1 - \cos\theta_C) \equiv S_0.
\tag{2.23}
$$

The angle dependent dipole part is scaled by

$$
\begin{aligned}
\iint_{0,0}^{2\pi,\theta_C} d\Omega_s P_2(\cos\gamma) &= \pi\cos\theta_C \sin^2\theta_C P_2(\cos\theta_L) \\
&\equiv S_2 P_2(\cos\theta_L).
\end{aligned}
\tag{2.24}
$$

Here θ_C is the half angle of the fluorescence collection cone, and we assume that the detector efficiency is uniform for all solid angle. For determining experimentally relevant fitting functions, the ratio of the constant and dipole part is important, and we find that the dipole components are reduced relative to the constant components as,

$$
S_2/S_0 = \cos\theta_C \cos^2\left(\frac{\theta_C}{2}\right).
\tag{2.25}
$$

These scaling factors are included as part of the fitting functions to account for the numerical aperture of the imaging system. Failure to include these scaling factors shifts the extracted line centers by ≈ 6 kHz for $\theta_C = 26.6^\circ$ used in this experiment.

2.7 Conclusion

After investigating the Doppler free laser spectroscopy of alkali atoms with unresolvable hyperfine structure, we find that the effects of light polarization and quantum interference alter the relative line strengths and quantitatively affect the extraction of transition frequencies from data, even in the low intensity limit. Optical pumping effects at finite excitation power can further complicate the line shape, which we account for numerically. This leads to an improved determination of the ^{6,7}Li D2 line frequencies and splitting isotope shift. This effect may affect several species for which these complete line shapes will enable the next generation of measurements.

"There are no two level atoms and Cesium is not one of them." - W.D.P.

Chapter 3:   Excited to excited atomic transitions for laser cooling

Once a resonance as been identified spectroscopically, it is natural to ask how it may be used to manipulate atoms. In this chapter, we reexamine the light-matter interaction as a tool to control external motional states, rather than as a high precision probe for internal states. Specifically, we review an experiment that used the mechanical effect of light, scattered between two short lived excited states, to cool and confine Cesium atoms in a Magneto-Optical Trap [7]. This experiment led to a proposal to use excited state scattering to laser-cool magnetically confined (Anti-) H [8]. This chapter is organized as follows: we first review basic processes in laser cooling not only for their intrinsic value and applicability to quantum degenerate gas production but also so that they may be generalized to guide the interpretation of experimental results.

Laser cooling in its present state is a broad field applicable to ions, to neutral atoms (Li [60], Na [61], K [62], Rb [63], Cs [64], Fr [65], Mg [66], Ca [67], Sr [67], Ba [68], Ra [69], He [70], Ne [71], Ar [72], Kr [72], Xe [73], Cr [74], Yb [75], Ag [76], Er [77], Cd [78], Hg [79], Dy [80], Tm [81], and Ho [82].), and increasingly to molecules (SrF [83], YO [84], CH_3F [85]). Conceptually, it has also grown from Doppler cooling [86, 87] to include, polarization gradient [88–90],

velocity selective coherent population trapping [91], raman sideband [92–94], blue-detuned Sisyphus [95], "Pritchard-type" Sisyphus cooling of trapped particles [96], "Doppleron" [97] and numerous other cooling mechanisms. Despite this diversity, nearly all of the aforementioned processes rely on transitions between a long-lived ground state and an excited state. Some notable exceptions used an excited to further excited transitions to control the linewidth of Doppler cooling transitions [98–100] or create lightshifted darkspots allowing laser cooling to Bose-Einstein condensation [101]. However, useful mechanical effects from excited to further excited transitions are fairly rare [102]. The motivation for our exploration is manyfold. From a technical point of view, the development of robust and easy to use diode and fiber lasers invites experiments that may have previously been too ambitious. Additionally, we seek a cooling process where the cooling light and atomic florescence are nanometers different, enabling more efficient single atom detection useful for applications ranging from quantum gas microscopes [103] to atom trap trace analysis [104]. Finally, new cooling processes may further expand the applicability of laser cooling to as of yet uncooled atoms, ions, and molecules.

3.1 Traditional Laser Cooling

3.1.1 Dragged atoms and the optical Bloch equations

The general approach is to treat the atom-light interaction quantum mechanically (at least semiclassically) and treat the external degrees of freedom classically. This is justified if a single atomic wavepacket satisfies the Heisenberg inequality,

$\Delta \vec{R} \Delta \vec{P} \geq \hbar$, which can be fulfilled if the spread in position is small compared to a wavelength of light ($\Delta \vec{R} \ll \lambda_L$) and if spread in momentum is small compared to the natural linewidth,($\Delta \vec{P} \ll M \lambda_L \Gamma$). The assumption $\Delta \vec{R} \approx h/\sqrt{M_{atom} k_B T} \ll \lambda_L$, remains valid for heavy Alkali atoms into the $100\mu K$ range, however, one must be more careful when considering H or Li. When an atom satisfies these conditions the external coordinates maybe treated as classical parameters and the internal state response can be calculated. This is the dragged atom approximation.

In the following, we introduce the Optical Bloch Equations (OBE) to describe quantum mechanical internal state evolution and calculate relevant observables, namely the cooling (velocity damping) force and the momentum diffusion constant. The atomic Hamiltonian is modeled as a free particle with a single excited state $H_A = \hbar \omega_0 |e\rangle\langle e|$. The atom scatters light via electric dipole interactions $V_{A,L} = -\vec{d} \cdot \vec{E}$, and the electric field of the laser is $\vec{E}(\vec{R}) = \vec{E}_0(\vec{R}) cos(\omega_L t + \phi(\vec{R}))$ where the dipole operator is $\vec{d} = d\vec{\epsilon_z}(|e\rangle\langle g| + |g\rangle\langle e|)$ and the laser frequency is ω_L. We define the Rabi frequency, $\Omega(\vec{R}) = d\vec{\epsilon_z} \cdot \vec{E}_0(\vec{R})/\hbar$, that describes the coupling strength of the atom to the driving field. Making the transformation to the frame "rotating" with the laser, $\rho'_{ge} = \rho_{ge} e^{i(\omega_L t)}$ and $\rho'_{eg} = \rho_{eg} e^{-i(\omega_L t)}$, the Hamiltonian becomes time independent. We define the "detuning" as $\delta = \omega_L - \omega_0$. We can now write the simplified atom field in matrix form.

$$H = \hbar \begin{pmatrix} 0 & \frac{\Omega(\vec{R})}{2} e^{-i\phi(\vec{R})} \\ \frac{\Omega(\vec{R})}{2} e^{i\phi(\vec{R})} & \delta \end{pmatrix} \tag{3.1}$$

Thus far we have stated the Rabi problem, however, we must include the natural width to describe irreversible spontaneous scattering events necessary for cooling. This can be done phenomenologically using the optical Bloch equations where atomic coherences damp at a rate of $\Gamma/2$ and populations damp at a rate of Γ. The full equation of motion for the atomic density matrix has a conservative Hamiltonian evolution, the first term, and dissipative Liouvillian evolution, the last three terms.

$$\hbar\dot{\rho}(t) = -i[H, \rho] - \frac{\hbar\Gamma_{\mathrm{spon}}}{2}(c^\dagger c\rho + \rho c^\dagger c - 2c\rho c^\dagger) \tag{3.2}$$

Here, $c = |g\rangle\langle e|$, is the so called quantum jump or Lindblad operator that lowers the internal atomic state. The second and third terms in 3.2 act as if the Hamiltonian had an imaginary probability-nonconserving part. These terms, along with the Hamiltonian, constitute a possible description of photoionization dynamics induced by an optical field. The fourth term effectively restores the probability lost from the excited states back to the groundstate. Finally, the saturation parameter, $s = 2\Omega^2/\Gamma^2$, quantifies how much a transition needs to be driven, Ω, in order to overcome the loss from spontaneous decay, Γ. Note, the definition of s varies between references, see [90] vs. [105] for example.

3.1.2 Damping force

The expectation value of the force can be calculated in the standard way as, $\langle\vec{F}\rangle = -\langle\nabla H\rangle = \frac{i}{\hbar}\langle[H, \vec{p}]\rangle$. If we consider only the dissipative part of the force not derivable from a potential (because cooling cannot arise from a conservative
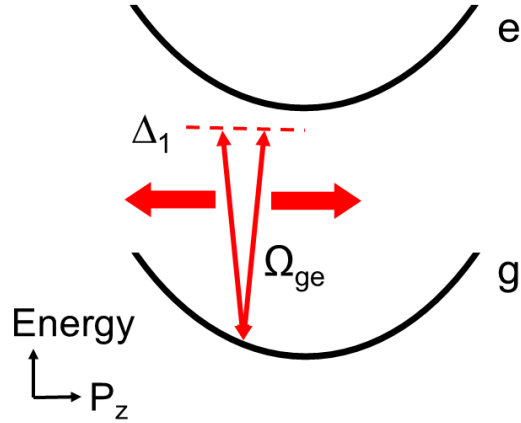
Figure 3.1: Damping force: The energy levels of a free particle. The Doppler shift from the motion of the atom relative to the cooling beams brings the counter propagating beam near resonance leading to increased scattering against the atom's direction of motion.

process), we find that $\vec{F}_{diss} = \hbar\vec{k}\Gamma\rho_{ee}$. This can be understood as the scattered photon momentum $\hbar k$ times the scattering rate for excited atoms Γ, times the population in the excited state ρ_{ee} (which is calculated from the OBE's). Since ρ_{ee} is, in general, a function of δ we can substitute $\delta \rightarrow \delta + kv$ to account for atomic motion. Such a process is schematically shown in fig. 3.1. For small velocities we can approximate the force as $f_z \propto -\alpha v$, which is damping for $\delta < 0$ (red detuning).

3.1.3 Momentum diffusion

The momentum diffusion constant describes the increase in the variance of the atomic momentum due to interaction with the electromagnetic field. Qualitatively, it can be interpreted as a random walk in momentum space with step size $\hbar k_{\mathrm{L}}$ and number of steps proportional to the population in the excited state times $\Gamma\delta t$.

Mathematically, the momentum diffusion coefficient is defined as,

$$2D = \frac{d}{dt}\langle (P(t) - \langle P(t)\rangle)^2\rangle = 2\int d\tau \langle \delta F(t)\delta F(t-\tau)\rangle \qquad (3.3)$$

where $\delta F(t) = F(t) - \langle F(t)\rangle$. The calculation of this two-time quantum mechanical correlation function is aided by the fact that the equations of motion for the two-time expectation values can be related to the solution for one-time expectation values. This result is known as the quantum regression theorem [106], see [105] and [107] for further discussion of the derivation. We briefly note that the momentum diffusion coefficient may be thought to originate from three different physical processes namely; fluctuations in spontaneous emission, fluctuations in photon absorbtion, and fluctuations in the dipole force. The last two processes can be nicely thought of in the nodes and antinodes of a standing wave. At the antinodes, the intensity is largest and the probability of being kicked due to absorption is highest but the gradient in the field, proportional to the kick, is near zero. At the nodes of the light, the situation is reversed. The probability of excitation is low but the momentum kick will be largest.

3.1.4 Doppler temperature

We can find the lowest achievable "Doppler" temperature by equating the momentum diffusion heating rate and cooling rates.

$$\dot{E}_{\text{cool}} = \dot{E}_{\text{heat}} \tag{3.4}$$

$$\vec{F}(v) \cdot \vec{v} = \frac{d}{dt} \frac{\langle (P(t) - \langle P(t) \rangle)^2 \rangle}{2M} \tag{3.5}$$

Now, we can solve for the temperature by equating it to the kinetic energy. This step is really only justified when a Maxwell-Boltzmann velocity distribution is generated by the cooling process. However, it is common practice to apply this definition in order to obtain an order of magnitude estimate even when the velocity distribution deviates from Maxwellian.

$$\frac{1}{2} k_{\text{B}} T = \frac{1}{2} M v^2 = \frac{D}{2\alpha} \tag{3.6}$$

At low intensity ($s \ll 1$) and low velocity ($\delta \gg k_{\text{L}} \cdot v$), we can use expressions for α and D to find the equilibrium temperature as a function of detuning,

$$k_{\text{B}} T = -\frac{\hbar \Gamma}{4} \left(\frac{\Gamma}{2\delta} + \frac{2\delta}{\Gamma} \right). \tag{3.7}$$

The minimum value is at, $k_{\text{B}} T_{\text{D}} = \frac{\hbar \Gamma}{2}$. For cesium and sodium the Doppler temperatures are 125μK and 240μK respectively. Remarkably T_{D} is independent of atomic mass, frequency of the cooling transition, and most other potentially relevant atomic properties. The dependence of the temperature on the scattering rate,
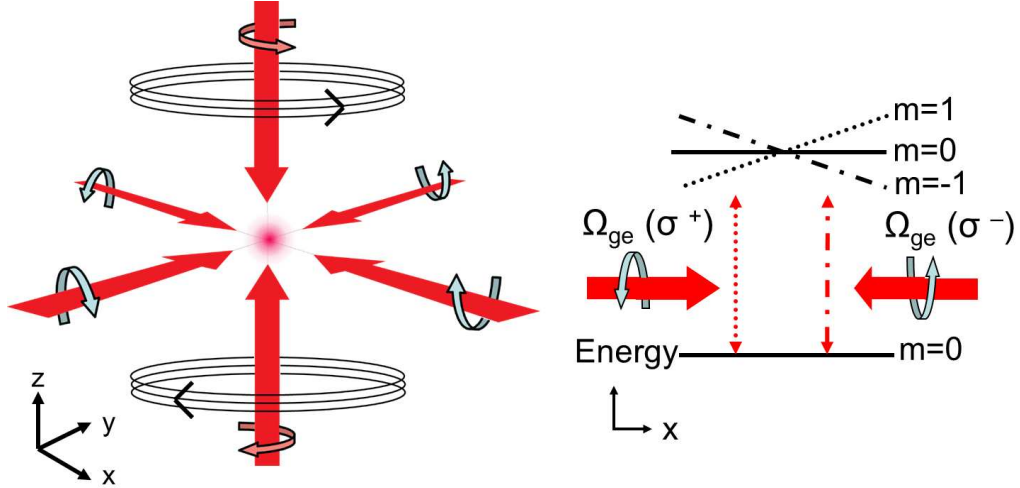
Figure 3.2: The physical layout and and energy level structure in a standard MOT. Six laser beams intersect at the field zero of anti-Helmholtz coils. Beams in the plane of the coils are σ^+ polarized w.r.t their propagation direction. The beams along the coil axis are σ^- polarized.

Γ, is somewhat easy to anticipate because the model relies on the scattering force that is intrinsically limited by the lifetime of the excited state. Measurements in agreement with the above two-level theory have only recently been made [108].

3.1.5 Magneto-optical trapping

We discuss a simple generalization to two-state laser cooling which enables robust trapping. The principle of the trap was proposed by Dalibard, implemented in [61] and, consists of applying an external magnetic field gradient to shift the Zeeman sublevels of the excited state of a $0-1$ atomic transition in a spatially dependent way, see the right side of Fig. 3.2. When the transitions are driven by red detuned spatially uniform circularly polarized light, atoms at the edge of the

trap are closer to resonance with the desired Zeeman sublevel and therefore, scatter light more efficiently, pushing the atom to the center of the trap. This spatially dependent trapping force combined with the velocity dependent damping force from optical molasses creates a trap that compresses atoms in phase space. The magnetic field used in this trap is a "spherical quadrupole" made using anti-Helmholtz coils. It is important to note that the primary atom-field interaction in a MOT is still $\vec{E} \cdot \vec{d}$ and not from the $\vec{\mu} \cdot \vec{B}$ interaction of the atomic magnetic dipole with the magnetic field. In common experimental conditions, the force from the magnetic field is two orders of magnitude smaller than the force from the laser field [109]. There are notable exceptions in the strongly magnetic lanthanides that can Magneto-optically trap using only one laser beam [77].

3.1.6 SubDoppler cooling

The measurement of "sub-Doppler" temperatures in both single [110] and multiple photon laser cooling [7](fig. 3.7) makes it clear that a more complete theory of laser cooling must be constructed. Since the Doppler limit depends only on the radiative lifetime, $\frac{1}{\Gamma}$, observation of sub-Doppler temperatures implies that there must be a longer relevant time scale. This time scale is the optical pumping time between Zeeman sublevels in the ground state. In fact, the temperature limiting process may now become scattering a single photon, or less if atoms are optically pumped into a dark state. The previous assumption of a two-level atom does not fully describe the behavior of atoms in a standing light field. To capture the dy-

namics of this motion-coupled optical pumping, we must include both the Zeeman sublevels and the polarization of the light.

There are several complementary models for sub-Doppler cooling by polarization gradients [88]. Among them are: $F = 1/2 \to F' = 3/2$ atoms with lin $\perp$ lin optical coupling (Sisyphus cooling), $F = 1 \to F' = 2$ atoms with $\sigma^+ \ \sigma^-$ optical coupling, and $F = 1 \to F' = 1$ atoms with $\sigma^+ \ \sigma^-$ optical coupling (velocity selective coherent population trapping). The first method is often discussed but rarely implemented, the second is often implemented but rarely discussed and the third is rarely discussed or implemented. I will attempt to give a bit of discussion about the second case.

The general theoretical procedure is to "adiabatically eliminate" the excited state and write equitations of motion for the effective-groundstate populations. This process gives the groundstate a finite linewidth which may be spatially dependent. Adiabatic elimination works when the excited state dynamics are fast compared to the ground state optical pumping time typically of order Γ.

In the case of the $F = 1 \to F' = 2$ atoms with $\sigma^+ \ \sigma^-$ optical coupling, there is no intensity dependence to the light field. It is always linearly polarized but, the direction of the polarization varies by 2π on the order of an optical wavelength. The coupling of the light field optically pumps the atoms to maintain an equal population in the $m_f = \pm 1$ ground states. However, motion in this light field preferentially populates one of the Zeeman states over the other. When the population in the Zeeman states is unequal the atom will preferentially scatter light from the counter propagating beam (due to non-adiabatic optical pumping rather than the Doppler

47
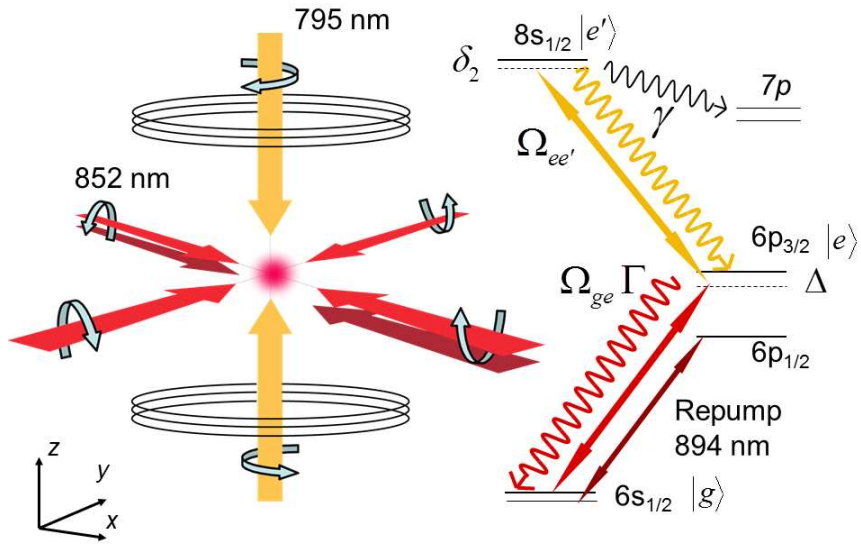
Figure 3.3: Cesium excited state laser cooling setup and energy levels. Here, Ω_{ge} and $\Omega_{ee'}$ are the Rabi frequencies of the laser couplings, $\Gamma/2\pi = 5.2\,\mathrm{MHz}$ and $\gamma/2\pi = 1.5\,\mathrm{MHz}$ are the linewidths of the $6\mathrm{P}_{3/2}$ and $8\mathrm{S}_{1/2}$ states respectively, and Δ_1 and δ_2 are the 1-photon and 2-photon detunings.

shift) and be cooled.

In the low intensity limit when the light shift (or optical pumping rate) becomes small, cooling eventually fails and this is known as "décrochage" (the atoms become "unhooked" from the light field).

3.2 Multi-photon Magneto-optical trapping of Cs

3.2.1 Setup and apparatus

The experimental setup consists of three external cavity diode lasers, which allow us to access the relevant levels in cesium shown in figure 3.3. The 852 nm laser is a home-built design (SDL-5411 G1 nominally producing 100 mW) which is locked 50 MHz above the 4-5 crossover saturated absorption feature of Cesium. The remaining three lasers are locked to the stabilized 852 nm laser via cavity transfer. The reference cavity (Thorlabs SA 200-7A Fabry Perot cavity FSR 1.5 GHz) length is first locked to the frequency modulated transmission peak of the 852 nm laser. The light from each of the remaining lasers (all were Sacher Lasertechnik Lynx Littrow model TEC 120 nominally producing 80 mW) passes through a fiber EOM (EO Space PM-0K5-10-PFU-PFU-850-UL-S, PM-05K-10-PFA-PFA-780-UL-S) which adds a sideband. The frequency modulated transmission peak of the sideband is then locked to the reference cavity, and the laser frequency sent to the experiment can be tuned by changing the EOM sideband frequency. The 795 nm laser was amplified to 500 mW using a home-built cage mounted tapered amplifier based around an Eagleyard (EYP-TPA-0795-00500-3006-CMT03) gain chip. The standard MOT beams were free space coupled and retro reflected. The 852 nm and 795 nm beams were combined on a Semrock dichroic mirror. Fluorescence or absorption images are recorded with a CCD camera.

The experimental chamber was quite simple, and based around a 3x3x8 cm
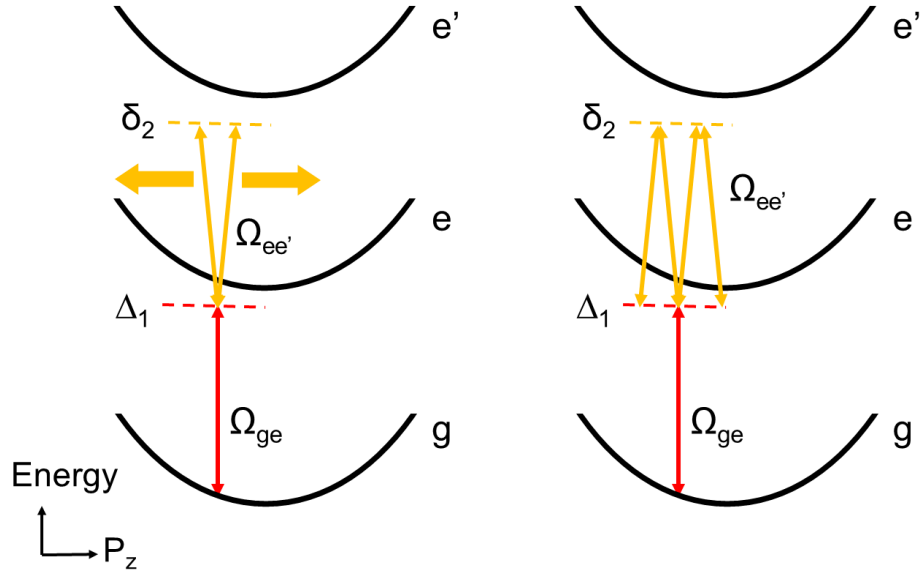
Figure 3.4: Two color damping forces. To the left an two-photon process and to the right a $2n + 1$ photon process (for the $n = 1$ case).

glass cell connected to an oven consisting of a needle valve connected to a 1 1/3"
heated($\approx$ 30C) bellows containing 1g ^{133}Cs metal. Connected to the experimental
cell and oven was a 4-way 2 3/4" conflat cross containing: a window (for probe and
repump beams), an Ion pump (Varian 911-5005), a 2 3/4" T which connected to an
ion gauge, and a gate valve turbo pump-out connection.

3.2.2   Two-color cooling

We may now generalize our understanding of Doppler cooling to include multi-
photon processes observed in our experiment. The first and simplest process is two-
photon Doppler cooling, illustrated on the left of fig. 3.4. Consider motion along
$\hat{z}$: a Doppler insensitive ground to excited state excitation in the $\hat{x} - \hat{y}$ plane is

followed by a Doppler selective momentum kick along $\hat{z}$ against the direction of motion. The scattering rate, eqn. 3.8, for the two photon process resulting in one unit of $\hat{z}$ momentum transfer, scales like the normalized product of single photon excitation rates times the scattering rate of the highest excited state γ.

$$R_{\hat{\mathbf{i}},\hat{\mathbf{j}}}^{(2)} = \frac{\gamma |\Omega_{ge}\Omega_{ee'}|^2}{16|(\tilde{\Delta}_1 - k_{ge}\hat{\mathbf{i}} \cdot \mathbf{v})(\tilde{\delta}_2 - k_{ge}\hat{\mathbf{i}} \cdot \mathbf{v} - k_{ee'}\hat{\mathbf{j}} \cdot \mathbf{v})|^2} \qquad (3.8)$$

where k_{ge} and $k_{ee'}$ are the wavenumbers of the laser beams, $\tilde{\Delta}_1 = \Delta_1 + i\Gamma/2$, and $\tilde{\delta}_2 = \delta_2 + i\gamma/2$. We define both ground and excited state saturation parameters as, $s_{ge} = 2\Omega_{ge}^2/\Gamma^2$ and $s_{ee'} = 2\Omega_{ee'}^2/\gamma^2$. From eqn. 3.8 we can verify that for $\delta_2 < 0$, the force along $\hat{z}$ is damping eg. $f_z^{(2)} \propto -\alpha^{(2)}v_z$. This process only works on the red side of two-photon resonance as in the standard two-level Doppler cooling theory. Essentially, it is standard Doppler cooling after a first excitation to the intermediate excited state. Data showing the two-photon cooling process is shown in red in figure 3.5, where $s_{ee'}=40$ is the low intensity excited transition saturation parameter.

For higher intensity $s_{ee'}$, a new multi-photon process can dominate. In this process, an initial Doppler insensitive ground transition photon plus 2n Doppler-sensetive excited transition photons transfer momentum. The three photon version of this process is shown in right side of figure 3.4. Since the process happens at high intensity, the excited transition coupling drives Raman processes between the lower of the two excited states. This effectively adiabatically eliminates the highest excited state, thus the natural scattering rate for this process is Γ not γ. The

reduced population in the e' state adds an additional exciting feature. The cooling

process becomes independent of the sign of δ_2 as long as $\Delta < 0$. This is shown for

$s_{ee'} = 100, 150, 450$ in fig. 3.5. The three photon scattering rate is given by,

$$R_{\hat{\mathbf{i}},\hat{\mathbf{j}},-\hat{\mathbf{j}}}^{(3)} = \frac{|\Omega_{ee'}|^2}{4|\tilde{\Delta}_1 - k_{ge}\hat{\mathbf{i}} \cdot \mathbf{v} - 2k_{ee'}\hat{\mathbf{j}} \cdot \mathbf{v}|^2} \frac{\Gamma}{\gamma} R_{\hat{\mathbf{i}},\hat{\mathbf{j}}}^{(2)}, \tag{3.9}$$

with $R_{\hat{\mathbf{i}},\hat{\mathbf{j}}}^{(2)}$ as in Eq. (3.8). In this case, the momentum transfer multiplying this

scattering rate is $2\hbar k_{ee'}$ because there is a two photon process along $\hat{z}$. Again for

$\Delta < 0$, the three photon force becomes damping, $f_z^{(3)} \propto -\alpha^{(3)} v_z$.
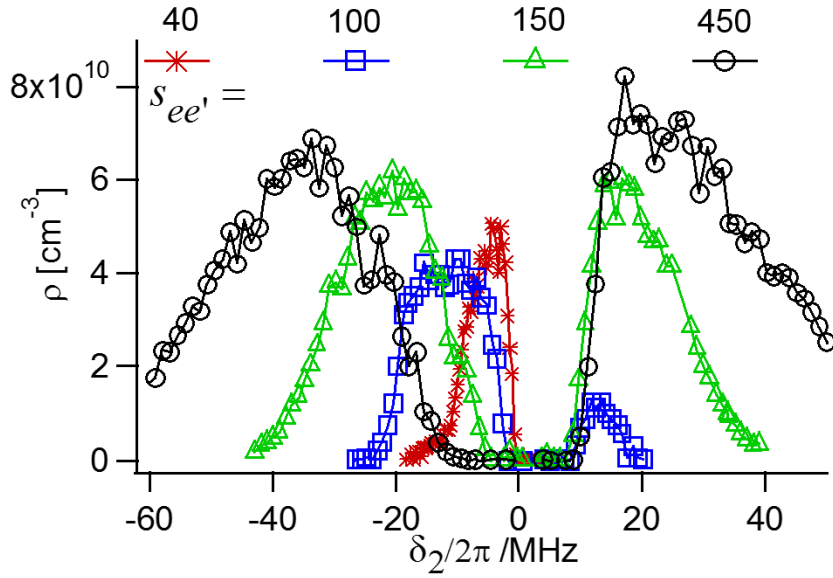
Figure 3.5: MOT density as a function of two photon detuning. At low saturation $S_{ee'} = 40$ (red) the cooling works as shown in the left side of figure 3.4. At high saturation the MOT begins to operate on the blue side of two-photon resonance, and over a wider range of detunings in agreement with the cooling mechanism described in the right of figure 3.4.
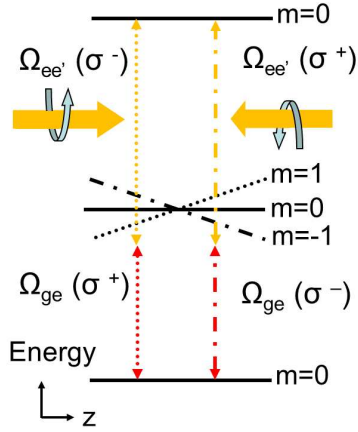
Figure 3.6: Two color trapping level diagram.

3.2.3 Two-color trapping

In figure 3.6, we consider the simplest excited state generalization to magneto-optical trapping using a $0-1-0$ ladder atomic system. Trapping along the axis with excited to further excited coupling light is an inherently two photon process. The atom must first absorb the in-plane ground to excited $0-1$ coupling light then it makes a $1-0$ transition to the spin 0 excited state. This reversal of angular momentum between the ground to excited and the excited to further excited state has the important practical consequence that the polarization of excited to further excited state coupling light must be reversed relative to the traditional MOT setup. However, like standard MOT's, the trapping is relatively robust against imperfections in the excited transition beam polarization and can tolerate errors in the quarter-waveplate axis by of order $10°$.

3.2.4 SubDoppler temperatures
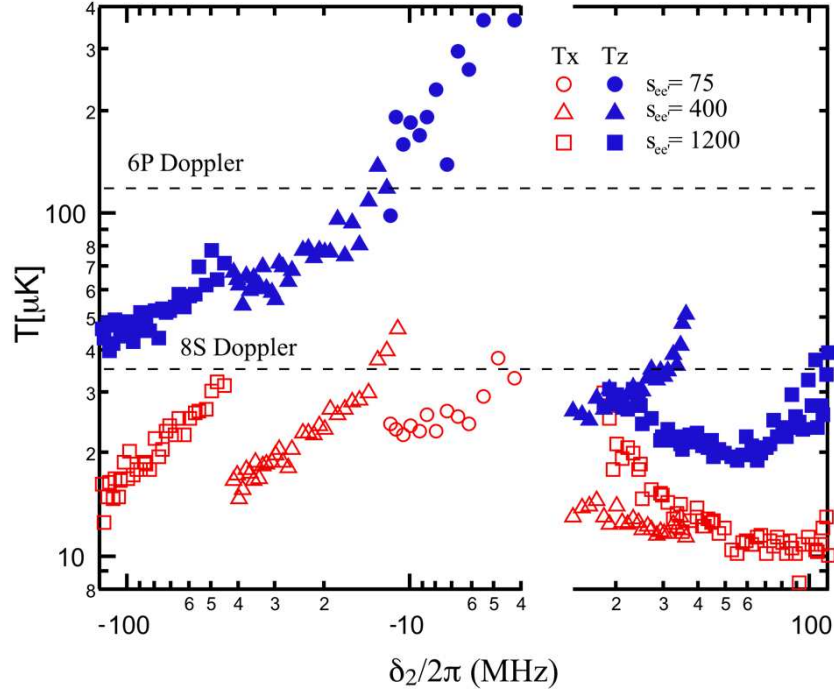
Figure 3.7: Temperature as a function of two photon detuning in a multi-photon MOT. The solid blue data points are along the $\hat{z}$ direction with e-e' coupling. The open red data points are in the $\hat{x} - \hat{y}$ plane with standard g-e coupling.

Surprisingly, we measure the temperature of the trapped cloud to be below the Doppler temperature. In a system with two excited states, there are Doppler temperatures associated with the natural width of each state. In our system $T_{D\ 6p_{3/2}} = 125\ \mu K$ and $T_{D\ 8s_{1/2}} = 36\ \mu K$. We measured the temperature of the cloud along the vertical and in-plane directions by imaging the atomic cloud after time of flight expansion and the data are summarized in fig. 3.7. For $\delta_2 > 0$ along the $\hat{z}$ direction, the observed temperature is below both of the Doppler temperatures.

One explanation of this observation is that the atoms are moving in a two color nonseparable dissipative optical potential and that subDoppler cooling in the

$\hat{x} - \hat{y}$ plane may be mixed into the $\hat{z}$ direction by the potential. Another theory is that the subDoppler temperatures are caused by two-color polarization-gradient cooling. An extension of [88] from a F=1 to F'=2 system to a F=1 to F'=2 to F"=1 system is an appealing minimal model of such a process. There are two key polarization configurations to consider, linear or σ^+, σ^+ polarization coupling F=1 to F'=2 with σ^+, σ^+ polarization coupling F'=2 to F"=1. Since the Hilbert space of this model is still rather large and the choice of states to adiabatically eliminate is not completely straightforward, we have explored this by numerically solving the OBE's and computing the expectation value of the damping force. In addition to a three photon Doppler force peak in the force vs. velocity curve, we find a smaller polarization gradient peak at a lower velocity in analogy with what is calculated in two level systems.

3.3   Excited-state Sisyphus cooling for trapped H($\bar{\text{H}}$)

While the laser cooling of atomic hydrogen is conceptually simple using the standard cycling transition, it is technically demanding. The lowest lying optical transition is still well into the vacuum ultra-violet at 121 nm. This makes traditional optical components, as simple as high reflectivity mirrors, quite difficult to obtain. It has been laser cooled but not as a proper MOT. Rather, it was cryogenically cooled to 1 K, then magnetically trapped, and finally laser cooled with optical pulses [111]. The concept of laser cooling H for precision measurement is appealing because there are many theoretical predictions that are orders of magnitude better

than present measurements. However, even more appealing and challenging is the precision measurement of $\bar{\text{H}}$ for comparison to H as a probe of matter-antimatter symmetry. The production of trapped $\bar{\text{H}}$ has recently been achieved [112–114]. It is far more challenging than the production of H because it is produced in such small quantities that traditional buffer gas methods would be impractical (and potentially could cause annihilation). Thus optical cooling is a likely starting point [115–117]. Even with a trapped $\bar{\text{H}}$ sample and a 121 nm source, the phase-space address-ability of Doppler cooling is extremely limited. In real space, it is desirable to have the cooling beam overlap the entire magnetic trapping volume, which places power constraints on the cooling laser. In momentum space, the cooling laser must be red-detuned of even the hottest, fastest-moving atoms allowing them to be cooled before the cooling light could be brought to address slightly cooler atoms. It is these constraints that motivate our proposal to laser cool H($\bar{\text{H}}$) using excited-to-excited state transitions.
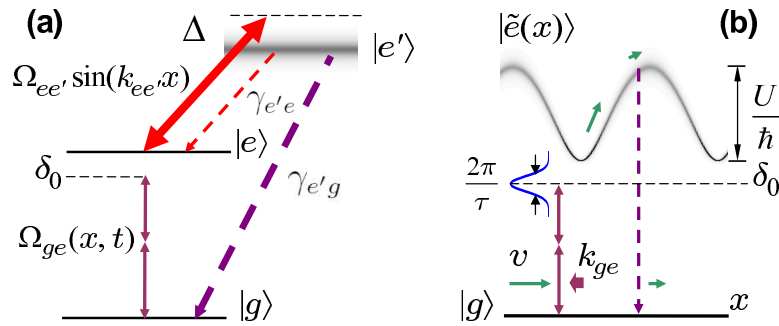
Figure 3.8: (a): Bare level diagram for the proposed cooling cycle (b): Relevant dressed-excited state and Doppler selective two photon excitation.

Our proposal utilizes a relatively general three level system shown in fig. 3.8. In it, a Doppler-sensitive pulsed two-photon excitation excites atoms into a relatively long lived excited state $|e\rangle$. The $|e\rangle$ state is dressed by light that couples to the short lived $|e'\rangle$ state. This creates a dissipative excited state optical lattice, shown in fig. 3.8-b, where the minima have long lived $|e\rangle$ character but the potential energy peaks have short lived $|e'\rangle$ character. This dressed state lattice preferentially scatters atoms that have climbed up potential hills. After another excitation pulse, the atoms will be preferentially returned to the bottoms of the potential to re-climb another hill as in the Sisyphus myth. In atomic H the levels are $|g\rangle = 1S_{1/2}$, $|e\rangle = 2S_{1/2}$, and $|e'\rangle = 3P_{3/2}$.

Figure 3.9 shows the real space configuration of beams forming the excited-state dissipative optical lattice; an approximation of the trapping volume, of the presently used magnetic trap at CERN. This configuration is appealing because the volume of the optical lattice is nearly the same as the trap volume and the visible lattice light at 656 nm is easier to generate and manipulate. The excitation to the lattice is a pulsed two photon excitation. There are two potential schemes to achieve this excitation, degenerate 243 nm radiation or a two-color (174.8 nm and 399.5 nm) pulse where one of the photons cannot photo-ionize H from the 2S state [118] (while this is more technically demanding, it does allow more cooling per photo-ionization event). Due to the pulse width, the pulsed excitation gives more range in excitation frequency thus addresses more momentum phase space, while the excited state lattice makes a larger cooling volume. Every cooling cycle removes both a $\vec{k} \cdot \vec{v}$ of energy from the excitation, and up to the depth of the e-e' lattice in

57
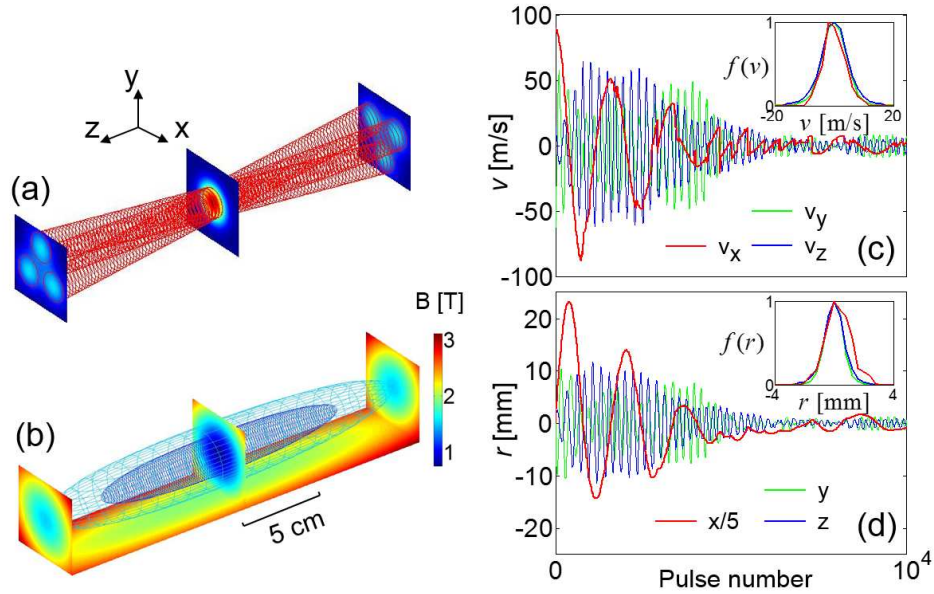
Figure 3.9: a) Excited state dissipative lattice beams b) Magnetic trap
c & d) Velocity and real space cooling trajectories for trapped H.

kinetic energy.

A typical velocity (and position) cooling trajectory is show in fig 3.9-c(d). Numerical simulation of three dimensional cooling is challenging because H is too light to justify the dragged atom approximation, allowing the problem to be separated into a classical kinematics problem and a three-internal state system. However, a fully quantum mechanical problem is too difficult due the large separation in atomic and trap scales. A semiclassical stochastic wavefunction approximation enabled suitable accuracy, by treating the motion as classical until a quantum jump from the excited state lattice occurs associated with a change in momentum of the classical trajectory.

In summary, pulsed excitation plus dissipative lattice cooling scheme could be

highly efficient. The simulation shows that $\approx 4 \; 10^4$ pulses can cool from ≈ 1 K to $\lesssim 10$ mK in three dimensions. If limited only excited state lifetimes the full cooling process could happen as quickly as 80 ms, however, the more likely limitation could remain available laser power. Even with reduced laser power, the cooling time could remain faster than Doppler cooling by several orders of magnitude.

Chapter 4: Experimental Setup and Construction

4.1 Preface to ultracold atom research

The following chapters describe the central effort of this thesis which was the construction and operation of an experiment to observe nonequilibrium quantum magnetism using ultracold atoms in optical lattices. The use of ultracold atoms to study collective quantum mechanical effects has been one of the most productive lines of research in atomic physics in the last 20 years, with numerous substantial achievements including Bose-Einstein condensation [119,120], production of a degenerate Fermi gas [121], BEC to BCS crossover [122–124], creation of an atomic Mott insulator in an optical lattice [125] and realization of a spin-orbit coupled BEC [126]. The general trends and long term goals are toward quantum correlated manybody systems. Current frontiers of this research include progress toward: fractional quantum hall physics via optical flux lattices [127], high spin symmetry [128, 129] and multi-orbital Kondo lattice model physics [130] enabled by alkali earth atoms, and the exploration of quantum magnetism utilizing a variety of approaches to generate long range atomic interactions [131]. In this thesis, we focus on using a dynamically controllable optical lattice to generate nontrivial manybody excited states and observe their time evolution. By using the optical lattice to tune single par-

ticle energy scales, we are able to observe super-exchange dominated dynamics in a 2D system. The following chapters describe the construction of an apparatus for the production of Bose-Einstein condensates, the setup and characterization of a dynamically controllable state dependent optical lattice, and finally, the study of manybody non-equilibrium dynamics.

4.2   Construction overview

In this chapter, we describe the design and construction of a third generation ^{87}Rb condensate machine. The design follows the apparatus described in [132] but, expands upon the former design by including a primary chamber for experiments using BEC's in a state dependent double well optical lattice, as well as, second science chamber including intra-vacuum optics to trap and image atoms in an optical lattice with 1 μm diffraction limited resolution. Full time work on this machine began in January of 2011 although planning of the tweezer chamber preceded this by a couple of years. As the sole PhD student working on this apparatus, I attempt to document all aspects of the apparatus for future generations of students and postdocs.

4.3   Vacuum system

4.3.1   Vacuum Chamber Design

The vacuum system, shown in Fig.4.1 is comprised of two separate vacuum regions; an oven, and a UHV zone separated by a differential pumping tube sur-

rounded by Zeeman slower coils. The UHV side of the vacuum contains the main science chamber, in which experiments in the double well optical lattice take place, and the tweezer chamber shown in Fig.4.2. The internal optical layout of the tweezer chamber is shown in Fig.4.3.

The base of the oven is a 1.33" conflat bellows containing 5 g of natural abundance Rb in a glass ampule, where the glass was broken under vacuum while being pumped by a turbo pump. In operation, it is heated to 85 °C by Aerotech twisted pair heaters. The bellows is then connected to a 1.33" "T" and 4" nipple (known for historical reasons as the bright-wall) which is kept at 105°C to prevent migration of the Rb metal from the oven to the rest of the system. Inside the bright-wall there is a standard copper pinch-off tube press fit onto a steel collimation tube for the atomic beam with a 40:1 aspect ratio. The bright wall is connected to a 4.5" Kimball Physics spherical octagon, the 4.5" flange of which connects to a 125 l/s ion pump (Varian VacIon Plus 150 Ion Starcel) of the same dimension to optimize vacuum conductance. Within the octagon, there is a copper "cold cup" to collect and sequester diverging parts of the atomic beam. A commercial Uniblitz shutter is torr-sealed to a Swage-lok mount which, is in turn, connected to another pinch off tube on the far side of the octagon to mechanically shutter the atomic beam. The cold cup is thermally contacted to the exterior of the vacuum chamber using a high current copper feedthrough which has been machined to mount to the cold cup. It is cooled outside the vacuum chamber by a Peltier cooler to -24°C. The hot side of the Peltier is, in turn, water cooled and flushed with dry nitrogen to reduce condensation/frost. Finally, there is a pneumatic gate valve interlocked to
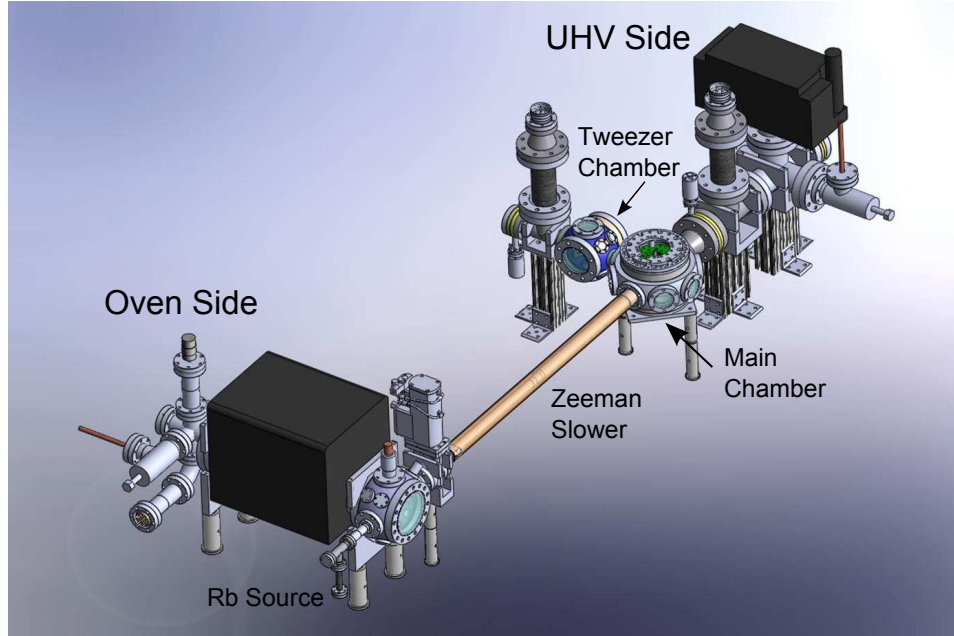
Figure 4.1: The bottom left side is the oven while the top right is the UHV.

an ion gauge to separate the oven assembly from the Zeeman slower. A custom 1.5"
long 1.33" diameter conflat bellows flexibly connects the slower to gate valve/oven
setup. The slower is a standard zero-crossing field design that has been used in the
laser cooling group on many apparatuses [133, 134]. Inside the slower field coils is
electronic heater tape used for Baking to UHV and a variable diameter nipple with
1.33"(2.75") conflat connectors on the oven (main chamber) sides.

The main science chamber used in this experiment is based around a spherical
octagon (Kimbal Physics MFC600-SO 200800) with eight 2.75" ports and two 6"
ports with recessed "Bucket" windows (custom made by UKAEA). The recessed
windows allow the magnetic trapping coils and optics to be placed as close as possible
to the atoms, increasing trapping efficiency and numerical aperture respectively. All
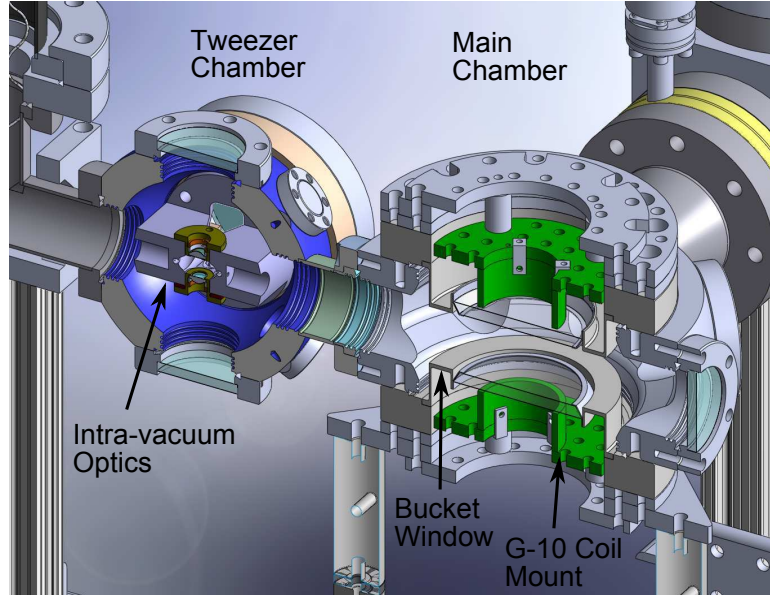
Figure 4.2: Cross section view of the UHV chambers. The main experimental chamber is on the right while the tweezer chamber is to the left.

windows are anti-reflection coated (by Lattice Electro Optics Inc.) at 780 nm, 810 nm, 1064 nm, and 1550 nm. The UHV chambers are designed to optimize the functionality of Ti-sub pumps (Agilent P/N 9160050) by placing them closest to the chambers to maximize vacuum conductance. The filaments are placed inside stainless steel bellows, so that under normal atmospheric pressure, the filaments will drop down into the main chamber. This maximizes the surface area that the sublimated titanium can coat. Hand rotatable baffles on feedthroughs can be rotated to block the line of sight to the windows and thus prevent the sublimated titanium from coating the vacuum windows inside the chamber. Under typical experimental operating conditions, the filaments are retracted out of the optical beam paths. Past the main chamber, Ti-sub pump is the UHV chamber ion pump (Varian Star
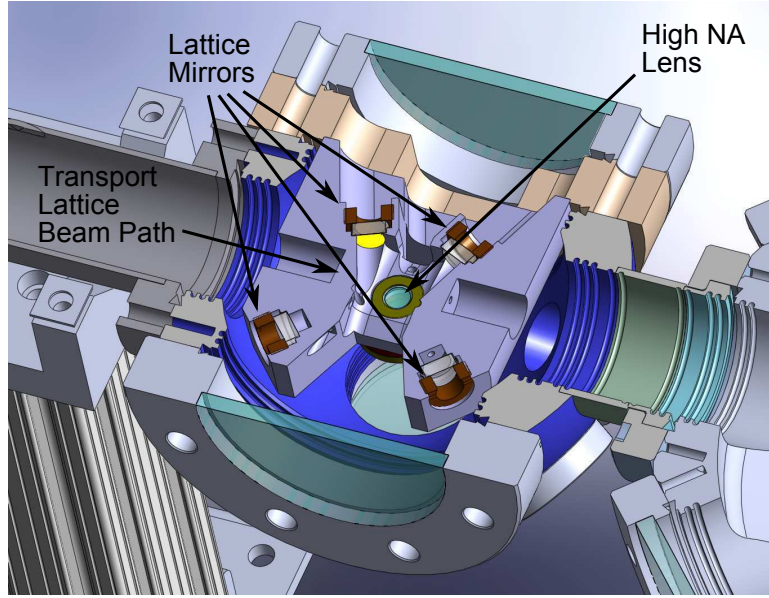
Figure 4.3: Cross section view of tweezer vacuum chamber.

cell with a speed of 55 l/s), an ion gauge, and a bakeable valve protected from atmosphere by a copper pinch-off.

4.3.2 Vacuum Chamber Assembly and Bake-out

In order to obtain trapped-atom-lifetimes that are not dominated by collisions with background gas atoms, we conduct our experiments at ultra-high vacuum in the 10^{-10} Torr range. We briefly outline our procedures for ultra-high vacuum preparation, construction, and pump-down/bake-out. *Prepare chamber parts, tools, and area:* Wearing nitrile gloves and face masks, acetone wash the un-waxed side of Al foil and apply to all workspace surfaces (dry with lint-free chem wipes as necessary). Next wash all vacuum chamber parts in an acetone ultrasonic bath. Wrap all parts in clean foil and air bake at 400 F for a week. This creates a chrome-
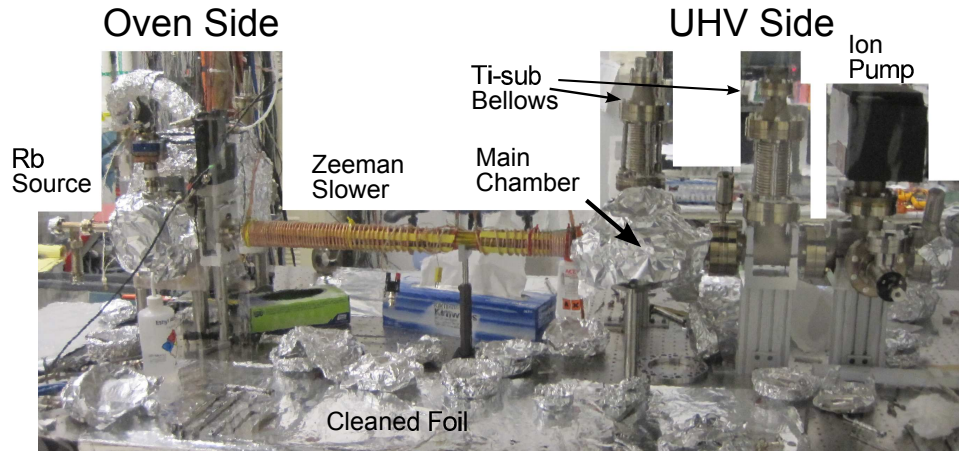
Figure 4.4: The nearly completed vacuum chamber.

oxide layer near the surface which makes the steel less permeable to hydrogen [135].

Assembly and bakeout preparation: Re-clean parts in an ultrasonic bath and cover the optical table with cleaned foil as shown in figure 4.4. We assembled the chamber using silver coated bolts and standard conflat flanges with copper gaskets. We were careful to keep the knife edge of the conflat clean and defect free, as well as, to mount rotatable flanges to fixed flanges to ensure enough degrees of freedom to line up bolt holes. To ensure that the copper gaskets were evenly compressed, we tightened bolts in an alternating sequence depending on the number of bolts on the flange. For example in a six bolt flange the sequence would be; 1, 3, 5, 2, 4, 6, 3, 5, 1, 4,... We compressed the copper gaskets until there was steel to steel contact. Once the system is sealed up, we leak checked the chamber by pumping the system down using a turbo pump (Pfeiffer Vacuum HiCube 80 Eco) and an RGA (Dyson/AMETEK Quadrupole gas analyzer model MD014110-1, or SRS RGA 100) and applying either Acetone or Helium to suspect vacuum connections. If Helium was applied we would
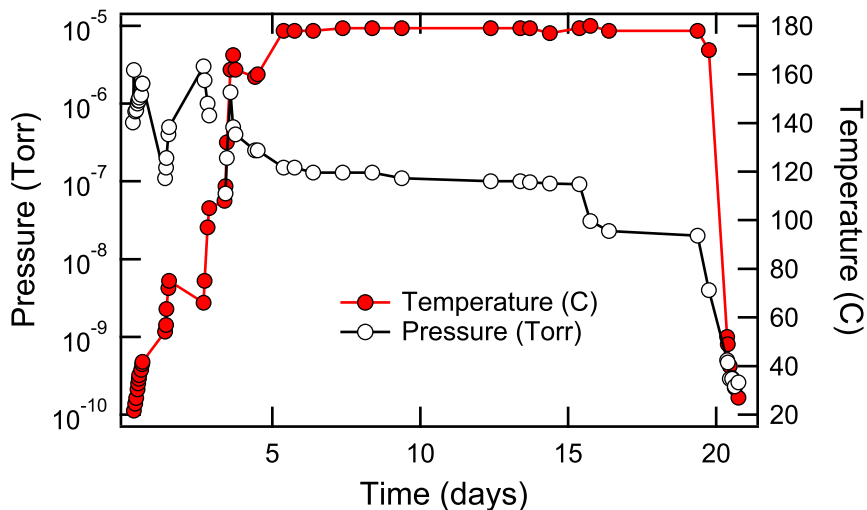
Figure 4.5: Vacuum chamber pressure and temperature during bake, t=0 corresponds to day 0 in the table of notes on bake out.

look for a peak in He partial pressure on the RGA. However, if acetone was applied we would look for a dip in pressure as the large molecules temporarily filled the small leaks.

Bake: Once there were no obvious leaks, we baked-out the chamber to remove residual Hydrogen and impurities like water. Since our chamber is too large to fit in an oven, we wrapped the chamber in Al foil, then heater tape (being careful not to layer heat tape on itself), and finally, with more Al foil to create our own oven. We control the temperature of the heater tape using Variacs and monitor it in many different locations with K type thermocouples on a 16 channel thermocouple monitor (SRS model 630). To monitor thermal gradients across the chamber, there was about one thermocouple per piece of heater tape. We typically heat at a rate of less than 3 C per ten minutes and limit the maximum temperature to $< 200°C$

67

Table 4.1: UHV pump down and bakeout procedures.

Day	Notes
-5	Turbo pump vacuum
-4	at 10^-6 range, start RGA(s) and degass all ion gauges $\approx$1min
-2	Degas ion pumps, turn ion pumps on by "burping": run at 3kV until high current $(2*10^-2$ A), turn off, run at 5kV until high current, turn off, then run at 7kV until high current, finally drop down to normal operating voltage 3kV or 5kV
-1	Degas all Ti:sub filaments
0	room temperature under turbo pump vacuum, begin bake (gate valve between oven and UHV closed)
15	degas ion gauges, ion pumps, and Ti:Sub filaments
21	hand tighten bakeable valve, start cooling, and degas ion gauge at lower pressure
22	cold, open gate valve

to protect the glass to metal view port seals and A/R coatings. See figure 4.5 for temperature and pressure as a function of time and see table 4.1 for additional notes on the bake. During the bake we periodically checked the in-vacuum shutter to verify its functionality. When cooling down the chamber, the pressure is anticipated to drop below the limit of the turbo pump so, we separate it from the rest of the UHV system by closing the bakeable valve. If the bakeable valve is tightened while hot, it will not be reusable. We have found that "hand tight" is sufficient to separate the turbo pump vacuum from the UHV side during the cool down. When cool, we tightened the bakeable valve to 15 ft-lbs using a torque wrench.
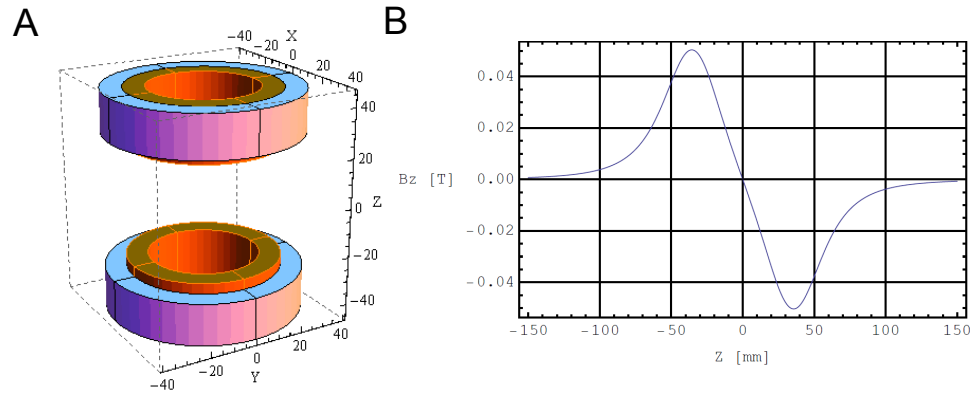
Figure 4.6: A) Quadrupole coil geometry (all dimensions in mm). B) Magnitude of the z component of the field along the z axis(axis of the quadrupole) for a 150 A current.

4.4 Magnetic trap

4.4.1 Coil design

We use a quadrupole magnetic field to confine atoms during the early stages of evaporation while they are still, on average, too hot to spin flip near the trap field zero. These coils also provide the magnetic field gradient for the MOT. The coils were wound using square cross-section hollow copper tubing and the main constraint was the size of the vacuum chamber, which was primarily determined by the internal size of the "Bucket" windows and by size of the MOT beams/longest desirable time of flight for imaging. The coils were mounted in a machined G-10 fiberglass coil form to reduce eddy currents induced during switching of the field. The quadrupole coil geometry (pictured in Fig.4.6 A), consists of two inner layers with 5 turns and two outer layers with 4 turns. The field was simulated using the Mathematica package

69

"Radia" and is plotted in Fig.4.6 B. Near the center of the trap, the magnetic field gradient is 10.5 mT m^{-1} A^{-1} (or 1.05 G/(cm A)). Due to the closer proximity of the coils to the atoms, this is more than a factor of 2 improvement than the apparatus in [132]. We used the following coil winding procedure: 1) Cut $\approx$4 m (number of turns + leads) of square cross section coil. 2) Fix coil form to flat surface elevated off of table such that the coil winding guide tool can clear above the table (since we use square tubing the orientation of the coil must be controlled using a coil winding guide). 3) File the corners on coil form and cover it with Kapton tape so that the coil's insulation will not be harmed during winding. 4) Clamp the coil onto the bottom of the coil form, on the side opposite to the hole, through which the leads will pass when completed. 5) Wind the coil up the form keeping the square tubing correctly oriented while maintaining tension on the coil (this is a 2 person job, one person to guide, and the second person to maintain tension). 6)Bend the coil out of the hole for the leads at the top of the coil form (a half inch post makes a good bend radius). 7)Apply a layer of epoxy to the outside of the first layer of wound coil. 8)Repeat steps 5-7 for all remaining layers of coil.

4.4.2   Fast switching high current source for magnetic trapping

The MOT and magnetic trap coils are the same, which eliminates transverse magnetic trap alignment issues, present in Ioffe-Pritchard traps, as the atoms from the MOT are transferred to the magnetic trap (Gravitational and radiation pressure imbalances can complicate this picture, nevertheless it is preferable to the previous

Ioffe-Pritchard design). However, this method of BEC production also requires that the field coils must be switched as fast as possible from $\vec{B} = 0$ during the optical molasses stage to their maximum magnetic trap depth during the beginning of RF evaporation. This is a classic technical problem for ultra cold atom experiments with numerous solutions. Our setup uses a current supply (Agilent 6690, 440 A, 15 V) operated in constant voltage mode at 15V as the current source. The current is sensed by Hall probes (Danfysik 866) and is fedback to control the current, using a water-cooled MOSFET bank, shown in figure 4.7. The bank is designed to split the ≈ 400 A (in practice we limit the computer control request current to 155 A) from the supply across 20 MOSFETs rated for ≈ 30 A. The resistance of the MOSFET bank is controlled by a PID circuit which is buffered, in order to overcome the substantial parallel gate capacitance of the MOSFETs. The set point of the PID is computer controlled by an analog output from a NI 6733 with 16 bit resolution. Since control, monitoring, and field coils are in a different room from the PID and current supply, ground isolation of the PID is important to manage ground loops. The characteristic switching time is 1 ms. All of this system, except for the field coils, is located outside of the lab in a service corridor to better separate the thermal, acoustic, and magnetic noise from the main experiment.

4.4.3 Plumbing

The heat generated by resistive current flow in the magnetic coils, typically on the order of a kW, must be dissipated by chilled water. The block diagram
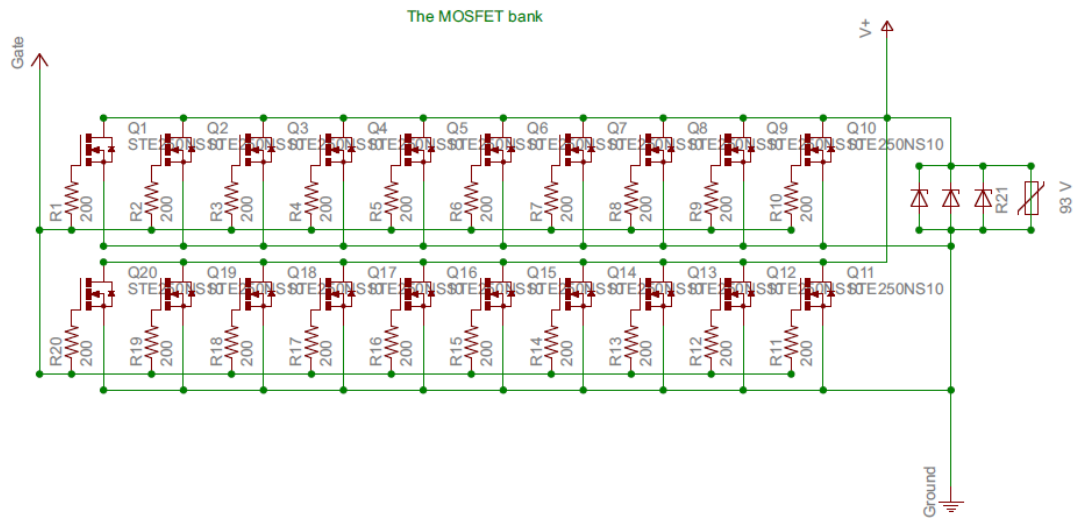
Figure 4.7: MOSFET bank schematic. Components: MOSFETs Q1-20; STE250NS ≈30A max each, Resistors 1-20; 200Ω, Zener diodes labeled "R21"; 93 V zener diode, "93 V"; 93 V varistor. The Zener diodes and varistor are for suppression of transient voltages during switching. The gate voltage is the output of the PID locking circuit, while V+ comes from the Agilent 6690 through the experimental coils.
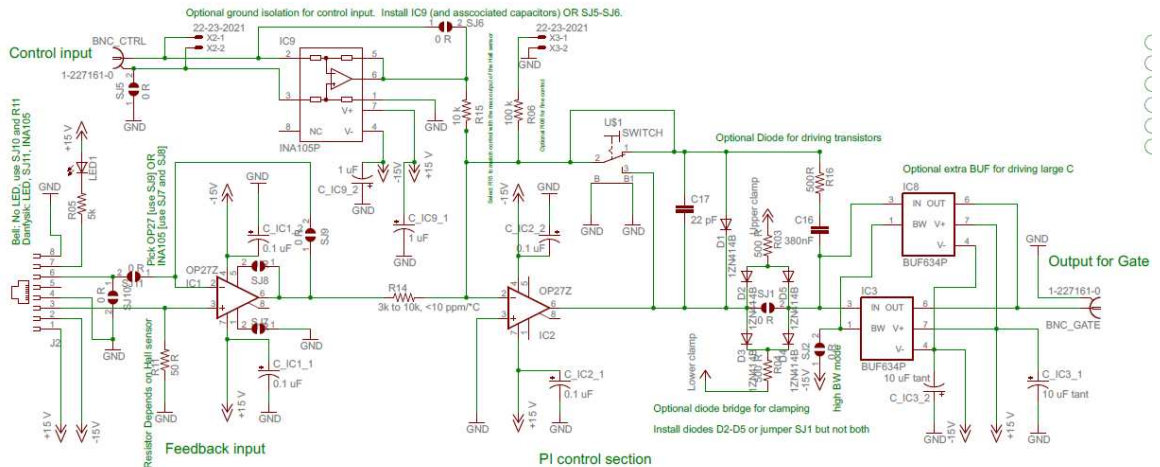
Figure 4.8: MOSFET servo.
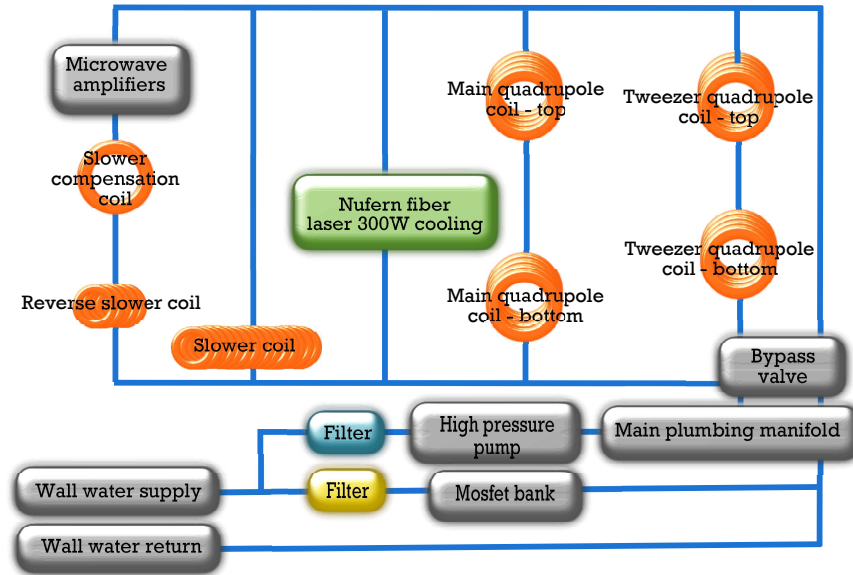
Figure 4.9: Block diagram of plumbing system.

of the complete plumbing system is shown in Fig.4.9. Filtered pressurized (pump: Dayton model 9k862A) wall water is sent to a main manifold where it is split off to two sets of quadrupole coils, Zeeman slower coils, a fiber laser amplifier, and microwave amplifiers. To cool more efficiently, the water is run in parallel through the quadrupole coils. On the lower pressure return side of the system, we use Proteus 100C110 flow switches to monitor the flow rate. The outputs of the flow switches are interlocked together and drive a reed switch giving the necessary open-closed logic to the quadrupole current supply (the logic of the current supply is such that an open circuit allows current to flow to the coils so care must be taken to never disconnect the reed switch from the power supply).

A manifold to organize and secure large high current electrical+plumbing connections is shown in Fig.4.10. It is designed in modules of two connections (supply
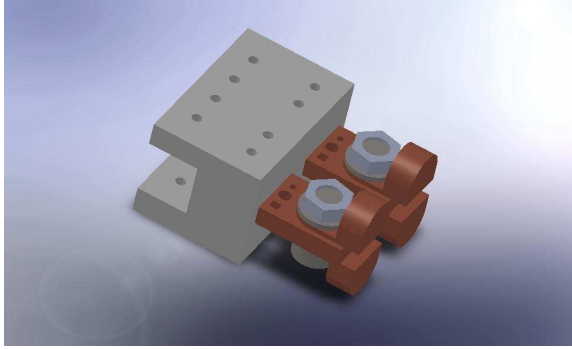
Figure 4.10: A single supply/return module of the electric to water connection manifold.

and return) can be scaled for different experiments. The plastic manifold (gray) fits around 1010 80/20 and has slots on the front to hold 2 copper pins. The copper pins slide into the plastic and are bolted in from the top. The copper pins have holes for multiple common sizes of coil (1/8" round 1/4" round and .17" square tubing) and for bolting on high current lugs.

4.5   Laser cooling optics

4.5.1   MOT beams

In order to create a compact and robust quantum gas production system, our MOT beams are produced on a separate optical table and delivered to the experimental chamber via optical fiber. MOT beam shaping and polarization control are achieved in a simple package shown in figure 4.11. The light emerging from the fiber is circularly polarized with a quarter wave plate, then expanded through a plano-concave f=-25mm lens, then collimated by the combination of a f=150 mm
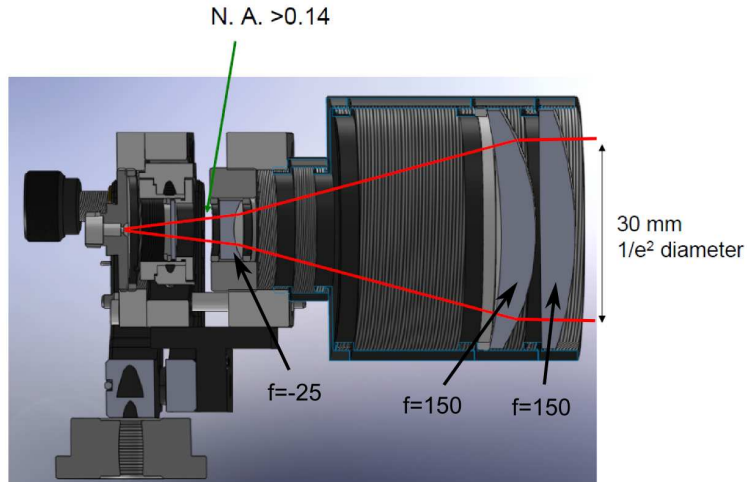
Figure 4.11: MOT launch optics package. The red lines indicate approximate rays of the MOT beams.

meniscus lens and a f=150 mm plano-convex lens. The entire package is kinematically adjustable and is mounted on the bottom of the second story instead of directly on the first level breadboard to preserve space on our breadboard. The beams are periscoped downwards off retractable pneumatic mirrors and into the chamber.

4.5.2 Pneumatic mirror system

Most of this subsection is from the author's manuscript [9], in which we describe a pneumatically actuated mirror system with long term repeatable sub-milliradian pointing stability ensured by a 3-point kinematic positioning system. This system is easily capable of moving 50 mm (2") optical components nearly the full throw of a pneumatic piston cylinder in < 1 s (≈ 36 mm to 50 mm for the designs presented, though longer actuation distances could be achieved with
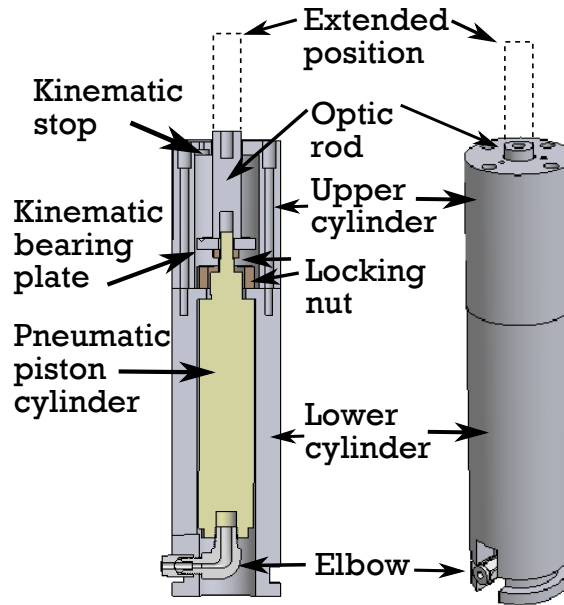
Figure 4.12: Cross section and assembled view of vertically oriented and translating optic mount. The 12.5 mm (0.5") diameter optic rod and piston connected to it below are shown in the compressed position. The post can be extended the to the full throw of the piston minus a small amount of translation to ensure that kinematic contact is made. The piston throw is 38 mm (1.5") and the throw of the actuated post is 36 mm (1.42"). In the extended position, the kinematic bearings are coincident with the kinematic stops. The upper cylinder, lower cylinder, kinematic bearing plate, and optic rod are custom parts. The pneumatic piston cylinder, elbow, and locking nuts are standard commercial products.

straight-forward modifications). The vertically oriented design occupies the same space on an optical table as a typical 38 mm (1.5") post, is compatible with fork-type optical clamps, and its actuation requires no additional space on the optical table. The system components are relatively inexpensive and cost < \$1200 for a set of 4 vertical and 2 horizontal units. The motivation for this project comes from the long term failure modes of commercially available "flipper" mounts used in [132].

The vertically-oriented design, shown in FIG. 4.12, is based on a single-acting

spring return pneumatic cylinder with a 1.5" throw (SMC Corporation NCMKB088-150CS) [1]. The overall height of the assembly and choice of piston throw are determined by the height of the beam above the optical table (which in our case is 25.4 cm (10")) and by the size of the optic to be actuated (50 mm (2") elliptical gold mirrors), respectively. The assembly includes 4 custom designed parts: a lower cylinder, an upper cylinder, a kinematic bearing plate, and an optic rod. The piston is housed in the lower cylinder of the assembly which contains a center hole for mounting the piston, four threaded holes to mount to the upper cylinder, and a flange around the bottom compatible with standard fork optical clamps. The piston is secured to the lower cylinder by a locking nut included with the piston. The piston actuates a 12.5 mm (0.5") diameter optic rod threaded for mounting to optics and a kinematic bearing plate with three ball bearings to create a repeatable stable mechanical structure [136]. The kinematic bearing plate is fixed in place between a locking nut (bottom) and the optic rod (top). When extended, the three ball bearings of the kinematic bearing plate make contact with the kinematic stop hardware screwed into the upper cylinder. We use standard three point kinematic stops with three distinct pieces: a cone, a flat, and a V-cut groove (Hitek Hardware; KC-1032-TH, KF-1032-TH, and KS-1032-TH).

The horizontally-oriented design is based on a horizontally-mounted pneumatic cylinder (SMC NCMR106-0200CS) and a commercially available linear guide rail and carriage system (IKO Nippon Thompson; LWLF14R150BPS2 and

---

[1] All product names and part numbers are for specificity only and do not constitute an endorsement by the authors or their parent institutions.
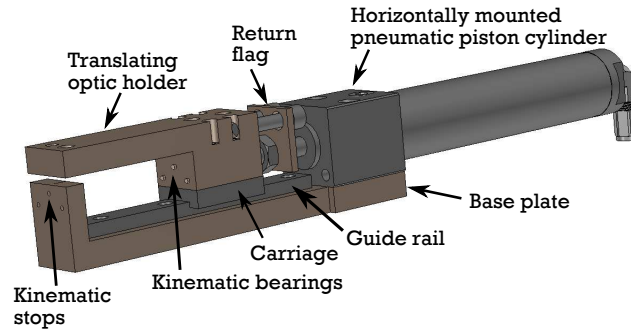
Figure 4.13: Horizontally oriented and translating design. The carriage and piston are shown in the compressed position. In the extended position, the kinematic bearings are coincident with the kinematic stops and the carriage assembly is repeatability positioned. The carriage can be translated by nearly the full throw of the piston $\approx$ 50 mm (2"). The base plate, translating optic holder, and return flag are custom designed. The carriage, guide rail, and pneumatic piston cylinder are commercially available.

LWLF14C1BPS2). The design includes three custom pieces shown in FIG. 4.13.

The first is a monolithic base plate containing threaded mounting holes for the horizontally oriented piston, pedestal mounts, and linear guide rail, as well as, a three counter bores to hold the kinematic hardware as discussed in vertical design. Next, the translating optic holder is designed to be mounted on the moving carriage and has threaded holes for the specific optic mount to be translated. It also contains three press-fit ball bearings to make the necessary 3-point contact with the kinematic stops. The end of the piston, padded by a rubber stopper, presses on this piece in the extended position. The final custom piece is a return flag which allows the carriage to be retracted by the piston. As the piston retracts, the flag catches on a nut around the piston.

The pneumatic control system uses laboratory compressed air regulated to

330 kPa (48 PSI) to minimize the vibrational disturbance of other optics while maintaining a reasonable actuation time. An electrically controlled solenoid valve (SMC VQC2101-5 mounted to SMC VQ2000-PW-02T) switches the air to a 6 way splitter (SMC KQ2ZT01-34S) for all pistons simultaneously. Most exhaust gas is released at the solenoid valve through 35dBA silencers (SMC AN202-02) which can be located meters away from the experimental chamber, reducing acoustic noise and air currents, as well as, electrical noise associated with the switching of the solenoid valve. We use 5/32" OD tubing before the splitter ($\approx$ 3 m) and 1/8" OD tubing between the splitter and the pistons ($\approx$ 1 m). The solenoid valve is TTL controlled so that pistons can be synchronized with the rest of the experimental cycle. It is important to consider interlocking the position of the piston with respect to the on/off state of the other beams behind it. This can prevent safety hazards associated with unintentionally scattered laser light or, in the case of higher powered beams, damage to the piston and optics on it. In our experiment, we accomplish this by interlocking the piston TTL signal to the high-power dipole trapping beam TTL signal.

We characterize the mechanical stability of the mounts in terms of the position stability of the optical beams they actuate (which, for example, would lead to intensity/number fluctuations in a MOT). To make position stability measurements path length independent, we measure the angular pointing stability. We reflect a collimated 635 nm laser beam from a single-mode fiber with a $1/e^2$ beam diameter of 700 μm off the actuated mirror, and image the position of the beam on a CCD beam profiler [137,138]. In all test measurements, the mirror was an elliptical 25 mm (1")
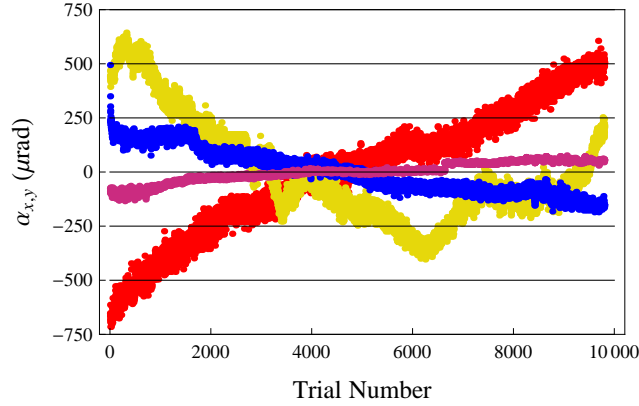
Figure 4.14: Pointing stability of pneumatic mirrors; The points are the x, y angular displacements, $\alpha_{x,y}$, in μrad (corresponding to spatial displacements < 1.5 mm, while the length of a CCD pixel was 6.4 μm) of the peak centers on the CCD located 165 (1) cm away from the actuated mirror. The vertical pneumatic design is in blue along x and violet along y while the horizontal pneumatic design is in red along x and yellow along y.

diameter gold mirror epoxied onto a 25 mm (1") diameter post angled at 45° which weighed ≈ 45 g (the 50 mm (2") elliptical gold mirrors used in the apparatus are ≈ 100 g). An individual position measurement cycle is 4 s with 1.6 s to actuate the mirror and allow vibrations to damp (the vibrations on the optical table were measured to damp out in < 100ms using an accelerometer) , then a 100 ms exposure on the CCD, 300 ms dark time, and another 2 s to retract and stabilize the mirror. This cycle was repeated 9800 times over ≈ 12 hrs where the temperature in the room was 21^oC and fluctuated by $\leq 0.5^oC$. We estimate the angular pointing stability from the spread of the data points in FIG. 4.14 and the beam path length from the pneumatic mirror to the beam profiler, 165 (1) cm (In the experimental apparatus, 30 cm beam paths are used.). We also estimate "short term" pointing

stability by binning the data into 100 shot intervals and computing the standard deviation for each interval. Averaging over all collected intervals, the short term standard deviation is less than 35 μrad while, the standard deviation of the worst 100 shot interval was 300 μrad. As a final more qualitative discussion of repeatability/durability, we note that our system of four vertically oriented cylindrical mirrors has functioned successfully for more than 2 years without replacement of any mount components. We tweak up the alignment of the mirrors every 2 to 4 months.

4.5.3   Zeeman slower beams

The collimated output of polarization maintaining fibers for the slower cooling (3 mW) and repump (7 mW) are combined on a PBS followed by a quarter wave plate that circularly polarizes the cooling light. A f=-25 mm and 150 mm lens system expands the beam after the second lens and slowly focuses the beam approximately 145 cm from the slower entrance vacuum window, which puts the focus just before the gate valve separating the oven from the slower coils. The optical system is mechanically secured using cage hardware and attached to the chamber with a custom flange that contains a bolt circle for both the vacuum bolts, as well as, threaded holes for 60 mm cage hardware, which simplifies the alignment process.

4.5.4   Imaging system

We image the atoms by absorption of a collimated resonant probe beam with an intensity below saturation. We have imaging systems along two directions. In one

direction the probe beam propagates vertically downwards to image the behavior of the atoms in the 2D horizontal plane. The images are formed by two lenses: A f=100 achromatic lens (25 mm aperture) at focal distance after 27 ms TOF of the atoms and a f=400 mm plano-convex lens (50 mm aperture) at focal distance to the image plane, a CCD camera (Princeton Instruments). The distance between the lenses is about 10 cm. This system has a field of view of $\approx$ 1.25 mm radius, a focal depth of $\pm$ 450 μm , and a numerical aperture of 0.13. The focal depth should not be reduced to image the 3D BEC sharply as there are stigmatic aberrations. The second direction of imaging is $\approx$ 5 degrees off of the tightly confining dipole beam and images the vertical and one in plane direction. This imaging system is two f=400 mm (25 mm aperture) plano-convex lenses, which form a condenser lens, which images the atoms onto a second CCD camera (Point Grey Flea 3). This imaging system has a field of view radius of 8 mm and a focal depth of $\pm$ 800 μm. We experimentally calibrated the magnification of the imaging system to be $\approx$ 0.98 by watching atoms fall from rest under gravity to determine a well defined length within the vacuum chamber. All lenses are aligned by overlapping the different reflexions from the lenses on the incoming beam.

4.6   Laser systems

4.6.1   Cooling lasers

Our cooling/probing laser system consists of three lasers; a master frequency reference laser (New Focus Vortex 6013) locked to the ^{87}Rb F=2 to F'=2-3 crossover

feature created by saturated absorption spectroscopy (see for instance [139] and references therein), a cooling laser (Toptica TA pro) beatnote locked [140] to master near the F=2 to F'=3 transition ($\approx$ 780.246nm, $\approx$1.23 W) and finally a repumping laser (Toptica Dl-100) also beatnote locked to master near the F=1 to F'=2 transition ($\approx$ 780.235nm, $\approx$60 mW). This reference laser plus beatnote locking system is quite flexible and allows the frequency of the light sent to the experiment to be dynamically changed via a voltage controlled oscillator reference during the experimental cycle. [See fig. 4.15 for a detailed level diagram including all beam paths and relevant AOM offsets. To control the intensity of near resonant light to the experiment, all beams are AOM-switched and shuttered (to insure essentially perfect extinction). The full optical layout for the three cooling lasers is shown in Fig. 4.16 [2]. All lasers are boxed to improve eye safety, thermal stability, and to prevent stray scattered light from interacting with atoms in the science chamber. All light is fiber coupled to the experiment, separating experimental and "supply" side alignment problems.]

4.6.2   Dipole trapping laser system

In order to achieve internal-state-independent trapping of our atoms we utilize a crossed optical dipole trap, see [141] and references therein. This is different from the previously reported apparatus [132] which used a hybrid state-dependent single optical dipole beam + quadrupole magnetic field trap (during my tenure as

---

[2]The optical schematics in this Chapter are based on Alexander Franzen's Component Library,14 which is licensed under the Creative Commons Attribution-Non Commercial 3.0 Unported License.15.
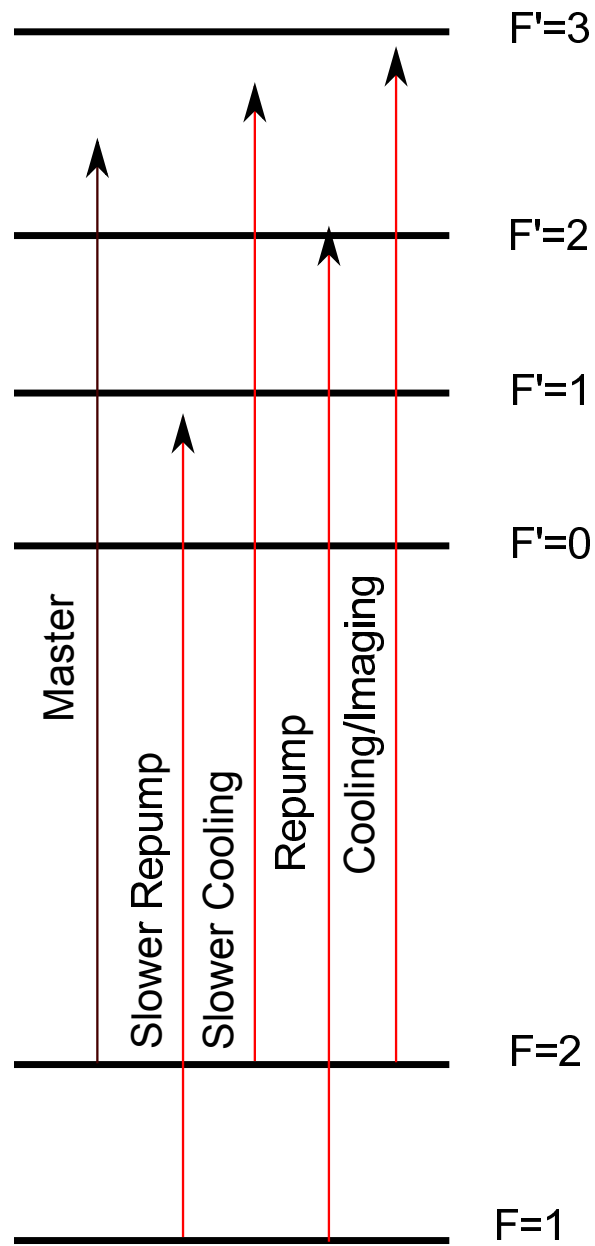
Figure 4.15: Cooling Laser Level Diagram

Cooling Laser

Fiber PM

Fiber SM

HDD Shutter

AOM

HWP

TA PRO

PBS

Repump Laser

DL 100

Master Laser

Rb cell

Pump

Vortex

Probe
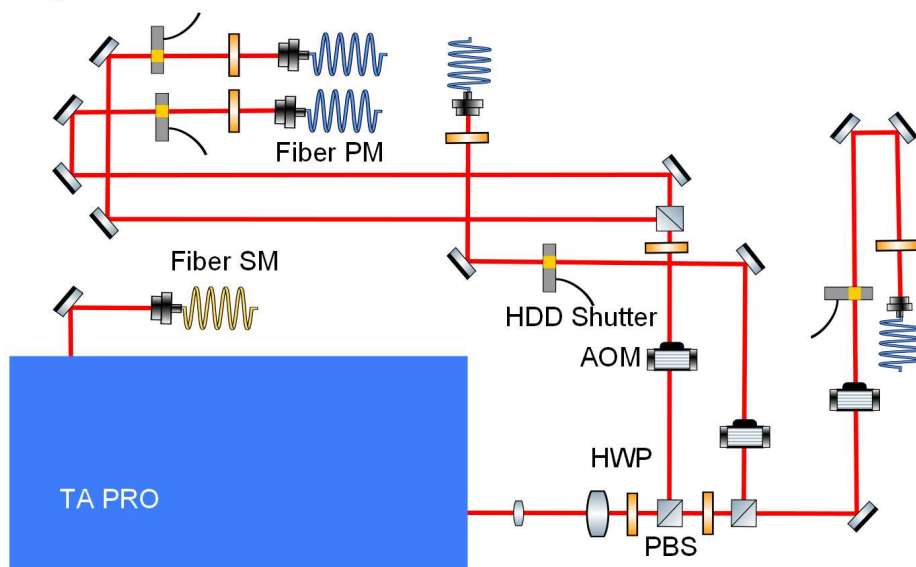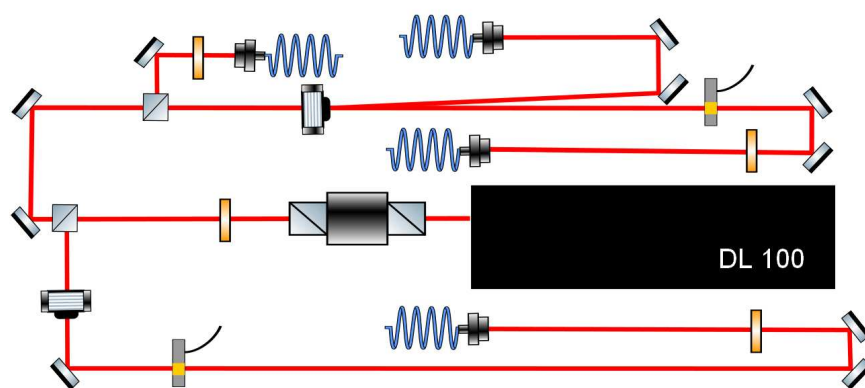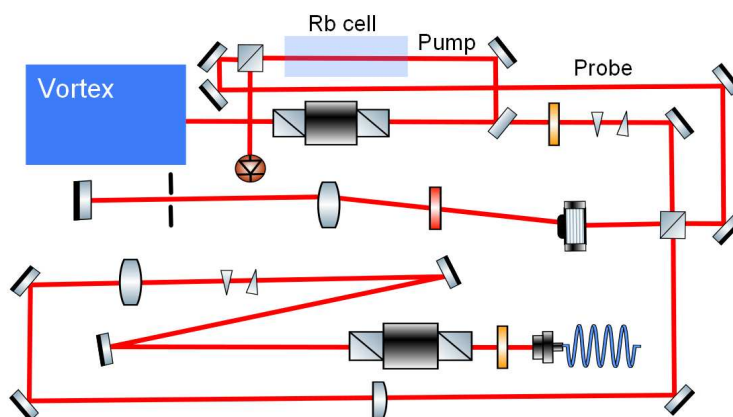
Figure 4.16: The optical layouts for the cooling lasers.

85
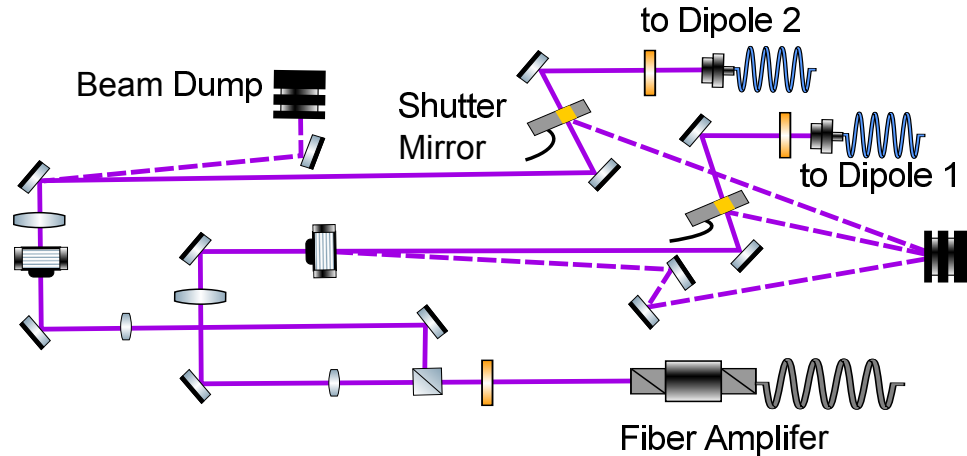
Figure 4.17: Optical layout of the dipole trapping laser; light coming from the optically isolated fiber amplifier is split between two beam paths using a half-wave plate and PBS. The dipole intensity servo is implemented via feedback to AOM RF power and the intensity locked beams are sent to the experiment via hollow core optical fiber. Due to the high power of the beams, the shutters actuate high reflectivity mirrors to steer the unwanted beams into heat sunk beam dumps.

a graduate student, we have achieved BEC in four different dipole beam configurations including: 1550 nm single beam, 1064 nm single beam, 1064 nm crossed with 1 elliptical and one circular beam, and our final configuration). We use a fiber laser system that is intensity-stabilized by acousto-optical modulators and mechanically shuttered with moving mirrors to provide the necessary optical dipole trapping power to the experiment. The free space optical layout is pictured in Fig. 4.17. Our fiber laser seed is from Orbits Lightwave producing 75 mW of linearly polarized 1064 nm light. This laser has a self calibrating PID, to optimize its current-temperature setpoint, which can produce 1-10 Hz power fluctuations for approximately the first hour of operation. We have operated it without power cycling for ≈3 years. I wrote a labview interface for serial over USB communication with the unit to check diag-

nostic information.The seed laser has enough power to simultaneously run two fiber amplifiers, a Nufern brand amplifier producing 50 W requiring 50 mW input optical power and an IPG brand amplifier producing 30W from $\approx$9 mW input power. The Nufern amplifier requires water cooling and is interlocked to the cooling water supply. Additionally, both lasers are interlocked to the door and pneumatic MOT mirrors for eye safety. Hollow core optical fibers (PN) deliver the beams to the experimental optical table and decouple trap and supply alignment issues.The beam waists at the atoms are approximately; 30 μm by 80 μm in Dipole 1 and 70 μm by 275 μm in Dipole 2. In the typical configuration for BEC, the trap frequencies are: 10Hz (along tightly confining Dipole 1 dominated by Dipole 2), 50Hz (along Dipole 2), and 130Hz (vertically).

4.6.3   Lattice laser

We generate the optical lattice light using Coherent MBR (Monolithic Block Resonator) 110 titanium sapphire(Ti:saph) laser pumped by a Coherent Verdi V-10. Details of the lattice will be discussed in the following chapter, here we simply note the general layout and technical issues. We use a Ti:saph for its wavelength tuneability, necessary for optimizing the vector light shift. Additionally, its relatively high power ($\geq$1 W) and narrow bandwidth (100 kHz to $\approx$1 kHz depending on locking configuration) allow us to generate deep three dimensional lattices, consisting of an in-plane 2D and vertical lattice, for Rubidium. The supply side optics layout is shown in figure 4.19. We have had one noteworthy technical issue with our Verdi

+ MBR system, an *internal* spot on the Verdi output window changed the spatial mode of the pump enough to make the MBR lase unreliably. This problem is one of the few "user serviceable" failure modes of a Verdi. It can be fixed by removing the Verdi cover, removing the sealed shutter housing, and cleaning the inside of the window with methanol or acetone as necessary.

The lifetime of atoms in an optical lattice should be limited by single particle spontaneous scattering of off-resonant lattice light, however, there are many technical factors that must be overcome in order to reach this noise floor. An important diagnostic is to look for frequency "noise" sidebands on the light. This could come from many sources including acoustic motion of optics but, in practice we observe noise primarily from the thin etalon used to lock the Ti:saph, as well as, the intensity stabilization lock. Figure 4.18 shows a typical power spectrum of the lattice light after the intensity lock. There are clear noise peaks at the fundamental and harmonics of the thin etalon drive frequency, as well as, a small peak from the intensity stabilization circuit. These technical noise sidebands manifest themselves as resonant heating/atom loss at specific lattice depths when the frequency of the noise sideband matches a band of the lattice. The intensity lock PID gain settings are tuned to remove the excess sideband. Initially, we increased the MBR resonant drive frequency to allow us to work at deeper lattice depths without heating. However, the final solution was to unplug the $\approx$90 kHz frequency drive and operate the MBR without a frequency lock. This came at the price of operational stability, as the MBR could now go multimode.
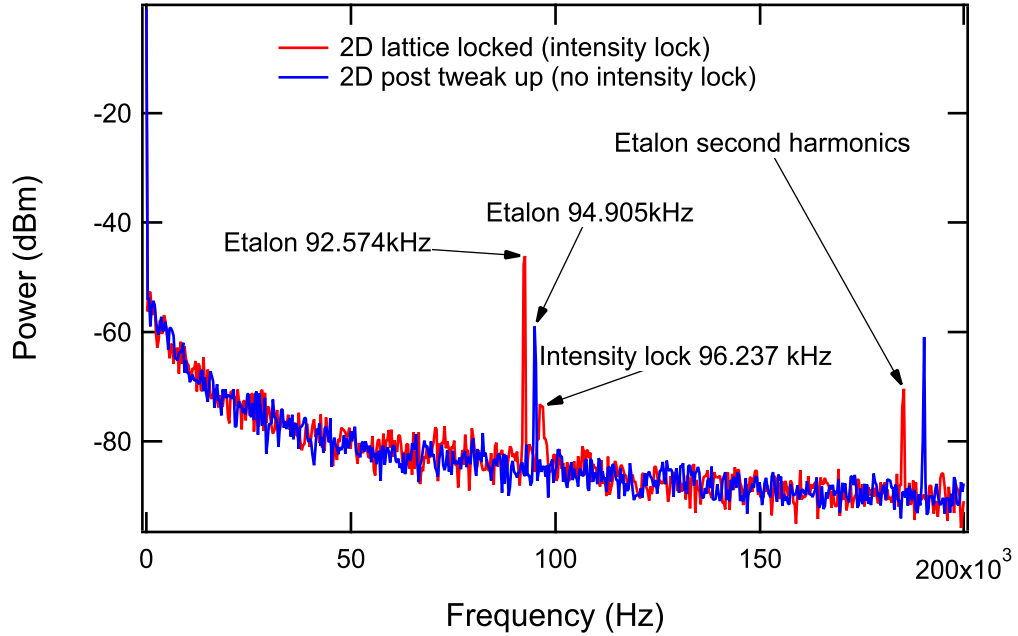
Figure 4.18: Power spectrum of noise in the output light of the Ti:Saph

4.7 Computer control

Our experiment is controlled by a main computer running our "setlist" user interface built on Labview 2012 64 bit (formerly 32 bit with the Luaview scripting language). The "setlist" user interface takes experimental line-level timing and output requests and converts them into hardware level commands which are then parsed and sent to the appropriate hardware. Setlist generates TTL pulse sequences for a master timing device, whose digital output is used to trigger outputs from other programmed devices during an experimental run. In order to make a triggerable device compatible with setlist, one must provide: 1) a software driver that takes the line commands from the user interface and turns them into list of triggers from a
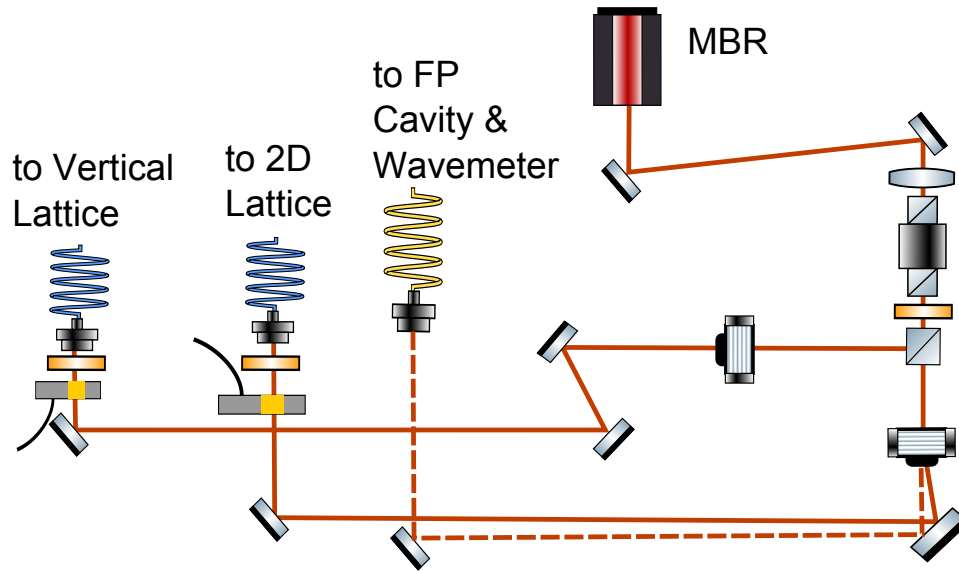
Figure 4.19: Optical layout of the lattice laser dipole trap: upon exiting the MBR the lattice light passes through an optical isolator and is variably split on a PBS using a waveplate. The two emerging beams then pass though AOM's where the opposite $\pm$ first orders are taken so that the vertical and horizontal lattices are separated in frequency by ≈ 160MHz which prevents them from interfering. The beams then pass through hard disk drive shutters and are then fiber coupled over to the main experiment optical table. The lattice light is monitored on a Fabry Perot(FP) cavity,and a wavemeter.

master TTL line and a set of outputs to occur at each trigger, e.g. as a step-through FIFO, and 2) a device programmer to communicate with the device. Running an experiment in setlist corresponds to parsing the commands into device output and pulse tables, programming the devices, and starting the master timing device. Setlist also publishes information, such as the values of the variables that are being used, to a networked Labview variable that can be accessed remotely.

Our master device is a Pulse Blaster USB (Programmable TTL Pulse Generator/Digital Word Generator and Timing Engine) which has 24 digital output lines (TTL levels) with programmable timing for every output line (minimum 50 ns pulses and 10 ns resolution). The pulse blaster "wait for event" function enables AC line triggering so that the entire experiment can be synchronized to 60 Hz magnetic fields.

We use several different slave device types in our experiment: NI USB Multifunction DAQ's (for analog control of current, cooling laser intensity and frequency) and custom-built FPGA-controlled DDS boards (for RF and microwave pulse/sweep generation and laser intensity locking). The 3 National Instruments 6363 USB Multifunction DAQ's are electrically isolated from the main control computer using optical USB extenders (Icron USB ranger 2224). The NI 6363's main relevant specifications are, 48 Digital I/O Channels (5 V TTL, 1 MHz clock rate), and 4 AO Channels (16 bits, -10 V to 10 V, 3 MS/s update rate). For additional analog I/O lines we also use a NI 6733 (16 bit, 8 channels) and 6713 (12 bit, 8 channels) PCI cards. Additionally, we use a home-built combination FPGA+DDS to generate RF signals for atomic manipulation, as well as, to drive AOM's. The design, adapted

from the Monroe group, uses an FPGA (Altera Cyclone II) to trigger and input parameters into a DDS (AD9954 DDS IC). The FPGA also functions as a PID for AOM based intensity locking. The key DDS specifications are; frequency range 0-200 MHz (as configured), $\approx$0.1 Hz frequency resolution, 14-bit amplitude resolution, 14-bit phase resolution, and has automated linear frequency sweeps. We found that the clock multiplier chip on the DDS daughter board must be bypassed in order to generate reliable timing signals. This requires that we distribute our own 400 MHz signal to all devices in place of a standard 10 MHz signal.

We collect our images on two CCD cameras, a PointGrey Flea 3 and, a Princeton instruments Pixis. The images are readout and stored in a second imaging computer networked to the main control computer. The networked variables are grabbed and their data stored with the images (in the HDF5 format). After storing the images, the Labview camera drivers call a command, in the software program Igor, that loads and processes the images. The images are analyzed in real time using a custom made GUI in Igor. Typical analysis done in Igor includes fitting to images of Kapitza-Dirac diffraction or Stren-Gerlach-separated atomic clouds and computing the relative populations.

4.8   Microwave and RF system

4.8.1   Microwave system

The collisional stability of ^{87}Rb combined with state independent optical dipole trapping allows us to occupy all eight possible F=1 and F=2 ground states. Due to

the initial magnetic trapping, the BEC is typically produced in the $|F, m_f\rangle = |1, -1\rangle$ state. Microwaves around 6.8GHz allow the upper F=2 Zeeman states to be deterministically populated. We generate the necessary 6.8GHz microwaves (with below Hz level accuracy) by frequency doubling the output of a Rhode and Schwartz frequency synthesizer (SMT 06) operating at a fixed frequency of 3.438 GHz, which is then mixed with a variable $\approx$40MHz RF signal generated from an FPGA controlled DDS device. This microwave signal is then sent through a TTL controlled switch, amplified, impedance matched using stub tuners, and sent to the experiment using a homemade microwave horn. The horn is made of a copper pipe closed at one end except for a hole in back with a radius chosen to be below cutoff for 6.8 GHz. The hole provides optical access for the MOT/imaging repumping beam. The horn has vertically and horizontally (this defines the convention used in table 4.3) placed SMA connectors to provide polarization selectivity. The detailed system is given in tables 4.2 and 4.3. The final stage of microwave amplifiers requires water cooling which is interlocked to the flow switches using a MOSFET to switch the DC power to the amplifiers. All RF and microwave sources are referenced to the same amplified 10MHz rubidium clock (SRS FS 275 & distribution amplifier SRS 735). It is important to monitor the PLL lock on the rubidium clock to verify that the frequency is stable, as on occasion have observed non-repeatable microwave transfer resulting from unlocked rubidium clock sources.

Using this microwave source, we measured a Rabi coupling strength a of $\Omega/2/(2\pi) = 17$kHz by observing the internal state evolution of an optically trapped BEC prepared in $|1, -1\rangle$ as it coherently coupled to $|2, -2\rangle$. The vertical channel has

Table 4.2: Main microwave setup

Element	Power (dBm)	Manufacturer (part number)
Source	13	Rhode and Schwartz SMT 06 3.438GHz
Isolator	11.8	Pasternack
cable	10.3	
Doubler		Marki (D-0308 LA)
Bandpass Filter	9.3	Minicircuits (VBFZ-6200-S+)
Attenuator	5.9	
Amplifier 30dB	23.8	Marki (A-0206 EZP)
Attenuator	18	
Isolator	17.7	Pasternack
Power Splitter		Minicircuits

approximately a factor of two higher microwave power than the horizontal channel. Although the steel chamber makes it difficult to maintain microwave polarization, after multiple reflections, the coupling strength to a given transition does change as a function of static bias magnetic field.

4.8.2 RF system

The RF for evaporation and internal state manipulation in the 2-25MHz range is generated using the FPGA + DDS box. The output of the FPGA+DDS is sent to an RF switch (Mini Circuits ZYSWA-2-50DR) with better than 40dB isolation, amplified (Mini Circuits ZHL-5W-1), sent to the atoms via a pair of coils pictured in Fig.4.20, then 20 dB attenuated and, 50 Ω terminated on a digital oscilloscope. The PCB coil has the advantage of being repeatably manufactured and rigidly mountable to the chamber. The RF coils were mounted between the vacuum bucket window and the quadrupole coils. To characterize the coupling strength of the $\hat{z}$
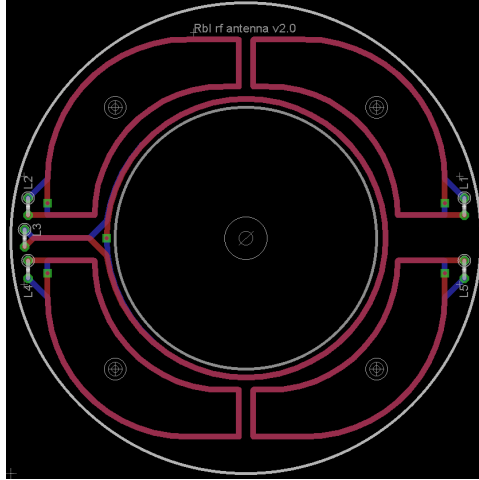
Figure 4.20: RF coil PCB.

RF field, we measured a Rabi frequency of $\Omega/2/(2\pi) = 4.76$ kHz by observing the internal state evolution of an optically trapped BEC prepared in $|1, -1\rangle$ as it coherently oscillated into $|1, 0\rangle$ and $|1, 1\rangle$ and back at a bias magnetic field where the levels were linearly Zeeman split by ≈ 2.25 MHz. At the beginning of evaporation, ≈ 20MHz, the reflection from the coils is approximately a factor of ten larger than at the end of evaporation, around 2 MHz.

4.9 BEC Sequence

Having introduced the hardware necessary for BEC production, we outline the typical sequence of BEC production in table 4.4. The sequence is very similar to a number of other labs producing ^{87}Rb condensates [132]. We load the six beam MOT from the Zeeman slowed atomic beam to collect a sufficient number of atoms ($\approx 10^9$). We then spatially compress the MOT by increasing the quadrupole field

gradient and then initiate optical molasses by turning off the quadrupole field while linearly increasing the cooling beam detuning to $\approx 10\Gamma$. After polarization gradient cooling, we shutter the repumping beam and allow atoms to accumulate in $F = 1$ in preparation for magnetic trapping. To load the magnetic trap, we switch the quadrupole field back onto its full value (> 10x the MOT field) in 1 ms. We then perform forced RF evaporation in the magnetic trap by ramping a DDS frequency in 3 steps with the crossed dipole beams at their full value. After evaporation, the atoms are loaded into the crossed dipole beams (located below the quadrupole field zero position) by adiabatically ramping the amplitude of the quadrupole field to zero. Finally, the dipole beams are exponentially ramped down to produce a BEC with no visible thermal component. The atoms are typically held in the trap for an additional half second before synchronizing the subsequent experiment to the 60 Hz power grid.

Table 4.3: Vertical and Horizontal microwave channels

	Vertical antenna		Horizontal antenna
Element	Manufacturer (part number)	Element	Manufacturer (part number)
Mixer	Marki (IRW0618 LXW-2) mixes in signal from "DDSuW2" $\approx$ 40MHz	Mixer	Marki (IRW0618 LXW-2) mixes in signal from "UCF-PGA7" $\approx$ 40MHz
Bandpass filter	5.6-7GHz	Bandpass filter	5.6-7GHz
TTL switch	Pulsar (PMC SW1AD-15)	TTL switch	Pulsar (PMC SW1AD-15)
Amplifier	Microwave Power L0607-35	Attenuator	-6dB
Isolator	Pasternack (PE 8302)	Amplifier	Microwave Solutions (MSH-5727901)
Directional coupler	Pasternack (PE 8302) reflected power to 50Ω	Isolator	Pasternack (PE 8302)
Directional coupler	Pasternack (PE 8302) reflected power 20 dB attenuated to power meter Minicircuits (ZX47-40-St)	Directional coupler	Pasternack (PE 8302) reflected power to power meter Minicircuits (ZX47-40-St)
Stub tuner		Directional coupler	Pasternack (PE 8302) reflected power 20 dB attenuated to power meter Minicircuits (ZX47-40-St)
Antenna (V)	in horn	Stub tuner	
		Antenna (H)	in horn

Table 4.4: BEC sequence

Step	time(s)
load MOT	3-5
compressed MOT	0.01
optical molasses	0.01
optical pumping	0.002
Magnetic trap + RF evaporation (22-18.5 MHz)	0.7
Magnetic trap + X dipole trap + RF evaporation (18.5-8-2 MHz)	2.0,2.3
Adiabatic decompression of Magnetic trap with X dipole trap (I_{quad}=155-115-38)	0.5,1.0,0.25
X dipole trap evaporation	2.0
X dipole trap hold + line trigger	0.5

Chapter 5: Manybody physics in optical lattices

5.1 Introduction

Optical lattices have long been a part of atomic physics [142, 143]. Standing wave intensity patterns are central to the explanation of subDoppler cooling processes and even before BEC (or before the mass production of BEC), they served as an important tool to create defect-free crystals of light with atomic motion quantized in bands analogous to electrons in solids. Even today, a profitable line of research can be made by extending experiments with laser cooled atoms and optical lattices into the ultracold regime [144]. High phase space density atomic samples in optical lattices have transcended their single particle origins and now enable experiments where the effective system dimensionality and interactions are important and can be tuned. This has led to the current program of "quantum simulation" [145] where experiments that are well controlled at the single particle level can be operated in an interacting regime where the Hilbert space becomes intractably large on classical computers.

While BEC may be understood at its simplest level as a non-interacting statistical effect, optical lattices allow one to effectively control the energy of atom-atom interactions relative to their kinetic energy. A remarkable example of this is the

superfluid-to-Mott insulator quantum phase transition, where, as the interaction between atoms is increased, the qualitative nature of the ground state wave function changes from weakly interacting superfluid to strongly correlated insulator. This process happens theoretically at zero temperature in the absence of environmental coupling. Realized experimentally in [146], this was a paradigmatic demonstration of a interaction driven quantum phase transition using ultra-cold atoms in an optical lattice. Such quantum phase transitions have been previously observed in a traditional condensed matter context [147, 148] but, it is hoped that the methods of atomic physics may enable further unprecedented observation and control of many-body states.

The realization of the Hubbard model in optical lattices naturally inspires us to push to ever lower energy scales in pursuit of more exotic physics. The low energy behavior of the Hubbard model can be mapped onto the Heisenberg model describing quantum magnetism. A canonical example of this is the rich phase diagram of the cuprates, where the doping of antiferromagnetic magnetic insulators leads to the emergence of high-T_c superconductivity. The realization of such physics in optical lattices is profoundly difficult because the magnetic spin-spin interactions in the Heisenberg model are mediated by second order "superexchange" processes in the parent Hubbard model. This means that in traditional simple cubic lattices the superexchange energy (describing the tunneling of an atom to a neighboring lattice site, interaction on site, and return tunneling) must always be small compared to the tunneling energy. There has been progress toward cooling [149] and observation of antiferromagnetic order in extended lattices [150]. However, an alternative route to

100

observation of superexchange is the use of lattices with two sites per unit cell [151–153]. In this case, the lattice can be used to control an additional band structure energy scale as in "superlattice" semiconductor heterostructures [154], as well as to isolate pairs of atoms generating a massive reduction in effective system Hilbert space.

A second theme of our research in ultracold atoms in optical lattices is the exploration of manybody dynamics in regimes where dissipation limits traditional condensed matter experiments [155–157]. In this context, dynamic multi-period lattice control [158–161] enables the preparation and manipulation of manybody excited states. At a few particle level, this control enables basic quantum computation operations such as the $\sqrt{SWAP}$ enabled by the exchange interaction of two particles merged onto the same site [162]. Of particular interest is the adiabatic preparation of excited spin states [163, 164]. In the absence of lattice mediated coupling to the environment, the high energy spin system would only be able to relax its energy via high order tunneling processes that would connect the bulk of the system to impurities on the edges. Another inspiration of our work is the investigation of the paradigm of critical slow down [165, 166] where system relaxation time scales diverge for weakly interacting systems near a critical point. There has recently been numerical evidence that strongly interacting systems in certain contexts critically speed up [167]. It is hoped that ultracold atomic systems could be a useful platform to controllably tune these interactions and observe the ensuing dynamics.

5.2 Optical lattices

5.2.1 Single atom lattice physics

An optical lattice is a standing wave interference pattern created by the electric fields from a laser. The simplest case is a linearly polarized beam reflected back on itself. The field maxima will add creating an intensity pattern with half the spatial period of the electric field ($\lambda/2$ spaced). In the context of condensed matter quantum simulation, we will work in a regime where the frequency of the lattice light is far from atomic resonance. Far from resonance light scattering is suppressed and we may think of the optical lattice as a conservative potential for atomic motion. The full potential the atoms experience is [168],

$$V = -\vec{E}^* \cdot \hat{\alpha} \cdot \vec{E} - \mu \cdot \vec{B} \tag{5.1}$$

where $\hat{\alpha}$ is the atomic polarizability tensor, $\vec{E}$ is the electric field of the lattice laser, μ is the magnetic dipole moment, and $\vec{B}$ is a static magnetic field. The operator $\hat{\alpha}$ has scalar, vector, and tensor components. Typically only the scalar part is considered in the limit that the lattice light is far detuned with respect the fine and hyperfine structure splitting. However we utilize a lattice detuning on the order of the fine structure splitting so both the vector, ($\propto \vec{B}_{eff} \cdot \vec{F}$ where $\vec{B}_{eff} \propto \vec{E}^* \times \vec{E}$), and scalar, ($\propto |\vec{E}|^2$), parts of the dipole interaction are relevant while the second rank part is suppressed. By the projection theorem, the vector lightshift must behave in

a manner similar to real magnetic field applying a m_f dependent shift. The vector light shift is different from its real counter part in that the effective field now can change direction on the scale of an optical wavelength and that it only interacts via the Bohr magneton and not also via the nuclear magneton (typically this is a small effect).

Once our state-dependent periodic optical potential is established by beam geometry, polarization, and detuning, we may find the single-particle Bloch function eigenstates and energies. In the case of a one dimensional lattice with a single spatial frequency, the Schrodinger equation may be solved analytically in terms of Mathieu functions. These band solutions smoothly interpolate from free particle plane waves in the low lattice limit to an array of uncoupled harmonic oscillators in the deep lattice limit. With lattices that have multiple spatial frequencies in higher dimensions it is often more useful to represent the lattice Hamiltonian in a plane wave basis and retain only the necessary terms to achieve a given accuracy for an observable, say the band energy at a given quasi momentum. Although the plane wave basis is often the natural choice because it exploits the underlying translational symmetry of the potential, it is useful, in the context of contact interactions, to consider a spatially localized basis of Wannier functions. The Wannier function of a given band can be constructed by Fourier transforming the Bloch functions over the domain of the given Brillouin zone. This cut off in momentum space implies that the real space Wannier functions cannot be infinitely well localized. This Fourier transform definition of Wannier functions also leaves a phase ambiguity on the wavefunction and in general requires care to create maximally localized states, see [169]

103

for a review.

5.2.2 Lattice enabled models of manybody physics

5.2.2.1 The Hubbard model and Mott insulator

The Hubbard Model was originally introduced as a minimal theoretical model to include the effects of electron-electron interactions on the conduction in solids [170]. Its most essential features are a term that describes particle motion (typically a single band tight binding model) and a term that describes density-density interactions. The Hubbard model was extended to bosons in [171], the Bose-glass phase was explored in [172], and its realization in optical lattices was proposed in [173].

$$H = \sum_{<i,j>,\sigma} J_\sigma(\hat{a}_{j,\sigma}^\dagger \hat{a}_{i,\sigma} + h.c.) + \sum_{i,\sigma} \frac{U_\sigma}{2}(\hat{n}_{i,\sigma}(\hat{n}_{i,\sigma} - 1))$$
$$+ \sum_{i,\sigma,\sigma'} U_{\sigma,\sigma'}\hat{n}_{i,\sigma}(\hat{n}_{i,\sigma'}) + \sum_{i,\sigma} \epsilon(i)\hat{n}_{i,\sigma} \tag{5.2}$$

where $\hat{a}_{j,\sigma}(\hat{n}_{j,\sigma})$ is the destruction(number) operator of a particle of spin σ on site j. The top line constitutes the two essential terms, tunneling and interaction. Spin dependent contact interactions are parametrized by $U_{\sigma,\sigma'}$ (for the $F = 1, 2$ hyperfine states of ^{87}Rb $U_{\uparrow,\downarrow} \approx U_{\uparrow,\uparrow} = U_{\downarrow,\downarrow}$). The onsite energy $\epsilon(i)$ can be used to describe a external trapping potential or simply to tune the onsite occupation.

The model is quartic in field operators and cannot be exactly solved analytically, though a basic intuitive picture can be made by considering two limits. When

J $\ll$ U the wave function localizes on lattice sites and the compressibility vanishes. The real space occupation basis is ideal and the kinetic energy terms can be treated perturbatively. This is the Mott insulator state [174, 175] (proposed to explain the extremely low conductivity observed in NiO). It is special because two particle interactions drive the qualitative change in behavior as opposed to a standard "band" insulator where the chemical potential lies within the band gap which is effectively a single particle/statistical effect. Well into the Mott Insulating phase, the excitation spectrum of this state is gapped, as particles must have approximately the onsite interaction energy U to conduct. In the opposite limit, J $\gg$ U, the diagonal basis is plane wave eigenstates. In this case, interactions can be treated perturbatively and the ground state is superfluid. The superfluid excitation spectrum is not gapped because an extended system can support infinitely long wavelength excitations. It should be noted that the superfluid state may have interactions which changes the dispersion from quadratic (free particles) to linear (sound waves).

The Bose-Hubbard model mean-field phase diagram, as a function of Hamiltonian parameters, can be readily calculated as in the first section of [172]. When scaled by the coordination number the phase diagram is independent of dimension. However, assuming a two nearest neighbors per dimension the extent of the lobes grows with decreasing dimensionality (where quantum fluctuations become increasingly important). The mean-field phase diagram can be numerically improved upon at the MI-SF phase boundary where expectation of the superfluid filling is near an integer (the tips of the Mott lobes). Corrected phase diagrams have been calculated with more advanced numerical methods [176, 177].

The tunneling parameters are defined in terms of overlap integrals of Wannier functions on site j with spin σ, $w_\sigma(x - x_j)$, as,

$$J_\sigma = \int dx \; w_\sigma(x - x_i)(-\frac{\hbar^2 \nabla^2}{2m} + V_{latt}(x))w_\sigma(x - x_j). \tag{5.3}$$

The density-density interaction energy, U, is the overlap of two Bosons in the same state,

$$U_\sigma = \int dx \; g|w_\sigma(x - x_i)|^4 \tag{5.4}$$

where $g = 4\pi\hbar^2 a_s/m$. The realization of Hubbard physics requires the temperature of the system to be small compared to the Mott melting temperature. A generally accepted value for the melting temperature is $k_B T \leq 0.2U$ [178].

5.2.2.2 The Heisenberg model

The Heisenberg model is a canonical quantum interacting spin model and it is a useful model for studying magnetic phase transitions [179]. In the Heisenberg model a given lattice site may contain a spin-1/2 particle which may be oriented in 3D (in place of an up or down classical spin found in an Ising model). In a fixed lattice with no motional degrees of freedom, the spins on different sites interact with coupling strength or J_{ex} [1]. The Heisenberg model may be considered the low-energy effective description of the Hubbard model valid at unit filling of Bosons (half filling for Fermions) for $J/U \ll 1$. The key idea is that when the particles are

---

[1]The dynamics of ultracold atoms creates a notional conundrum because t is frequently used for time not tunnel coupling, and the tunnel coupling becomes J, leaving no conventionally accepted notation for the magnetic exchange coupling.

nearly immobile, a restricted set of the full Hubbard model Hilbert space maybe

considered and the energetics within this restricted Hilbert space is the same as

that of a nearest neighbor Heisenberg model with magnetic coupling $J_{ex} = 4J^2/U$

(physically, the "exchange" of two neighboring spins occurs as a second-order virtual

tunneling process through an intermediate doubly-occupied state). An application

of this transformation to ultracold atoms in optical lattices was given in [180]. In

order to make tunable spin-spin interactions, as well as to make the onsite Hilbert

space for Bosons spin-1/2 (or larger) a state dependent optical lattice was a key

ingredient for this proposal. The so called XXZ model is an important special case,

$$H_{XXZ} = J_{ex} \sum_j (\hat{S}_j^x \hat{S}_{j+1}^x + \hat{S}_j^y \hat{S}_{j+1}^y + \Delta_z \hat{S}_j^z \hat{S}_{j+1}^z) \tag{5.5}$$

where the in-plane interaction energies, $J_{ex} = J_\uparrow J_\downarrow / U_{\uparrow\downarrow}$, are equal and the out-of-

plane interaction energy, $J_{ex}\Delta_z = (J_\uparrow^2 + J_\downarrow^2)/(2U_{\uparrow\downarrow}) - J_\uparrow^2/U_{\uparrow\uparrow} - J_\downarrow^2/U_{\downarrow\downarrow}$, can be tuned to

be different from the in-plane interaction energy. The spin operators defined in-terms

of Hubbard operators are: $\hat{S}_j^x = 1/2(\hat{a}_{j,\uparrow}^\dagger \hat{a}_{j,\downarrow} + \hat{a}_{j,\downarrow}^\dagger \hat{a}_{j,\uparrow})$, $\hat{S}_j^y = -i/2(\hat{a}_{j,\uparrow}^\dagger \hat{a}_{j,\downarrow} - \hat{a}_{j,\downarrow}^\dagger \hat{a}_{j,\uparrow})$,

and $\hat{S}_j^z = 1/2(\hat{n}_{j,\uparrow} - \hat{n}_{j,\downarrow})$. The ground state phases are controlled by Δ_z, and there

is a phase transition at $\Delta_z = 1$. For $|\Delta_z| < 1$ the excitations are gapless spin

waves but for $\Delta_z > 1$ the excitations are gapped and the ground state is an Ising

ordered antiferromagnet. The realization of ground state quantum phases in this

model requires that $k_B T \lesssim J^2/U$ which is in the 100 pK range. In addition to this

stringent temperature requirement, the parasitic heating rate of the lattice must also

be small compared to the J^2/U scale in order for long range magnetic correlations

to form. This is particularly limiting for Alkali fermions because their fine structure splitting, of order the spin-dependent lattice detuning, produces an unacceptably large scattering rate. In the final chapter of this thesis we will consider a Heisenberg model with an additional tunable lattice energy scale which relaxes these conditions and enables the observation of dynamics.

5.3   Probes of many particle states

The momentum distribution of the 3D SF-MI transition was first observed via TOF and absorption imaging in [125]. For low lattice depths, the population in the diffracted orders increases with increasing lattice depths. When the lattice depth at the center of the cloud crosses the phase transition from superfluid to insulating, the diffraction signal from the superfluid gains an additional broad incoherent part (as there is no well-defined phase from insulating site to insulating site). As the size of the central Mott state grows with increasing lattice depth, the incoherent background becomes the dominant feature. Due to this inhomogeneity and the finite size of the system, the sharp quantum phase transition from SF to MI is broadened into a slower cross-over.

The excitation spectrum of MI state was further probed by using a transport like measurement, where a magnetic field gradient to "tilt" the lattice such that ground motional state of one lattice site was energetically separated from the motional ground state of the neighboring site [125]. When the tilt energy equals the onsite interaction energy, resonant tunneling may occur since the system no longer

needs to pay the U energy cost to create a double occupancy. This tunneling in the presence of a field gradient at deep lattice depth, partially dephases the super-fluid wavefunction created when the lattice is ramped back down. This results in broadened superfluid diffraction peaks. Monitoring the diffraction peak width as a function of applied magnetic field gradient reveals resonant peaks at energies of U and 2U. The peak at 2U is further broadened due to competing degenerate processes eg. the creation of two doublon-hole pairs is degenerate with the co-tunneling of two atoms or tunneling from a doubly to singly occupied sites. This spectroscopy also allows one to measure U as a function of lattice depth. An alternate transport measurement enabled by moving the magnetic trap containing the BEC relative to the lattice beams was implemented in [181]. Such a measurement is not a direct probe of the manybody spectrum but does give insight into the properties of the the ground state quantum phase.

Since the observation of the superfluid-insulator transition, a number of al-ternative spectroscopic techniques have been implemented to gain further insight to the manybody spectrum. Bragg spectroscopy has been used to probe both the BEC dispersion curve [182,183] and the Mott insulator spectrum [184] (a proposed variation on this is lattice phase modulation [185]). A technique complementary to the observation of momentum space diffraction peaks is to use a matter wave anal-ogy of the Hanbury-Brown Twiss effect. While the momentum spectrum of a Mott insulator is broad and unpeaked, its noise correlations reveal sharp peaks associated with real space order of atoms in the lattice [186]. Another technique unavailable in condensed matter due to a lack of electron internal structure is interaction shift

resolving microwave spectroscopy of an internal state [187](this technique will be implemented and further discussed in the following chapter). Finally, single lattice site resolving optical microscopes are enabling the study of quantum gases on the single atom level [103, 188]. In the following we develop and demonstrate direct probes of staggered magnetization.

Chapter 6:   State-dependent Dynamic Optical Checkerboard Lattice

6.1   Idealized double well lattice

Before describing the checkerboard lattice in detail, I will review the simplest idealized version of our single-beam retro-reflected lattice originally reported in [189]. While much of the basic physical intuition about this lattice has been described in this initial publication, substantial subsequent advances have occurred, including but not limited to sublattice addressing [190] and precision measurement of sublattice energetic offset via phase running in the Mott insulator regime [191]. The goal of this chapter is to tie together and perfect these techniques in order to enable the use of this lattice as a tool for manybody physics.

The optical layout of the lattice is shown in fig 6.1. The lattice is a 4-beam 2D lattice contained in the $\hat{x} - \hat{y}$ plane, generated by folding a single beam back on itself. The initial input beam is linearly polarized in the 2D plane of the lattice. It passes through a Pockels cell/electro optic modulator (PC1 or the input Pockels cell) oriented with the extraordinary axis rotated 45° out of the plane, which allows the polarization to be continuously transformed from horizontal linear through elliptical to circular and elliptical back to vertical linear. The voltage dependent retardence of PC1 is parameterized by $\theta(V)$. The lattice in the horizontally and vertically
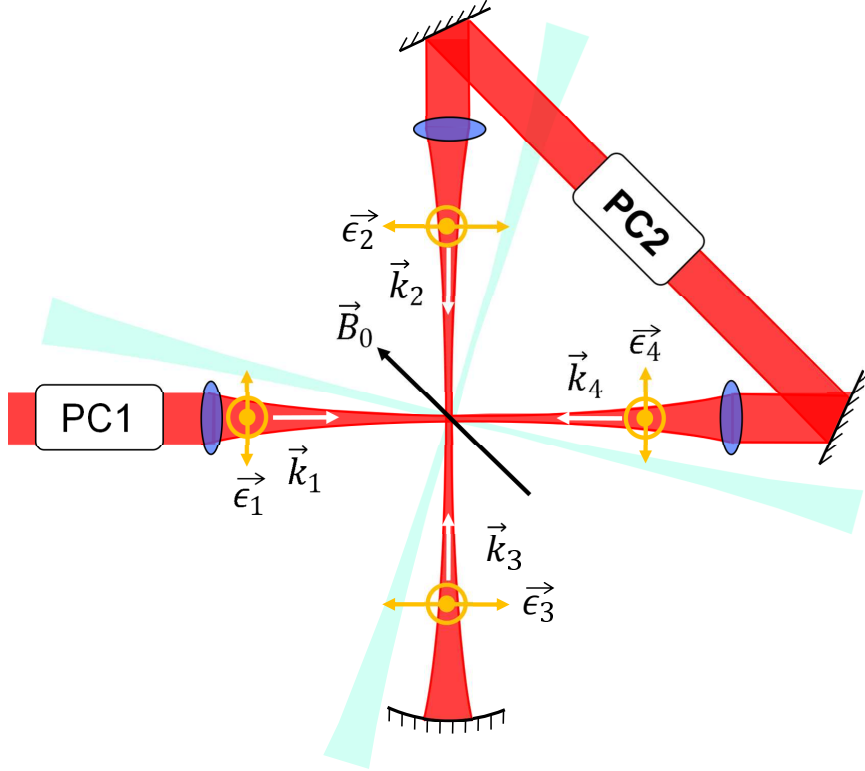
Figure 6.1: Double Well Optical Lattice layout: lattice beams are in red, dipole beams are in light blue, wave vectors are in white, and polarization vectors are in yellow).

polarized limits will form conceptual building blocks of our lattice intuition in terms of $\lambda/2$ and λ spaced lattices, formed by either a pair of independent 2-beam lattices or full 4-beam interference. The input beam, with wavevector $\vec{k_1}$ and polarization $\vec{\epsilon_1}$, is focused down onto the atomic cloud. The beam is then collimated and passes through a second Pockels cell (PC2) with its extraordinary axis in the horizontal 2D plane, allowing us to control the relative phase, $\beta(V)$, between the in-plane and the out-of-plane polarization components, resulting in polarization $\vec{\epsilon_2}$. The beam with wavevector $\vec{k_2}$, encounters the atoms a second time orthogonal to $\vec{k_1}$ after being focused back down. The beam is then reflected off of a curved mirror

which refocuses the light as it propagates back forming $\vec{k_3} = -\vec{k_2}$. The "$\vec{k_4}$" beam propagates through PC2 again and then back opposite to $\vec{k_1}$.

This single beam retro-reflected lattice is inherently phase stable. This means that phase noise due to translation of the mirrors forming the lattice will lead only to a translation of the lattice intensity pattern and not to change in shape/topology of the lattice. If this motion is slow enough, the atoms will adiabatically follow and heating will not occur. It is generally true that when a D dimensional lattice is formed using ≤D+1 beams [192] it is phase stable. The intuition for this is simple, D+1 beams will have D relative independent phases. Each of these phases can be be associated with translation in one dimension. Lattices created using more than D+1 independent beams must have their "time phase" actively stabilized [193]. Despite the violation of this inequality, (we make a 2D lattice using 4 beams) the retro reflected nature of the lattice removes the extra degree of freedom ensuring phase stability [194]. Another way to view this argument is to realize that you never can independently align $\vec{k_4}$. We have three independent wavevectors to align, exactly in agreement with the inequality.

In the following, we consider the lattices formed by different polarization configurations of the single retro reflected beam. With the polarization horizontal in the plane of the page and with $\vec{k_1} \cdot \vec{k_2} = 0$, the light polarization vectors $\vec{\epsilon_1}$ and $\vec{\epsilon_2}$ are orthogonal. Thus only $\vec{k_1}$-$\vec{k_4}$ and $\vec{k_2}$-$\vec{k_3}$ can interfere. These two sets of 2-beam interferences give a typical two dimensional $\lambda/2$ spaced lattice. However, the input Pockels cell can be set to the half wave voltage, giving vertical, out-of-plane linearly polarized light. In this case, all four beams can interfere giving a $\lambda/\sqrt{2}$ spaced lattice

rotated 45° with respect to the $\lambda/2$ spaced lattice. Along the lattice direction of the $\lambda/2$ spaced lattice, the spacing is λ, hence we will call it the "λ lattice" configuration. Any intermediate input Pockels cell rotation results in a combination of both $\lambda/2$ and λ lattices giving a 2D array of double wells which, in general, do not have equal depths.The qualitative picture is of two independent lattices with a relative amplitude controlled by PC1 and with relative phase (offset position) controlled by PC2.

Figure 6.2 shows the action of PC1 as it changes the polarization from vertical linear through elliptical down to horizontal linear with the phase of PC2 chosen to be in between $\lambda/2$ lattice sites. PC1 smoothly connects the "typical" $\lambda/2$ lattice shown on the right to the four times deeper λ lattice shown on the left. This lattice deformation allows us to split atomic wave packets localized on a single lattice site, realizing a matter wave version of double slit interference. The Pockels cells can be switched (apply ≈ 1 rad phase shift) in a few μs, which is faster than the time scale associated with typical band spacings (10 μs) and considerably faster than the coherence time of double slit interference(100 μs - 1 ms). When we realize matter wave double slit interference, we are careful to split the lattice sites slower than the band gap. The phase of the lattice containing a vertical polarization component can be swept along one direction a full wave length (from $-\pi$ to π) by changing the voltage of PC2.

In addition to the scalar lattice potential discussed so far, there is, in general, a vector lattice potential giving rise to a fictitious Zeeman field. For the vector light shift to be nonzero, the light must be near detuned relative to the fine structure
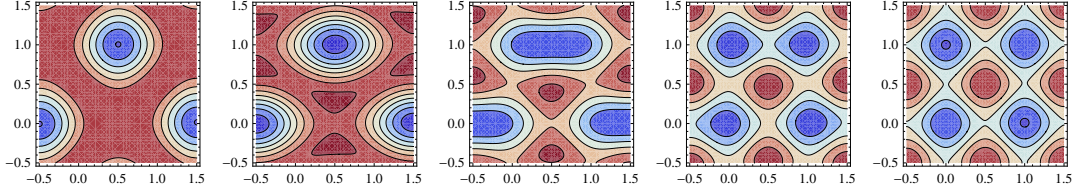
Figure 6.2: Action of the input Pockels cell: Contour plots of the scalar lattice potential as the input polarization is adjusted from vertical to horizontal. The lattice is deformed from λ spacing to $\lambda/2$ spacing. This deformation process, from λ to $\lambda/2$, leads to double slit matter wave interference as atomic wavepackets in one well are split in two then recombined in time of flight.

splitting, and the light polarization must have some ellipticity so that $\vec{B}_{eff} \propto \vec{E}^* \times \vec{E} \neq 0$. A typical vector field lies in the lattice plane, and is plotted over the scalar potential contour plot in fig. 6.3. The local field in neighboring sites is orthogonal although the relative field amplitudes may also vary dramatically. In the presence of a large bias field $\vec{B}_0 \gg \vec{B}_{\text{eff}}$, the total spin-dependent staggered offset $\delta_\sigma \propto |\vec{B}_0 + \vec{B}_{\text{eff}}|$ depends on the relative angle between $\vec{B}_0$ and $\vec{B}_{\text{eff}}$:

$$\left| \vec{B}_0 + \vec{B}_{\text{eff}}(x,y) \right| \approx \left| \vec{B}_0 \right| + \vec{B}_{\text{eff}}(x,y) \cdot \left(\frac{\vec{B}_0}{\left| \vec{B}_0 \right|} \right). \tag{6.1}$$

This local field direction allows us to define A and B sublattices. By tuning the direction of the bias magnetic field $\vec{B}_0$, we can tune the state dependence of the sublattices. If $\vec{B}_{eff}$ for one sublattice points along $\vec{B}_0$ the two fields add linearly, however, the other sublattice will now have $\vec{B}_{eff} \perp \vec{B}_0$. In this case the total field magnitude is the quadrature sum of the two which is dominated by $\vec{B}_0$ rendering the other sublattice effectively state independent.
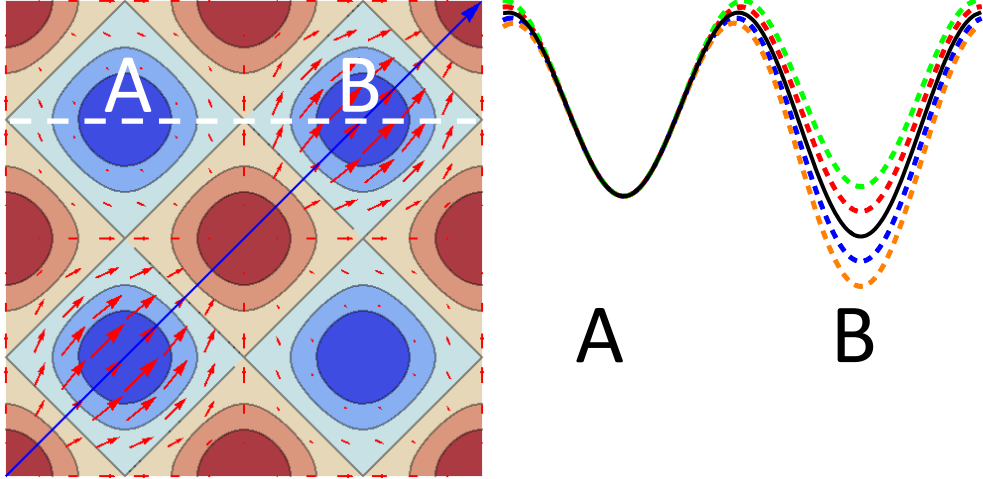
Figure 6.3: A $\lambda/2$ spaced lattice with a small offset applied. The contour plot shows the scalar potential (blue shading indicates lower potential). The red arrows indicate the local effective Zeeman field $\vec{B}_{eff}$, and the blue arrow represents the bias magnetic field $\vec{B}_0$. The right hand side is a cross section of the potential along the white dotted line. The colored dashed curves are the potentials seen by the five internal spin states of ^{87}Rb and the solid black curve is the scalar $m_f = 0$ potential. In this field configuration the, B sites have a state dependence.

6.2   Implementation

6.2.1   Imperfections in the lattice

In this section, we expand the description of the lattice to include additional degrees of freedom and their effects that must be controlled in the laboratory. While we do not have to actively stabilize an interferometer to remove time phase issues, we do rely on the passive stability and purity in polarization of our lattice light. Many of the technical challenges reported in the following are related to characterizing and controlling polarization at a sufficient level.

Following the previous section, we will enumerate the potential lattice errors in the order of light propagation through the lattice. The input polarization is ideally horizontal with respect to the table, and α_0 parametrizes the angle of the input polarization from horizontal. This is a relatively forgiving imperfection because the induced sublattice offset energy, $\Delta U = 4U_0 \sin^2(\alpha_0)$ (where U_0 is the lattice depth), scales quadratically with α_0. The next imperfection, α_1, is the misalignment of the axis of PC1 from $45°$ with respect to the plane of the lattice beams. It manifests itself as imperfections in the λ lattice preventing it from achieving perfect vertical polarization. The misalignment of the axis of the 2D Pockels cell from horizontal to the lattice plane, α_2, manifests itself as a residual moving lambda lattice when the polarization should be confined to be in the plane. In the $\lambda/2$ lattice, the most serious source of imperfection arises when the lattice beams don't intersect at $90°$. We denote the deviation from $90°$ by ϵ and the site-to-site energetic offset scales linearly for small ϵ, $\Delta U = 4U_0 \sin(\epsilon)$. Characterization of this offset is discussed in section 6.3.2. Additionally, attenuation through windows leads to reduced lattice depth upon retroreflection. The imperfect beam-power-balance has been dramatically reduced with AR coated optics and viewports in the new apparatus, to the percent level from the 10 percent level with the old cell. Finally, to insure the correct state dependence, the bias magnetic field direction must be oriented in the lattice plane and along the local effective Zeeman field of the lattice using techniques in 6.3.2 and 6.3.3.

6.2.2 Crude lattice alignment procedure

In this section we detail the technical steps associated with the alignment and characterization of the optical components of our lattice. Once the output beam of the fiber to the experiment is collimated (translating an aspheric lens and looking at a shearing interferometer), the first step is to linearly polarize the beam in the plane of the optical table. Place a kinematically adjustable glass plate at Brewster's angle with respect to the incident beam. Then adjust the beam so that it is a fixed height above the optical table ∼1 m distance away and rotate the polarizer to minimize the transmission. We estimate the uncertainty in the angle between the polarization and the optical table to be ∼0.001 rad. The process of finding the Brewster angle and subsequent polarizer adjustment should be iterated several times until subsequent adjustment converges to the same position.

Once the beam height and input polarization are fixed, the lattice plane polarization is defined. We can make a pair of mobile crossed polarizers, one vertical and one horizontal. It is useful to mount a double Glan-Taylor calcite polarizer with a ∼4° field of view, and 1:10^5 polarization extinction ratio (6 non-AR coated surfaces inherently reduce transmission, be careful to note this when calculating extinction ratios) in a kinematic mount capable of pitch, yaw, and barrel rotation. The vertical polarization can be found by maximizing the extinction of the horizontally polarized beam then reversing the polarizer with respect to beam propagation direction and re-maximizing and repeating until the extinction is globally maximized.

Once the polarization of the input beam is set, the first pass of the lattice beam

should be aligned to the BEC with PC1 in place but not carefully optimized. The first step toward this is aligning the beam using a mechanical target on the chamber windows. To avoid additional parasitic lattices arising from reflections off of the nominally AR coated windows, the in-plane lattice beams are rotated by $\approx 3.5°$ from normal incidence to the windows. Using targets with $\approx 100\mu$m printed lines and a vacuum chamber of order 20 cm, one can achieve approximately 0.005 rad angular accuracy. If the dipole trapping beams are aligned to the same target, this is typically enough to quickly observe an effect on trapped atoms in the chamber. However, if this approach is insufficient, the next step is to tune the Ti:saph near atomic resonance (within a nanometer) and steer the lattice beam around until loss of atoms due to near resonant scattering out of the BEC or magnetically trapped thermal cloud is observed. This alignment can then be quickly improved by noting the zero time of flight BEC position and trapping atoms in the "$\vec{k}_1$" lattice beam and the dipole beam nominally orthogonal to $\vec{k}_1$ and then overlapping the "$\vec{k}_1$" trapped cloud with the crossed dipole BEC position. The beam height can be optimized by maximizing the number of trapped atoms.

The alignment of $\vec{k}_1$ onto the BEC should be checked by "dipole pulling", where the lattice beam is used as a competing dipole trap to displace the BEC from its lattice-unperturbed-position in the dipole trap. As one scans a lattice beam across the BEC from far-off on one side to far-off on the other side the position of the BEC is: first unaffected, then pulled off center toward the lattice beam, then again unaffected as the lattice beam overlaps the BEC, then pulled off to the other side with the lattice beam, and finally unaffected again when the lattice beam

is far off on the other side. This dispersive feature in BEC position vs. lattice position is colloquially referred to as the "S" curve, and being centered on it is a reliable signal for lattice position optimization. It is a difficult procedure in the sense that no displacement can mean perfectly aligned or completely misaligned without directional information.

Once the $\vec{k}_1$ beam is initially aligned on the atoms, the next step is to optimize the alignment of the input Pockels cell (Linos Pockels cell driven by a Trek 5kV amplifier). The first step is to center the beam on the input aperture and observe the so-called isogyre or Malteese cross. To do this, you must add a second vertically oriented polarizer after the PC and a diffusing object (ground glass, tissue paper or scotch tape all work, although the tape may have undesirable stress induced birefringence) before the PC. Looking on a screen after the vertical polarizer, the Malteese cross is a dark cross with the axes of the polarizers defining the axes of the cross and radially symmetric interference pattern which should change as a function of applied voltage on the PC. The goal is to center the residual transmitted beam on the axes of the cross. The next step is the fine adjustment of the beam center by minimizing transmission through crossed polarizers, with the vertically oriented polarizer located just before the photodiode. To adjust the polarization from horizontal linear to vertical linear, the extraordinary/fast axis must be oriented at 45° with respect to the table. An accurate, if potentially lethal (the HV amplifier can drive 80 mA at 5 kV) way of orienting the fast axis at 45°, is by maximizing the extrema in extinction ratio by rotating the PC while sweeping to $\pm$ the half-wave voltage in a triangle pattern (safety note, "class 0" electrical safety gloves protect

up to 5 kV). This ramp must be kept relatively slow, below a few Hz, in order to avoid hysteretic drift effects from ramp to ramp.

This PC alignment process should then be repeated for PC2, however, the fast axis of the PC should now be optimized to be in the horizontal plane. This configuration does not change the amount of horizontally and vertically polarized components, it just induces a phase between them. There are several ways to optimize PC2. First one can temporarily place a polarizer at 45 ° and detect with vertical polarization, giving a full extinction ratio measurement as minimizing transmission through crossed polarizers while the PC2 is swept. A second approach uses horizontally polarized light. One can verify that the transmission through a vertical polarizer does not change as the 2D PC is swept. This configuration is an insensitive measure of the field because $I \propto |E|^2$ so, a 10^-4 extinction intensity measurement gives only percent level field information.

Once both PC's are aligned with acceptable extinction ratios (typically $\approx$ 1x10^{-4}), we characterize their full voltage response to determine $\theta(V)$ and $\beta(V)$. We do this by setting a polarizer and photodiode after PC2 (or the chamber if you wish to know about viewport birefringence) and sweeping the PC control voltages while simultaneously reading out the photodiode voltage. In this way, we can record the transmission for all potential operation settings. To gain the most information we use two polarizer settings, crossed vertical and 45° as shown in figures 6.4 and 6.5. The vertical polarizer setting, Fig. 6.4, returns the most information about PC1 and is nearly independent of the voltage applied to PC2. The 45° setting, Fig. 6.5, is best for calibrating the phase response of PC2. For clearer comparison Fig. 6.6

shows cross sections of the surface represented in Fig. 6.5.
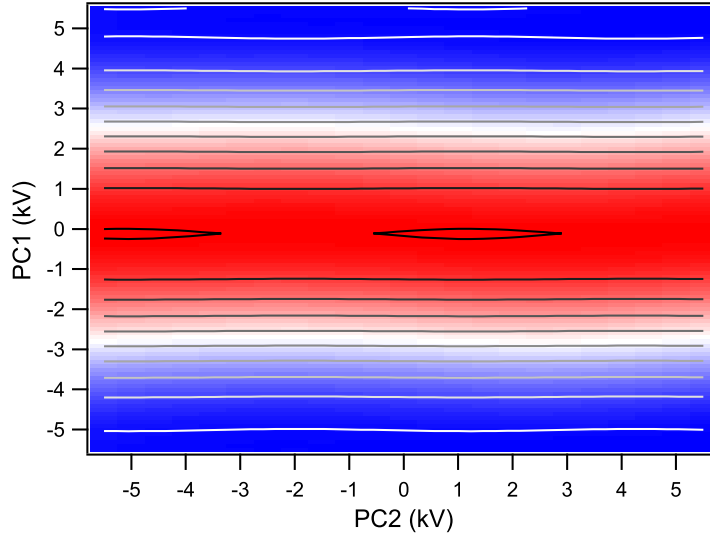
Figure 6.4: Characterization of the light transmitted through a vertical polarizer for all Pockels cell voltages. Data is represented by the colored plot and a best fit is displayed as a gray scale contour plot. Red corresponds to minimal transmission while blue corresponds to nearly full transmission. Ideally, in this configuration the input PC entirely controls the amount of vertically polarized light and the second PC has no effect. After alignment of the axis of the second PC there is little dependence. The gray scale contours correspond to a two variable fit to the data surface.

Next the second pass of the lattice beam through the atomic cloud, $\vec{k}_2$, must be aligned. This is most easily realized by recording the insitu (zero time of flight) position of the BEC and then loading the lattice and dipole 1, (with the lattice retroreflector, $\vec{k}_3$ and $\vec{k}_4$, blocked) and looking for an increase in atomic density at the overlap of the beams. Since the atoms are localized along a 1D tube, we only need to blindly search in the vertical direction and this method converges rapidly. Once a density peak is found, it can be readily adjusted to be centered on the position of
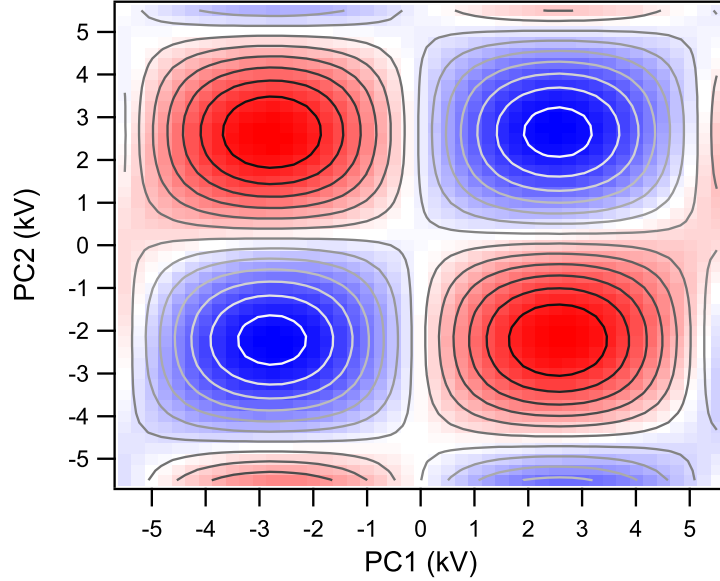
Figure 6.5: Characterization of the light transmitted through a 45° polarizer for all Pockels cell voltages. Data is represented by the colored plot and a best fit is displayed as a gray scale contour plot. Red corresponds to minimal transmission while blue corresponds to nearly full transmission. Extinction ratios in this case are limited by our ability to correctly set the polarizer to 45°. However, we can still extract the phase of the 2D Pockels cell as a function of voltage. The gray scale contours correspond to a two variable fit to the data surface.

the BEC. Again, the outcome of this process should be checked by "dipole pulling".

With the first two k vectors of the lattice aligned to the BEC, the next step is to align the retro reflecting mirror, thus fixing both $\vec{k_3}$ and $\vec{k_4}$. The first step is simply overlapping the back reflection from the retro mirror onto the incident beam. Since the lever arm from the retro mirror is ≈ 80 cm from the lattice fiber launch and the spotsize of the lattice beam is ≈ 1 mm, the angular accuracy of this basic alignment is again quite good, and an effect on the BEC should be immediately visible. The last step of this alignment is to use diffraction of the BEC off of the 2D
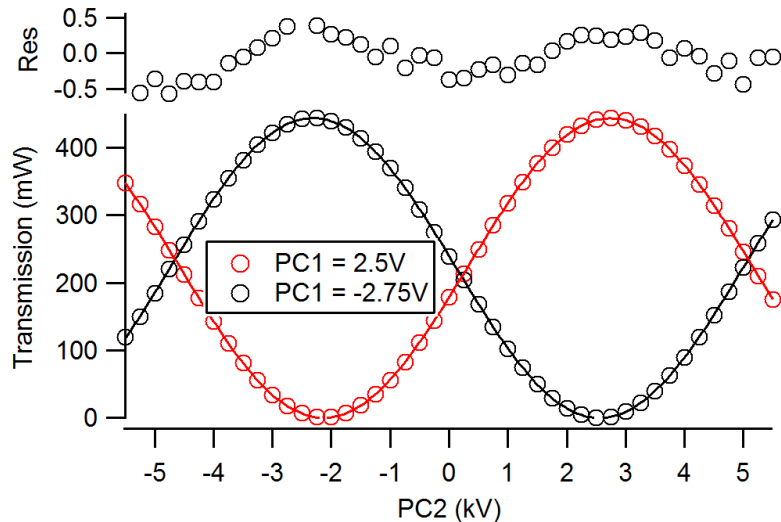
Figure 6.6: Characterization of the light transmitted through a 45° polarizer for approximate quarter wave values of the input Pockels cell.

optical lattice to optimize the retro reflector alignment. The optimum short-pulse diffraction pattern will have the most possible occupation in the highest momentum orders and will be as symmetric in 2D as possible (all four first order diffraction peaks should have the same population).

6.2.3 Pockels cell temporal response

Once the lattice is spatially aligned and characterized, the temporal response of the PC's must also be characterized. When switching from a large applied voltage to a small applied voltage (as in moving from addressing to dynamics configurations in the lattice), we have observed 100 ms scale relaxation of the transmitted light through a crossed polarizer. This behavior is shown in the red trace in Fig. 6.7. This relaxation could be due to leakage to a capacitance in the lines to the PC as well as

within the PC itself. In fact, we have only observed significant relaxation behavior in PC1 while PC2 seemed relatively well-behaved. By measuring the polarization response for several control voltages, we were able to choose parameters to remove the drift by feeding forward an exponentially decaying voltage offset in addition to the standard control voltage. The black trace in Fig. 6.7 shows the response with feed forward implemented. Any remaining noise and residual drift would show up as $\lesssim 10$ Hz lattice imperfections.
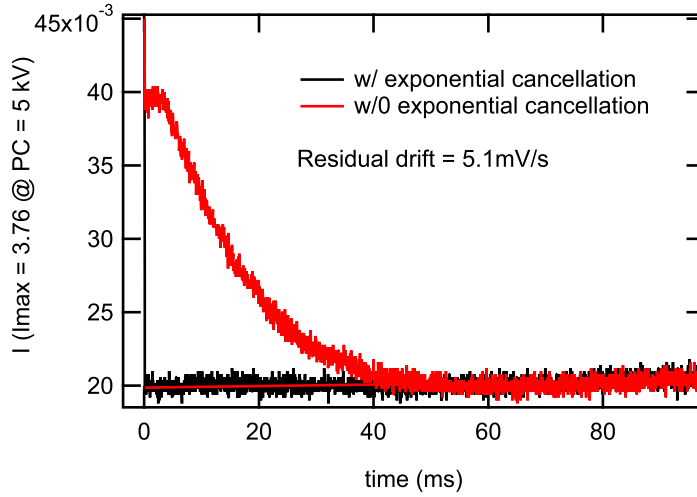
Figure 6.7: Measured polarization relaxation of PC1.

6.2.4 Vertical Lattice

To complete the three dimensional confinement of atoms, we implemented a vertical lattice in a "Bow tie" configuration derived from the Ti:saph, but offset in frequency from the 2D lattice by ≈ 160 MHz. In this configuration, two linearly polarized beams intersect at 142° and the resultant lattice is formed with a period-

icity, $\lambda/(2\sin(\theta_{vert}))$ (about 430 nm in practice). The plane, defined by the lattice beams, is orthogonal to the Zeeman slower and produces a lattice along $\hat{z}$. This bow tie setup allows imaging along the direction of gravity. The angle of the beam intersection is just larger than the numerical aperture of the imaging system. The beam waists are $\approx$250 μm and the power in the beams is typically $\approx$250 mW. The depth is calibrated daily by Kapitza-Dirac diffraction to check for relative alignment drift between the lattice and the crossed dipole trap.

6.3 Atomic probes for accurate alignment

Once the lattice is roughly aligned following the procedures just outlined, one can begin a number of further explorations to better understand the lattice. Our diagnostic tools include; lattice diffraction, bandmapping, Talbot enhanced diffraction, magnetic field sensitive and insensitive microwave spectroscopy, "ground-band diffraction" [189], and "phase running" in a double slit experiment [191].

6.3.1 Lattice diffraction and band mapping

Perhaps the most obvious and simple to implement probe of the lattice structure is atomic diffraction by the optical lattice. Diffraction probes the momentum space structure of the lattice and allows us to qualitatively compare the $\lambda/2$ spaced lattice to λ (again actually $\lambda/\sqrt{2}$ rotated by 45°) spaced lattice. Since the recoil momentum in the longer wavelength $\lambda/\sqrt{2}$ lattice is smaller, the first order diffraction peaks after time of flight, appear $1/\sqrt{2}$ closer to the central un-diffracted peak

than the $\lambda/2$ spaced lattice.

In the Kapitza-Dirac limit, we ignore the kinetic energy term and atom-atom interactions in the Hamiltonian compared to the potential energy of the lattice. This is valid if the atoms move little compared to a lattice spacing during the lattice pulse time. We use this method to calibrate the lattice depth by measuring the relative populations in the zeroth and first order diffraction peaks. In this limit, the lattice depth as a function of diffraction ratio has a simple functional form, $R_{0/1} = J_0^2(x)/J_1^2(x)$ where $x = (U_{latt}t_{pulse})/(2\hbar)$, which can be inverted to determine lattice depth. This measurement is most accurate when the peaks have approximately equal weight and any optical-depth dependent systematics cancel out. However, we rarely observe a significant diffraction ratio dependent discrepancy in calculated lattice depth.

The difference between lattices can also be observed by "band mapping", ideally, lowering the lattice adiabatically with respect to band excitation but quickly compared to atom-atom scattering interactions [195]. As the lattice is loaded, the atomic dispersion changes from parabolic, as a free particle, to nearly momentum independent in a deep lattice. The momentum of the BEC evolves from localized near zero to fill the lowest band of the lattice. Adiabatic deformation of the dispersion relation to back to parabolic during bandmapping should return a sharp momentum distribution. However, interactions and even small lattice induced heating prevent this. Thus the lowest Brillouin zone becomes nearly filled, and after time of flight provides a direct visualization of the Brillouin zones. The lowest Brillouin zone of the $\lambda/2$ lattice appears as a square with width $2\hbar k$ and the lowest Brillouin zone of

the λ lattice appears as a diamond with its edges at the centers of the $\lambda/2$ lattice Brillouin zone (again the with in momnetum space of the λ lattice is reduced by a factor of $1/\sqrt{2}$). In practice, it is often hard to convincingly see diamond of the λ lattice Brillouin zone. A lack of sharp corners from bandmapping could be due to a lack of population at higher momentum due to low temperatures.

6.3.2   Talbot Pulsing of the $\vec{k_1}$-$\vec{k_2}$ lattice

The lattice beam orthogonality can be tested by blocking the retro reflecting mirror ($\vec{k_3}$ and $\vec{k_4}$) and looking for diffraction from the $\vec{k_1}$-$\vec{k_2}$ beams polarized in the plane. If the two beams were perfectly orthogonal and the polarization was perfectly in the 2D plane, there would be no diffraction at all. However, any imperfections will allow diffraction to occur from a small residual $\vec{k_1}$-$\vec{k_2}$ lattice. The Zeeman projection of the atoms is also crucial, since even for perfectly orthogonal beams, there is still a standing wave polarization interference pattern which will diffract $m_f \neq 0$ atoms. The small diffraction signals can be magnified by Talbot pulsing the lattice for a duration of half the Talbot time [196], $\tau_{Talbot/2} = h/(8E_r) = 68~\mu s$, interspersed by dark times of half the Talbot time. This process coherently places atomic population in higher momentum orders and amplifies the diffraction signal. In practice, we typically use 8 Talbot pulses, though sometimes, more does increase the signal. Varying input PC voltage we can check that zero applied voltage results in zero diffraction. Figure 6.8 shows the typical characterization of lattice beam orthogonality via Talbot pulsing. The diffraction ratio in this case is the amount

of atomic population in higher momentum states. Using all Ti:saph power and 23, 68us pulses, we could detect a faint diffraction peak from a $\vec{k}_1$-$\vec{k}_2$ lattice. From this we ended up moving the k2 lattice mirror $\approx$0.25 mrad. This corresponds to a 100 Hz offset in a 30 Er lattice.

Stray reflections of of optics may also create extremely weak, but still relevant, optical lattices with spacing $\lambda/2$. We check for these using the same procedure but with $\tau_{Talbot/2} = 34\ \mu s$ to account for the shorter period. We removed back reflections off of elements by tilting optical surfaces slightly and checking for the disappearance of a diffraction signal.
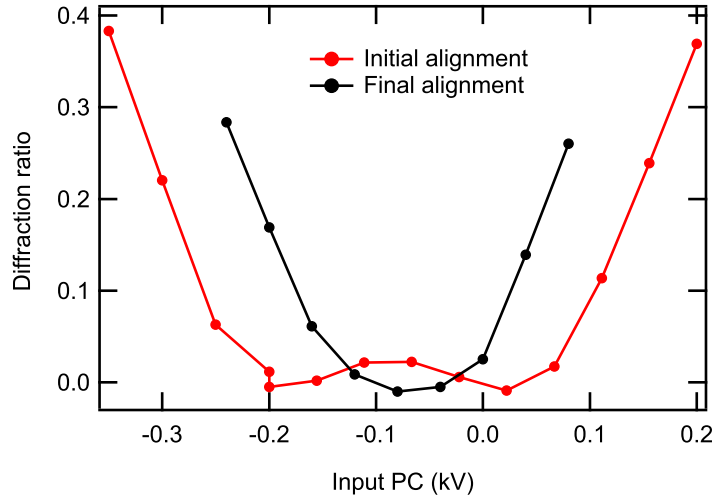
Figure 6.8: Talbot pulse measurement of beam orthogonality. The initial configuration shows a double minima structure due to the zero crossing of the tilt. The final configuration shows single minimum consistent with a tilt near zero.

Angular alignment of the bias magnetic field in the plane of the lattice is also done by Talbot pulsing atoms in states with $m_f \neq 0$. If there is a component of the bias field out of the plane, it will add with the $\vec{k}_1$-$\vec{k}_2$ interference pattern and

129

produce diffraction. By monitoring diffracted atom population as a function of $\hat{z}$ bias magnetic field, we can find a minimum (with no detectable diffraction) and set the field direction.

Angular alignment of the magnetic field in the plane is done by performing Rabi spectroscopy for different values of the shim fields. The measured linecenters as a function of applied field and a Breit-Rabi calculation allow us to extract the ambient field magnitude and the current response of the shim coils. There is an overall angular uncertainty related to the relative angle between lattice beams and the mounting of the coils to the chamber but, this estimate can be further refined by preforming high resolution site resolving spectroscopy and observing the disappearance of a sublattice-dependence

6.3.3 Sublattice resolving spectroscopy

An important probe of the vector light shift from our lattice is RF or microwave spectroscopy as originally reported in [190]. We expect to be able to apply of order 10 kHz effective field shift, which we can probe directly with Rabi spectroscopy provided that Fourier limit of our Rabi pulse is smaller than the applied shift. Since we must probe magnetically sensitive transitions, our pulse time is limited to less than a quarter period of the 60 Hz magnetic field noise associated with AC power. Using the bias magnetic field described in section 6.1 the shift from $\vec{B}_{eff}$ can be applied to one sub lattice leaving the other un-shifted. The sublattices will be degenerate for horizontal linear polarization. Increasing the beam ellipticity by
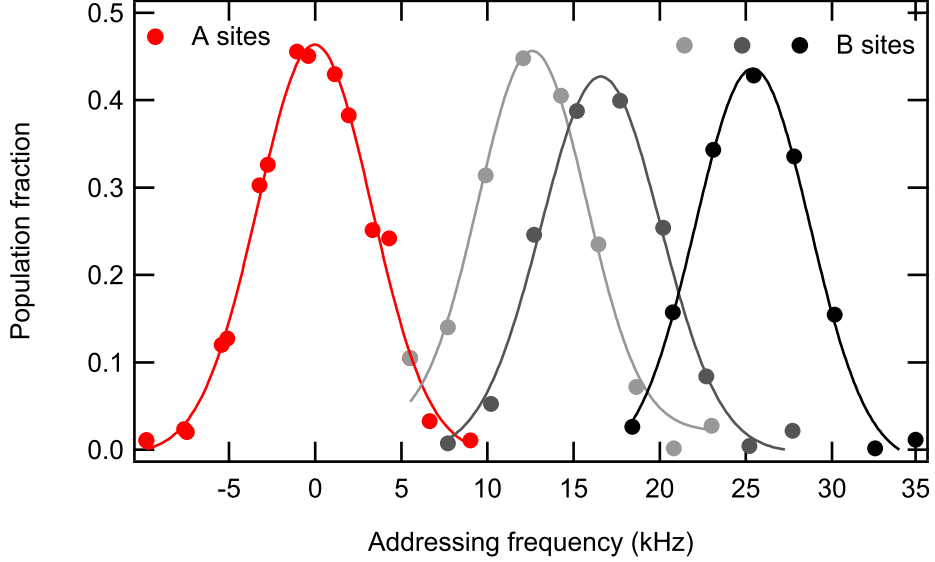
Figure 6.9: The A sites, left, experience no vector light shift while the B sites are spectroscopically separated with increasing lattice beam elipticity.

applying a voltage to PC1 breaks the sublattice degeneracy. We use the $|1, -1\rangle \rightarrow |2, -2\rangle$ transition because it has (from the g factor) three times the magnetic field sensitivity of a $m_f = 1 \rightarrow m_f = 0$ transition, so we get the most shift per applied $\vec{B}_{eff}$.

We check this transition daily with the vector tilt applied to the B sites using 108μs pulses (136μs is a π pulse) to tweak up the microwave transition center frequencies and check for drifts in the lattice alignment or bias magnetic field. Figure 6.9 shows three spectra taken with different lattice elipticities. The most distantly separated peaks represent the lattice during typical addressing conditions for the experiment reported in the following chapter. The day-to-day drift in tilt is ≈ 100 Hz out of ≈ 27 kHz. Repeating this spectroscopic procedure with the scalar

tilt applied on A sites using 2.5 ms pulses showed $\approx$250 Hz broadening, which places an upper bound on the inhomogeneity in $\vec{B}_{eff}$.

6.3.4 Lattice offset characterization via phase running

One of the central problems in setting up this lattice is accurately characterizing the sublattice offset Δ as a function of lattice control parameters. We have discussed the accuracy with which various "offline" measurements can determine lattice parameters. Even if they could be estimated with sufficient accuracy, we must still demand verification "with the atoms". There are two conceptually related methods ("ground band diffraction" and "phase running") that determine Δ by taking an initial wave function, splitting it, allowing it to time evolve in the presence of the sublattice offset Δ. The first of these methods is "ground band diffraction", where a BEC is loaded into the 2D lattice quickly compared to interactions, but slow compared to lattice band spacings (hence the ground band part), allowed to time evolve in a staggered lattice and then snapped off, creating a diffraction pattern. In this experiment, the populations in the reciprocal lattice space oscillate between the $\lambda/2$ and λ lattice. The rate of oscillation is proportional to the applied Δ. This technique has the advantage that the lattice is in steady state with respect to PC relaxation time scales because it does not need to be dynamically manipulated. Ground band diffraction in principle provides sufficient information in a less experimentally demanding configuration than "phase running" (described below). However, there remain a number of uncontrolled systematics likely related
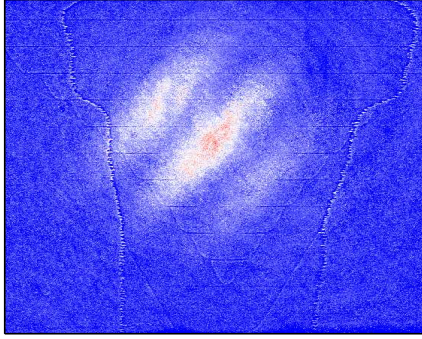
Figure 6.10: An absorption image of matter wave double slit interference, created when a λ period lattice is loaded then quickly deformed into a $\lambda/2$ period lattice. The lattice is then snapped off and the atomic cloud is allowed to expand and interfere with itself in time of flight.

to density and inhomogeneous lattice dephasing that complicate the interpretation of the time evolution of the diffraction pattern.

The second method is double slit phase running [191], and despite its technical demands (vertical lattice, low filling, PC hyseteretic dynamics and associated band excitation) it is a favorite characterization technique because it is able to measure not only the magnitude of the lattice offset, but also the sign of the offset. In this experiment, the 3D lattice with λ spacing in the 2D plane, is loaded slowly compared to interactions into Mott insulating state. The 3D array of isolated sites are then split, as shown in figure 6.2, and a tilt is applied to the "state independent" B sublattice. After waiting a variable time, the lattice is snapped off, and the split atoms interfere in time of flight, yielding a double slit interference pattern shown in 6.10. The timing of the phase running experiment is outlined in table 6.1. (The necessary Pockels cell manipulations mean that the Pockels cells have not fully

133

relaxed and thus the tilt is not at its steady state value which must be taken into account.) As the atomic phase winds due to the applied Δ, the position of the interference fringes translates as a function of the hold time in the tilted-isolated double wells. By fitting to the absorption image, we record this position and measure the velocity of the fringe motion. To increase accuracy, we measure after a revival so that the interaction time is sufficient to resolve slow fringe time evolution. Repeating this experiment for different hold times, applied offsets Δ and different internal spin state generates the summary plot shown in fig. 6.11. This plot is central to our characterization of the lattice and comparison to our lattice simulation. We found that for the measured depth and PC responses the fit curves matched well to our lattice calculations up to an overall voltage shift, related to the fact that the PC's were characterized in steady state and the phase running measurements were taken before relaxation could occur. Perfect alignment would mean that the curves for all three Zeeman projections would cross at zero sublattice offset. In this measurement, we observe imperfections on the order of 100 Hz in a 33 E_r lattice ($\approx$ 115 kHz total depth).

Table 6.1: Phase running experimental sequence

Step	Time
Load a λ lattice $32.7E_r$	100ms
split lambda lattice sites in half	466μs
move 2D PC to B sites	466 μs
tilt B sites	466μs
wait for time evolution	<2ms
snap off lattice	$\approx 1\mu$s
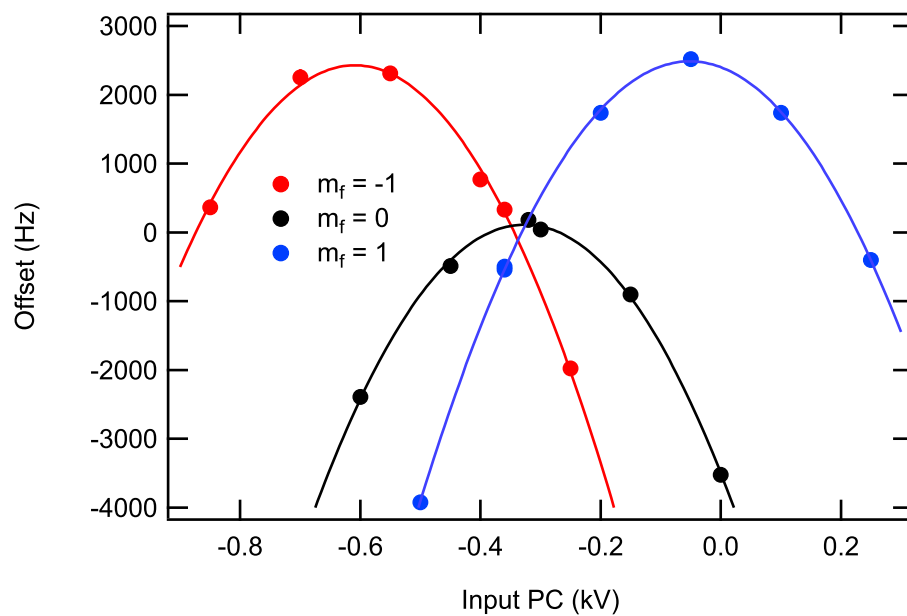
Figure 6.11: Measured offsets Δ_σ at short times relative to input pc relaxation. Error bars due to linear fitting of the phase vs. time are generally smaller than the markers.

6.3.5   Number resolving spectroscopy in the MI

We have discussed microwave spectroscopy as a probe for state dependent shifts. If we wish to probe the state of the atoms rather than the lattice we may use field insensitive transitions. Such transitions are called clock transitions because their environmental isolation makes them well suited as oscillators for time keeping. Previously, our group has investigated a number of magic wavelength configurations [197, 198] where the differential AC Stark shift on microwave transitions can be controlled by lattice and magnetic field configurations which have applications to trapped atom clocks. However in this experiment, we probe the first order magnetically insensitive $|1, -1\rangle \rightarrow |2, 1\rangle$ transition which around 3.23G is linearly insensitive to magnetic field [187, 199] using a two field microwave+RF coupling with a $\lesssim 100$ kHz intermediate detuning from the $|2, 0\rangle$ state. Due to percent level differences in the F=1 and F=2 scattering lengths [200], Rubidium has a spin dependent interaction energy which gives rise to a frequency shift, $\delta\nu = U(a_{21} - a_{11})/(ha_{11})$, which in a $\approx 30E_R$ lattice this gives $\delta\nu \approx 50$ Hz. Due to the environmental decoupling, we are able to use 80 ms Rabi pulses with an area $< \pi$. This resolution enables us to see atomic interaction shifts as shown in figure 6.12. In a system with continuous density variation, this would create an asymmetric lineshape where the greatest frequency shift occurs at the peak density but with vanishing weight due to the small fraction of the sample at the peak density. In a Mott insulator however, the density is discretized to have integer filling per lattice site. This creates discrete peaks in the spectrum rather than a broadened lineshape. It should be noted that
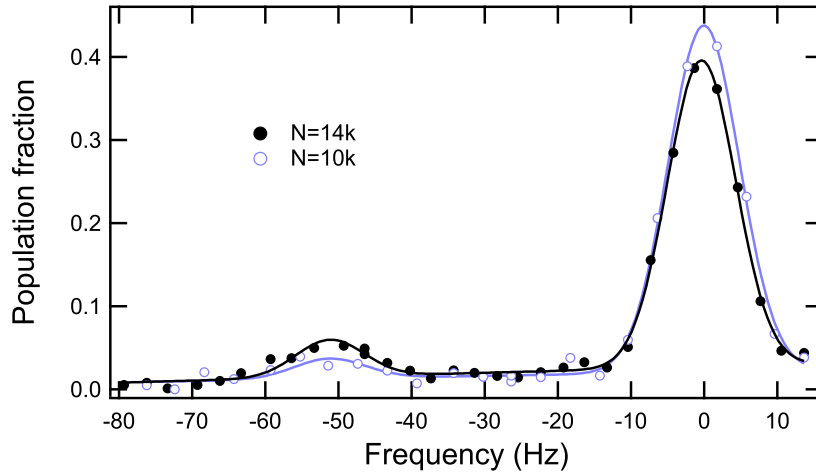
Figure 6.12: Reduction of the 2's peak with increasing throwaway. Black trace is with $14*10^3$ atoms, lavender trace is with $10*10^3$ atoms. Both data sets are fit with two Gaussian functions.

direct interpretation of the weights of this spectrum is involved and may well require knowledge of trap anharmonicities [201]. But, it is easy to get qualitative insight into the relative number of singly and doubly occupied sites. As we reduce the atom number, the peak associated with double occupation vanishes. Shot-to-shot fluctuations limit our knowledge of double occupation at the percent level.

Chapter 7:   Non-equilibrium dynamics

The interplay of magnetic exchange interactions and tunneling underlies many complex quantum phenomena observed in real materials[1]. We study nonequilibrium magnetization dynamics in an extended 2D system by loading effective spin-1/2 bosons into a spin-dependent optical lattice, and we use the lattice to separately control the resonance conditions for tunneling and superexchange. After preparing a nonequilibrium antiferromagnetically ordered state, we observe relaxation dynamics governed by two well-separated rates, which scale with the underlying Hamiltonian parameters associated with superexchange and tunneling. Remarkably, with tunneling off-resonantly suppressed, we are able to observe superexchange dominated dynamics over two orders of magnitude in magnetic coupling strength, despite the presence of vacancies. In this regime, the measured timescales are in agreement with simple theoretical estimates, but the detailed dynamics of this 2D, strongly-correlated, and far-from-equilibrium quantum system remain out of reach of current computational techniques.

---

[1]At the time of this writing, the bulk of this chapter has been submitted [10]

7.1 Introduction

The interplay of spin and motion underlies some of the most intriguing and poorly understood behaviors in many-body quantum systems [179]. A well known example is the onset of superconductivity in cuprate compounds when mobile holes are introduced into an otherwise insulating 2D quantum magnet [202]; understanding this behavior is particularly challenging because the dimensionality is low enough to support strong quantum correlations, but high enough to prohibit numerical solution. Ultracold atoms in optical lattices realize tunable, idealized models of such behavior, and can naturally operate in a regime where the quantum motion (tunneling) of particles and magnetic interactions (superexchange) explicitly compete [173, 180].

For ultracold atoms in equilibrium, the extremely small energy scale associated with superexchange interactions makes the observation of magnetism challenging, and short-range antiferromagnetic correlations resulting from superexchange have only recently been observed [150, 153]. Out of equilibrium, superexchange-dominated dynamics has been demonstrated in isolated pairs of atoms [151], in 1D systems with single atom spin impurities [203], and recently in the decay of spin-density waves [204]. However, the perturbative origin of superexchange in these systems requires that it be weak compared to tunneling, and thus the manifestation of superexchange requires extremely low motional entropy. Dipolar gases [131] and ultracold polar molecules [205] in lattices provide a promising route toward achieving large (non-perturbative) magnetic interactions [206], but, technical limitations in these systems currently complicate the simultaneous observation of motional and

spin-exchange effects.

Here, we study the magnetization dynamics of effective spin-1/2 bosons in a 2D optical lattice following a global quench from an initially antiferromagnetically ordered state [167]. The dynamics we observe is governed by a bosonic t-J model [207–211]. Utilizing a checkerboard optical lattice, we continuously tune the magnetization dynamics from a tunneling-dominated regime into a regime where superexchange is dominant, even at relatively high motional entropies. This experiment bridges the gap between experiments studying the non-equilibrium behavior of systems with exclusively motional [155, 212–215] or spin degrees [216, 217] of freedom, demonstrating the requisite control to explore the intriguing intermediate territory in which they compete. In addition, the techniques we demonstrate lay the groundwork for adiabatic preparation of low entropy spin states relevant for studies of equilibrium quantum magnetism [163, 164].

Our experiment uses two hyperfine spin states (denoted by $\uparrow$, $\downarrow$) of ultra-cold ^{87}Rb atoms trapped in a dynamically controlled, 2D checkerboard optical lattice [189] comprised of two sub lattices A and B (Fig. 1a). For most experimental conditions presented here, our system is well described by a Bose-Hubbard model [173] characterized by a nearest neighbor tunneling energy J, and an on-site interaction energy $U > 0$. In addition, we use the lattice to apply an energy offset $\Delta_\sigma = \Delta + \delta_\sigma$ between the A and B sub-lattices, consisting of a spin-independent part Δ and a spin-dependent part δ_σ acting as a staggered magnetic field ($\sigma \in \{\uparrow, \downarrow\}$) [190]. All of these parameters can be dynamically controlled, which we exploit to prepare initial states with 2D anti-ferromagnetic order and to observe
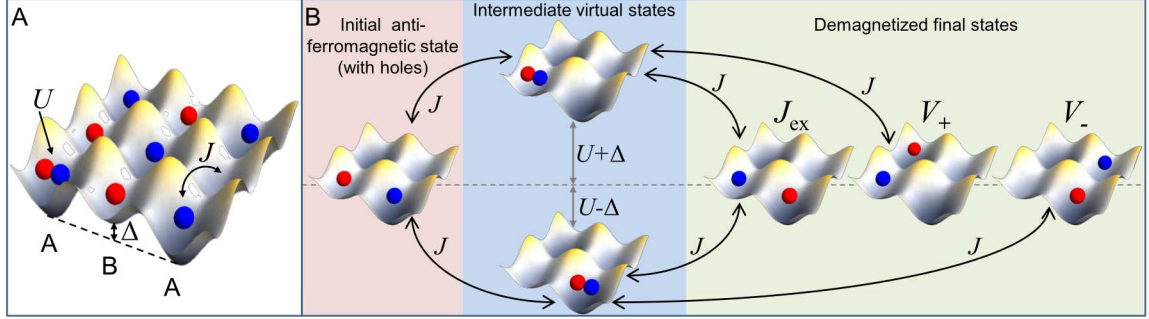
Figure 7.1: **Tunable exchange processes. (A)** Schematic of terms in the underlying Bose-Hubbard Hamiltonian: onsite interaction energy between two atoms U, tunneling J, and sub lattice offset, Δ. **(B)** Second order magnetic coupling processes arising from exchange between occupied nearest neighbor sites (J_{ex}) or hole-mediated exchange associated with hopping of a hole within one sub-lattice (V_+ and V_-). These couplings dominate the magnetization dynamics when tunneling is suppressed by tuning $|\Delta| \gg J$.

the resulting dynamics following a quench to different values of J, U, Δ, and δ_σ.

7.2   Hamiltonian

At unit filling, for $U \gg J$ and $\Delta_\sigma = 0$, double occupation at each site is allowed only virtually and the Bose-Hubbard model can be mapped onto a ferromagnetic Heisenberg model [180, 218] with a nearest neighbor magnetic interaction strength J_{ex} that is second order in the tunneling energy. In the presence of hole impurities, first order tunneling (with the much larger energy scale J) must be included, which significantly modifies the dynamics even at low hole concentrations [204]. The offset Δ_σ provides the flexibility to tune the relative importance of first order tunneling and second order superexchange processes. For example, below unit filling, if $|U - \Delta| \gg$

J and δ_σ, the Bose-Hubbard model can be mapped onto a bosonic t-J model (a J-J_{ex} model in our notation, since t represents time) with a staggered energy offset:

$$
\begin{aligned}
H \;=\; & -J \sum_{\langle i,j \rangle, \sigma} a_{i\sigma}^\dagger a_{j\sigma} - \sum_{j \in A, \sigma} \Delta_\sigma a_{j\sigma}^\dagger a_{j\sigma} \hspace{2cm} (7.1)\\
& -J_{\text{ex}} \sum_{\langle i,j \rangle} \boldsymbol{S}_i \cdot \boldsymbol{S}_j - \sum_{\langle i,j,k \rangle, \sigma\sigma'} V_j \left(a_{i\sigma}^\dagger \boldsymbol{\tau}_{\sigma\sigma'} a_{k\sigma'} \right) \cdot \boldsymbol{S}_j .
\end{aligned}
$$

The local spin operators are defined as $\boldsymbol{S}_i = \frac{1}{2} \sum_{\sigma\sigma'} a_{i\sigma}^\dagger \boldsymbol{\tau}_{\sigma\sigma'} a_{i\sigma'}$, where $a_{i\sigma}$ $(a_{i\sigma}^\dagger)$ annihilates (creates) a hardcore boson of spin σ on site i, and $\boldsymbol{\tau}$ is a vector of Pauli matrices. The notation $\langle i, j \rangle$ indicates the sum over i and j is restricted to nearest neighbors, and $\langle i, j, k \rangle$ indicates the sum is restricted to sites i, j, k such that $i \neq k$ are both nearest neighbors of j. The superexchange energy $J_{\text{ex}} = 4J^2 U/(U^2 - \Delta^2)$ (Fig. 1b) can be either ferromagnetic ($U > \Delta$) or anti-ferromagnetic ($U < \Delta$) [151]. The last term describes hole-mediated exchange between sub lattices where an atom on site k interacts via superexchange with an atom on site j, while simultaneously hopping to site i (Fig. 1b). Here $V_j = V_\pm \equiv J^2/(U \pm \Delta)$, where $-(+)$ applies when $j \in A(B)$. In writing Eqn. 7.1 we have ignored second-order processes [219, 220] that conserve sub-lattice magnetization [221]. When $|\Delta| \lesssim J$, first order tunneling is resonant and dominates over hole mediated exchange. For $|\Delta| \gg J$, however, first order tunneling is effectively suppressed, in which case the frequently ignored V_j term plays an important role in hole motion and must be included. Similarly, superexchange is resonant when $|\delta_\sigma| \lesssim J_{\text{ex}}$, but is suppressed when $|\delta_\sigma| \gg J_{\text{ex}}$. The values of J, U, Δ, and δ_σ are determined from an experimentally calibrated model of the lattice [221]. Inhomogeneity in the system, arising e.g. from trap curvature,
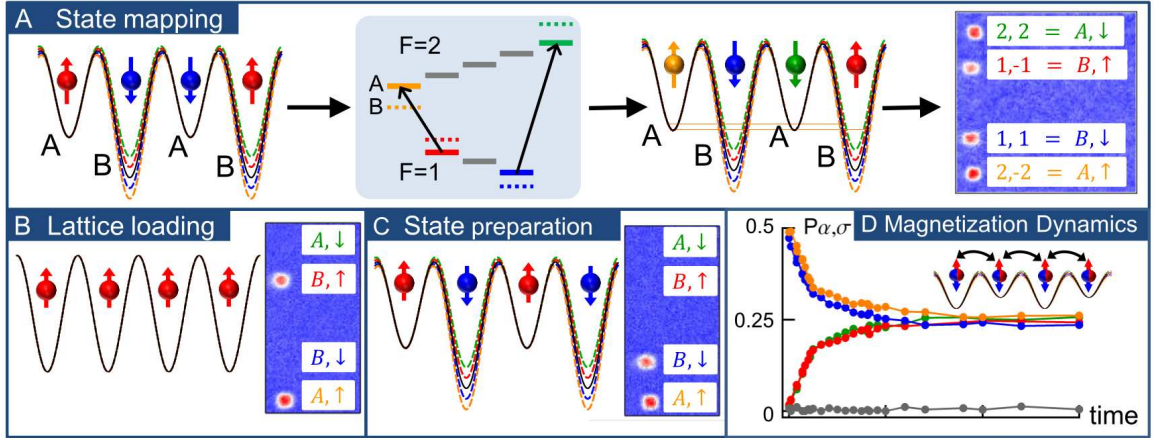
Figure 7.2: **Schematic of experimental sequence. (A)** Spin/sub lattice mapping: Atoms in $|\uparrow\rangle$ (red) or $|\downarrow\rangle$ (blue) occupy either the A or B sub-lattice (shown on the left). Applying a spin dependent addressing offset to the B sub-lattice spectroscopically resolves the A and B sub-lattices (colored lines correspond to the potentials and energy levels seen by different hyperfine states). The $|A,\uparrow\rangle$ and $|A,\downarrow\rangle$ populations are microwave transferred to two different hyperfine states (yellow and green respectively), and the four mapped populations are measured by absorption imaging after Stern-Gerlach separation (shown on the right). **(B)** Initial lattice loading: A spin-polarized $|\uparrow\rangle$ unit filled Mott insulator. **(C)** Microwave state preparation: B sites are microwave transferred from $|\uparrow\rangle$ to $|\downarrow\rangle$ using similar techniques to those employed for the state readout shown in **(A)**. **(D)** Time evolution: After the lattice is quenched to a specific configuration, the sub-lattice/spin populations are measured as a function of time (including the non-participating $m_F = 0$ hyperfine state shown in gray).

primarily enters via inhomogeneities in the parameters Δ and δ_σ.

7.3   Experiment

The experiments begin with $\lesssim 12 \times 10^3$ ^{87}Rb atoms loaded into a square 3D optical lattice with one atom per site [221], initially spin polarized in the state $|\uparrow\rangle$. We use the hyperfine states $|\uparrow\rangle \equiv |F=1, m_F=-1\rangle$ and $|\downarrow\rangle \equiv |1, +1\rangle$ to represent

the pseudo-spin-1/2 system. The 3D lattice is comprised of a vertical lattice along z which confines the atoms to an array of independent 2D planes, along with the dynamic 2D checkerboard lattice in the x-y plane. The vertical lattice depth is typically $V_z = 35$ E_{R}, held constant throughout the experiment, and the 2D lattice depth is initially $V_{xy} = 30$ E_{R} with no staggered offset, $\Delta_\sigma = 0$ (The recoil energy $E_{\mathrm{R}} = h^2/(2m\lambda^2)$, $E_{\mathrm{R}}/h = 3.47$ kHz, where m is the mass of ^{87}Rb and $\lambda = 813$ nm). The atoms occupy roughly 13-15 2D planes, with the central plane containing 800-1100 atoms. The ratio of surface lattice sites to total lattice sites of the trapped cloud is $\approx$15 % and sets a zero temperature lower bound for the number of sites with neighboring holes. Based on spectroscopic measurements and assuming a thermal distribution [221], we estimate the hole density averaged over the entire cloud to be about 25 %, and the hole density at the center of the cloud to be about 7 %.

To measure the spin population independently on each sub-lattice, we map the four spin-spatial states $|A\uparrow\rangle$, $|A\downarrow\rangle$, $|B\uparrow\rangle$ and $|B\downarrow\rangle$ on to four distinct Zeeman states (Fig. 2a): By applying a large state-dependent offset δ_σ to all B sites we transfer the spectroscopically resolved A-site atoms to two additional readout hyperfine states, $|A\uparrow\rangle \rightarrow |2, -2\rangle$ and $|A\downarrow\rangle \rightarrow |2, +2\rangle$ [190]. The four normalized populations $P_{\alpha,\sigma}$ ($\alpha \in \{A, B\}$) are measured with absorption imaging after Stern-Gerlach separation in a magnetic field gradient.

To perform the experiment, we start with a spin polarized configuration (Fig. 2b), and construct an initial state with staggered magnetization by applying the addressing offset δ_σ and transferring the B-site atoms to $|\downarrow\rangle$ (Fig. 2c). After returning δ_σ to zero we initiate dynamics by quenching to a given configuration with

lattice depth V_{xy} and offsets Δ and δ_σ (Fig. 2d). The ramp time for the quench of 200 μs was chosen to be fast with respect to subsequent dynamics but slow enough to avoid band excitation. After a variable hold time, we freeze the dynamics by raising V_{xy} to 30 E_R and read out the populations $P_{\alpha,\sigma}$, from which we determine the staggered magnetization M_s and the sub lattice population difference P_{A-B}:

$$
\begin{aligned}
M_s(t) &\equiv P_{A,\uparrow}(t) + P_{B,\downarrow}(t) - P_{A,\downarrow}(t) - P_{B,\uparrow}(t), \\
P_{A-B}(t) &\equiv P_{A,\uparrow}(t) + P_{A,\downarrow}(t) - P_{B,\uparrow}(t) - P_{B,\downarrow}(t).
\end{aligned}
\tag{7.2}
$$

The exchange terms in Eqn. 7.1 conserve P_{A-B}, while the first order tunneling does not, allowing for population transport between sub lattices. We also monitor the total spin imbalance $P_{\uparrow-\downarrow}$ and the $m_F{=}0$ population to quantify unwanted spin-changing processes that drive the atoms out of the spin-1/2 manifold containing $|\uparrow\rangle$ and $|\downarrow\rangle$. We measure the time for depopulation of the spin-1/2 manifold to be greater than 6 s and the atom number lifetime in the lattice to be greater than 3 s.

7.4 Observations

For the lattice parameters studied in this paper, the magnetization dynamics is well described by exponential decay, with decay time scales ranging between 0.5 ms and 500 ms. Example decay curves are shown in Fig. 3a for a lattice depth $V_{xy} = 15$ E_R and different offsets Δ. For some V_{xy} and Δ the exponential decay clearly occurs on two well separated time scales (Fig. 3a inset): a fast time scale, τ_f, which dominates the behavior in shallow lattices when $\Delta \approx 0$ or $\Delta \approx U$, and a
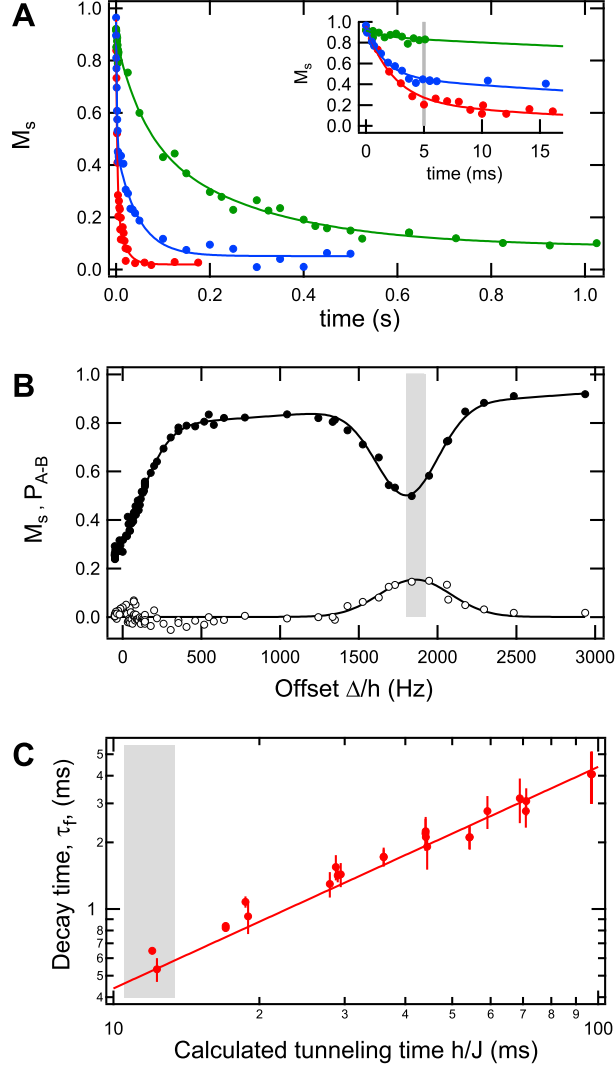
Figure 7.3: **Identification and control of tunneling (A)** Decay of magnetization at a lattice depth of 15 E_{R} for different offsets Δ/h of 1000 Hz (green), 300 Hz (blue), and -50 Hz (red). The inset shows the short time evolution, with two timescales ($\tau_f \approx 2$ ms and $\tau_s \approx 50$ ms), both visible in the $\Delta/h= 300$ Hz (blue) trace. The solid lines are double exponential fits. The vertical gray line indicates the fixed decay time at which the data in b) was taken. **(B)** Magnetization M_s (filled circles) and sub lattice population P_{A-B} (open circles) as a function of Δ at a fixed wait time of 5 ms $\gtrsim \tau_f$ after the quench. The fast magnetization decay is resonant at $\Delta = 0$ and $\Delta = U$, while sub-lattice transport occurs near $\Delta = U$. The vertical gray band represents the calculated U with an uncertainty due to parameter extraction from the two band model [221]. **(C)** The fast time scale, τ_f, vs. calculated tunneling time scale h/J for different lattice depths and $\Delta \lesssim J$. The solid line is $\tau_f = (h/J)/22$, and the gray band represents the uncertainty in the location of the 2D superfluid-insulator transition reported in Ref. [222]. (error bars represent the 1 standard deviation 146tatistical uncertainties from fitting).

slow time scale, τ_s, which dominates the behavior in deep lattices with larger offset, $|\Delta| \gg U, J$.

To investigate the faster time scale, we measure M_s and P_{A-B} at a fixed decay time for different Δ, as shown in Fig. 3b for $V_{xy} = 15$ E_{R}. The 5 ms decay time (indicated by the vertical line in Fig. 3a) was chosen so that nearly all of the fast decay but little of the slow decay occurred. The fast magnetization decay reveals resonant features at $\Delta = 0$ and U, where the decay rate at $\Delta = 0$ is twice as fast as at $\Delta = U$. In addition, P_{A-B} shows sub-lattice transport from B to A sites at $\Delta = U$, indicative of resonant first order tunneling. At $\Delta \approx 0$ the demagnetizing sub lattice transport $B \rightarrow A$ and $A \rightarrow B$ are balanced. We theoretically estimate the expected width of the $\Delta = U$ resonance in P_{A-B} to be $5J/h = 110$ Hz [221], which is significantly narrower than the 500 Hz width that we observe experimentally, suggesting inhomogeneous broadening. We note however, that the observed broadening is beyond what is expected from the measured trap curvature, and is inconsistent with estimates of light shift inhomogeneity from spectroscopic measurements [221]. A residual δ_σ could account for the width.

The measured decay times τ_f for a range of lattice depths are plotted against the calculated tunneling time h/J in Fig. 3a, showing a decay rate linear in J/h, with $h/(J\tau_f) = 22(2)$. This slope is comparable to a simple theoretical estimate taking only resonant tunneling into account, which predicts $h/(J\tau_f) \approx 2\pi\sqrt{2z} \approx 18$, with $z = 4$ the lattice coordination number. Given the relatively large average hole density near the surface of the cloud, the agreement with a non-interacting estimate is not surprising, though we would expect interactions to reduce the decay rate.
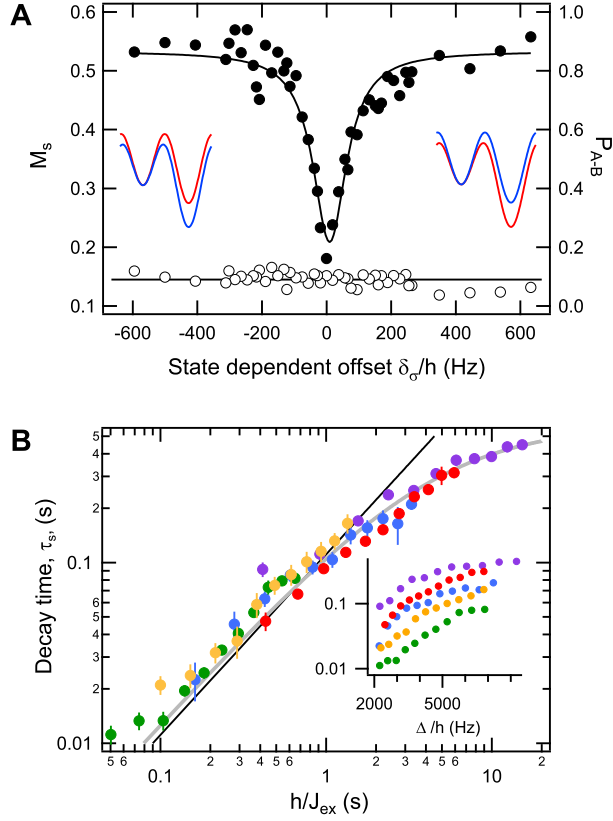
Figure 7.4: **Resonant superexchange (A)** Magnetization (filled circles) and sub lattice population difference (open circles) at a fixed wait time of 70 ms vs. spin dependent energy offset δ_σ for $V_{xy} = 9.4\ E_{\mathrm{R}}$ and $\Delta/h = 4.3$ kHz. The initial and final states of the second order processes are resonant ($\delta_\sigma = 0$), increasing the magnetization decay. The inset lattice potentials show the sign change of δ_σ across resonance for a fixed offset $\Delta > U$. **(B)** Measured slow decay time τ_s vs. calculated superexchange time h/J_{ex}: The filled purple, red, blue, yellow, and green markers represent lattice depths of 14.7, 13.2, 11.3, 9.4, and 7.5 E_{R} respectively. Inset: measured slow decay rate vs applied staggered offset Δ. The decay time scale, τ_s, collapses with h/J_{ex} over roughly two orders of magnitude in J_{ex}. The black line is a perturbative estimate of the scaling, which was checked in small systems by comparing to exact diagonalization averaged over hole-induced disorder [221]. The gray line is a fit to a saturated linear dependence of τ_s on h/J_{ex} (see text).

To investigate the slow dynamics, we measure the magnetization decay time τ_s for $\Delta > U$, where first order tunneling was negligible and superexchange should dominate the dynamics. To determine the dependence of τ_s on the spin-dependent staggered offset δ_σ, we measure the remaining staggered magnetization M_s and population difference P_{A-B} after a fixed wait time $\approx \tau_s$, as shown in Fig. 4a for a lattice depth 9.4 E_R and offset Δ/h=4.3 kHz. As expected for superexchange dynamics, the magnetization decay is resonant in δ_σ. The full width at half maximum of the Lorentzian fit to the resonance is 126(14) Hz, considerably narrower than the observed tunneling resonances shown in Fig. 3b, and is most likely dominated by inhomogeneous broadening (second order exchange processes are sensitive to inhomogeneity in both Δ and δ_σ). Figure 4a also shows that there is negligible sub-lattice transport associated with the demagnetization resonance. We note that at these values of Δ, the ground state of the system would have all atoms on the lower sub-lattice, and the conservation of P_{A-B} indicates that the spin dynamics occurs within a meta-stable manifold with respect to population.

Figure 4b shows the measured resonant decay times τ_s vs. calculated h/J_{ex} for different V_{xy} and Δ, with $\delta_\sigma = 0$ and Δ chosen to be larger than U but considerably less than the next excited band. The decay time τ_s scales with h/J_{ex} over two orders of magnitude in J_{ex}. The solid gray line through the data is a fit to the expected linear dependence, including a constant rate Γ_0 needed to capture the apparent saturation of τ_s at large h/J_{ex}: $\tau_s = (AJ_{\mathrm{ex}}/h + \Gamma_0)^{-1}$, with $A = 7.8(4)$ and $\Gamma_0^{-1} = 0.57(2)$ s. A quantitative calculation of the decay rate in 2D, including the effects of holes, is extremely challenging. However, the existence of a single energy

scale contributing to the demagnetization in this regime justifies (at a qualitative level) a short-time perturbative treatment, from which we extract $A \approx 2\pi\sqrt{z/2} \approx 9$, in agreement with the experimentally measured value [**?**]. Surprisingly, this result is largely independent of the hole density, which can be attributed to the approximate cancellation of two competing effects of holes: they decrease the rate of superexchange dynamics, but simultaneously open new demagnetization channels through the hole-mediated exchange term in Eqn. (1). The empirically determined timescale Γ_0^{-1} is shorter than the measured times for depopulation of the spin manifold or loss of atoms, and may be related to the non-zero relaxation processes observed outside the $\delta_\sigma = 0$ resonance in Fig. 4a. The mechanism for this off-resonant decay is not clear, but since the initial and final states differ in energy by significantly more than J_{ex} it must arise from energy-nonconserving processes such as noise assisted relaxation or doublon production [155]. Corrections to J_{ex} due to excited band virtual processes [203], which we estimate to be of order 10-20 % at the largest Δ and smallest V_{xy} shown in Fig. 4(b), may partially explain the observed saturation.

7.5   Conclusion

The scaling and resonant behavior of the fast and slow relaxation processes clearly reveal their origin as first-order tunneling and superexchange, respectively. For $\Delta \gg J$, our experiment realizes an unusual situation where tunneling, which is only active within a given sublattice, is comparable in strength to the superexchange coupling. This feature—which is crucial to our ability to observe superexchange

dominated dynamics—may have interesting implications for the equilibration of a doped antiferromagnetic state, since it determines the extent to which entropy (initially introduced in the motional degrees of freedom) is shared by the spin degrees of freedom. For smaller but non-zero Δ, the ability to observe both tunneling and superexchange, often simultaneously and at experimentally accessible entropies, opens exciting opportunities to explore the nonequilibrium interplay of spin-exchange and motion. Understanding the detailed dynamics of this strongly-correlated, 2D quantum system is a formidable challenge, which may require the development of new theoretical techniques.

7.6   Methods

7.6.1   Experimental Sequence

All experiments begin with a ^{87}Rb BEC with no discernible thermal fraction in the $|F = 1, m_F = -1\rangle$ internal Zeeman state, optically trapped with trap frequencies $\{\nu_x, \nu_y, \nu_z\} = \{12, 40, 100\}$ Hz. Control of the atom number, independent of trap parameters, is achieved by microwave removal of a fraction of atoms before the final stage of cooling. The BEC is then adiabatically loaded into a deep (≈ 30 E$_r$) 3D $\lambda/2$-spaced lattice with $\lambda =$813 nm, by loading the vertical lattice in 200 ms and the 2D lattice in 100 ms, starting 100 ms after beginning the vertical lattice ramp. The absence of doubly occupied sites is verified by number resolved microwave spectroscopy [187] of the magnetically insensitive $|1, -1\rangle \rightarrow |2, 1\rangle$ clock-transition near 0.323 mT using 80 ms pulses.

Spectroscopic estimates of the total average trap inhomogeneity were made by measuring the broadening of the clock transition and the state-dependent addressing transition ($|1, -1\rangle \rightarrow |2, -2\rangle$). These measurements indicate scalar and vector light shift inhomogeneity over the ≈ 10 μm atom cloud is less than a percent of the total shift, about 800 Hz and 250 Hz respectively. Since Δ and δ_σ are only sensitive to light shift differences on the small length scale of $\lambda/2$, we expect the inhomogeneity in A-B offsets to be substantially smaller than the measured globally averaged inhomogeneity.

We measure the average number of holes throughout the atom cloud by performing number resolved microwave spectroscopy [187] after merging neighboring pairs of sites into one site. Any pair of sites that contains a hole is counted as having one atom, and comparing the merged two-atom signal to the merged one-atom signal gives a measure of the average hole density. We estimate the central hole density by assuming a Fermi-Dirac distribution in the harmonic trap (under the assumption that there are no doubly occupied sites and the system is in thermal equilibrium) having a chemical potential and temperature that matches the measured number and average merged one atom fraction.

7.6.2 Tight Binding Parameters

While this chapter was written in collaboration with the coauthors listed in [10], I would especially like to thank Michael Foss-Feig for his contributions to the following lattice parameters and lattice timescale extraction sections.

Table 7.1: Tilted spin ordering experimental sequence

Step	Time
Load $\lambda/2$ lattice 30 E_r (load vertical lattice $30E_{rvert}$)	100ms(200ms)
apply site selective tilt (26 kHz $\|1,-1\rangle \to \|2,-2\rangle$)	466μs
apply site selective microwave shelving sweep to A sites $\|1,-1\rangle \to \|2,-2\rangle$	300 μs
apply microwave sweeps to B sites $\|1,-1\rangle \to \|2,0\rangle$ then $\|2,0\rangle \to \|1,1\rangle$	2.3 ms 300 μs
apply site selective microwave unshelving sweep to A sites $\|2,-2\rangle \to \|1,-1\rangle$	1.357 ms
un- tilt lattice	466μs
move 2D PC from B sites to A sites	200 μs
apply state independent tilt to A sites	200 μs
quench lattice depth $\approx 5E_r$	200 μs

The tight binding parameters U, J, Δ and δ_σ are determined from an experimentally calibrated model of the 2D lattice potential. The details of the checkerboard optical lattice are described in Ref. [189], and we only give a brief description here relevant for extracting tight binding parameters. The lattice is generated from a single laser beam folded to produce four interfering beams propagating along the x and y directions, resulting in a position-dependent total field

$$\vec{E}_{\text{latt}}(x,y) \;\; = \;\; (E_1\hat{e}_1 e^{-ikx} + E_2\hat{e}_2 e^{-iky} + E_3\hat{e}_3 e^{iky} + E_4\hat{e}_4 e^{ikx}), \qquad (7.3)$$

where $k = 2\pi/\lambda$, $\lambda = 813$ nm is the wavelength of the lattice light, and E_i are the single beam field amplitudes. The orientation and phase of the complex unit vectors $\hat{e}_i$ are controlled with electro-optic modulators (EOMs). The local intensity $I_{\text{latt}} = c\epsilon_0 |\vec{E}_{\text{latt}}|^2$ and circular polarization $i(\vec{E}_{\text{latt}}^* \times \vec{E}_{\text{latt}})$ give rise to a scalar light shift potential $V_{\text{latt}}(x,y)$ and effective Zeeman field $\vec{B}_{\text{eff}}(x,y)$ respectively [223]. The

Table 7.2:   Tilted spin ordering experimental sequence pt.2

Step	Time
hold for tunneling dynamics	2 μs-1 s
quench lattice depth $30E_r$	200 μs
remove state independent tilt from A sites	200 μs
move 2D PC from A sites to B sites	200 μs
apply site selective tilt (26 kHz $|1, -1\rangle \rightarrow |2, -2\rangle$)	200μs
apply site selective microwave sweep $|1, -1\rangle \rightarrow |2, -2\rangle$ on A sites	300 μs
apply site selective microwave sweep $|1, 1\rangle \rightarrow |2, 2\rangle$ on A sites	300 μs
un- tilt lattice	466μs
band-map	300 μs
Stern-Gerlach	3.5 ms

lattice can be tuned between a square lattice with $\lambda/2$ periodicity along x and y, and a square lattice with $\lambda/\sqrt{2}$ periodicity along $x + y$ and $x - y$. The spin-dependent lattice potential is calibrated for our geometry using the measured transmission losses, the calibrated polarization responses of the EOMs (including hysteresis), the measured deviation from orthogonality of the beams along x and y, microwave spectroscopy [190], diffraction phase winding measurements [189, 191] and pulsed diffraction to calibrate the depth [224]. The input field is calibrated in terms of the measured lattice depth $E_1 = (1/2)\sqrt{(V_{xy}/E_\mathrm{R})}$, where the lattice depth in recoil units V_{xy}/E_R is determined for the configuration of a square $\lambda/2$ lattice.

The full lattice potential, including imperfections, is used in the calculation of Bose-Hubbard parameters described below, but the approach we take is simplest to describe without lattice imperfections. In the absence of transmission losses or

birefringence ($E_i = E_{xy}$), the scalar part can be written as

$$V_{\text{latt}}(x,y) = V_{\parallel}(\theta_1)\left(\cos 2kx + \cos 2ky\right) + V_{\perp}(\theta_1)\left[\cos\left(kx - \theta_2\right) + \cos ky\right]^2. \quad (7.4)$$

Here θ_1 and θ_2 are controlled by two separate EOM's, and $V_{\parallel}(\theta_1) = V_{xy}(1/2)\cos^2\theta_1$ and $V_{\perp}(\theta_1) = V_{xy}\sin^2\theta_1$ are parameterized by V_{xy} determined when $\theta_1 = 0$. (For $\theta_1 = \pi/2$, the total lattice depth would be $4V_{xy}$.) In the limit of small θ_1, $V_{\perp} \ll V_{\parallel}$. If in addition $\theta_2 = 0$ or π, the lattice can be described as a square lattice of spacing $\lambda/2$ with a staggered offset $\Delta \approx 4V_{xy}\sin^2\theta_1$ (Fig. 7.5a). We use experimentally measured values of Δ under different conditions to calibrate the lattice model and the dependence of Δ on $\{V_{xy}, \theta_1, \theta_2\}$. The effective field $\vec{B}_{\text{eff}}(x,y)$ lies in the xy plane and is similarly controlled by θ_1 and θ_2. In the presence of a large bias field $\vec{B}_0 \gg \vec{B}_{\text{eft}}$, the total spin-dependent staggered offset $\delta_\sigma \propto |\vec{B}_0 + \vec{B}_{\text{eff}}|$ depends on the relative angle between $\vec{B}_0$ and $\vec{B}_{\text{eff}}$:

$$\left|\vec{B}_0 + \vec{B}_{\text{eff}}(x,y)\right| \approx \left|\vec{B}_0\right| + \vec{B}_{\text{eff}}(x,y) \cdot \left(\frac{\vec{B}_0}{\left|\vec{B}_0\right|}\right). \quad (7.5)$$

We control the size of the spin-dependent shift δ_σ by changing the orientation of $\vec{B}_0$ with respect to the lattice, so that $\delta_\sigma \approx 0$ when $\vec{B}_0 \perp \vec{B}_{\text{eff}}$. Microwave spectroscopy is used to calibrate δ_σ as a function of $\{V_{xy}, \theta_1, \theta_2, \vec{B}_0\}$.

The tunneling parameter J is extracted from band structure calculations based on the full lattice potential. Except in the limit when $\theta_1 = 0$, the potential is not separable in Cartesian coordinates and the band structure calculations must be
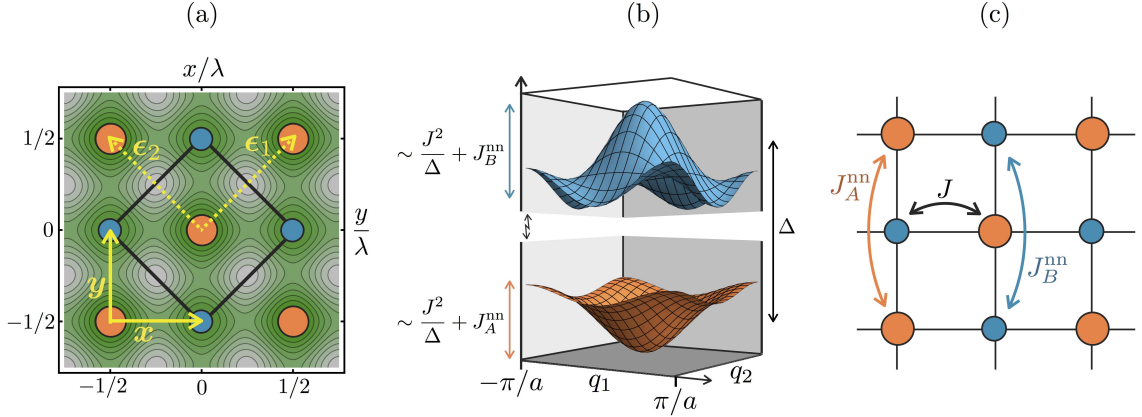
Figure 7.5: (a) The 2D optical lattice potential used for dynamics experiments, showing a unit cell outlined in black. (b) Typical example of the lowest two bands of the lattice (in the limit $\Delta \gg J$) in the first Brillouin zone, which is reciprocal to the unit cell drawn in (a). (c) Lattice sites divided into two sub lattices, and examples of the matrix elements entering the tight-binding model used to calculate the band structure in 7.6.

carried out in 2D. The primitive unit cell of our lattice, shown in Fig. 7.5a, is spanned by primitive vectors $\boldsymbol{\epsilon}_1$ and $\boldsymbol{\epsilon}_2$ of length $a = \lambda/\sqrt{2}$. A typical example of the lowest two bands, $E_-(\boldsymbol{q})$ and $E_+(\boldsymbol{q})$ (where $\boldsymbol{q} = \{q_1, q_2\}$ has components conjugate to $\boldsymbol{\epsilon}_1$ and $\boldsymbol{\epsilon}_2$), is shown in Fig. 7.5b. In order to determine the inter-sublattice tunneling matrix elements, we first calculate the lowest two bands of a suitable two-band tight-binding model analytically.

In the limit $\Delta \gg J$, the bandwidth contribution to either of the lowest two bands from the direct hopping J can be estimated perturbatively as $\sim J^2/\Delta$, which scales with V_{xy} similarly to the next-nearest-neighbor tunneling amplitudes directly connecting sites of the $A(B)$ sublattice, denoted $J_{A(B)}^{\mathrm{nn}}$ (Fig. 7.5c). As a result, an accurate tight binding model must include J_A^{nn} and J_B^{nn}, in which case we find tight

156

binding bands

$$\mathcal{E}_{\pm}(\boldsymbol{q} : \Delta, J, J_A^{\mathrm{nn}}, J_B^{\mathrm{nn}}) = \Delta/2 \qquad\qquad -2(J_A^{\mathrm{nn}} + J_B^{\mathrm{nn}}) \cos q_1 a \cos q_2 a$$

$$\pm \left(\left(\Delta/2 - 2(J_A^{\mathrm{nn}} - J_B^{\mathrm{nn}}) \cos q_1 a \cos q_2 a \right)^2 \right.$$

$$\left. + 4J^2 \left(1 + \cos q_1 a + \cos q_2 a + \cos q_1 a \cos q_2 a \right) \right)^{1/2}. \tag{7.6}$$

We extract the dependence of J on $\{V_{xy}, \theta_1, \theta_2\}$ by fitting $\mathcal{E}_{\pm}(\boldsymbol{q} : \Delta, J, J_A^{\mathrm{nn}}, J_B^{\mathrm{nn}})$ to the numerically calculated $E_{\pm}(\boldsymbol{q}, V_{xy}, \theta_1, \theta_2)$. With the next-nearest-neighbor tunnelings included, the fits typically produce a Brillouin zone averaged fractional error in the band energies on the order of 10^{-3}. Under almost all conditions in the paper, the extracted J is essentially independent of Δ and can be determined from the $\Delta = 0$ lattice with equivalent depth V_{xy}. The interaction energy U is given by $U = g \int d^3r \, |\phi(\boldsymbol{r})|^4$ where $g = 4\pi\hbar^2 a_s/m$, a_s is the s-wave scattering length, m is mass of ^{87}Rb, and $\phi(\boldsymbol{r})$ is the localized Wannier function on a lattice site. Assuming ϕ is a gaussian wave function (appropriate for a harmonic expansion of the lattice site), $U = g/((2\pi)^{3/2} a_x a_y a_z)$ where $a_{x,y,z}$ are the harmonic oscillator lengths associated with the local lattice site curvature. The anharmonicity on a lattice site in a square $\Delta = 0$ lattice can be approximately accounted for by using a Gaussian wave function with a modified width of $a_x = (\lambda/2\pi)/\sqrt{\sqrt{V_{xy}} - 1/2}$. A calculation of J_{ex} that takes into account the $\Delta \neq 0$ impact on U deviates by less than 6 % from the $\Delta = 0$ value over the range of Δ considered here, and we use the simple $\Delta = 0$ analytical expression for U described above.

7.6.3 Superexchange Timescale Estimates

When $|U - \Delta| \gg J$, (and assuming that $\delta_\sigma \ll \Delta$), double occupancies are forbidden and the Bose-Hubbard model can be mapped onto a bosonic t-J model with a sub-lattice detuning,

$$
\begin{aligned}
H = -J \sum_{\langle i,j \rangle,\sigma} a_{i\sigma}^\dagger a_{j\sigma} - \sum_{j \in A,\sigma} \Delta_\sigma a_{j\sigma}^\dagger a_{j\sigma} \\
- J_{\text{ex}} \sum_{\langle i,j \rangle} \boldsymbol{S}_i \cdot \boldsymbol{S}_j - \sum_{\langle i,j,k \rangle,\sigma\sigma'} V_j \left(a_{i\sigma}^\dagger \boldsymbol{\tau}_{\sigma\sigma'} a_{k\sigma'} \right) \cdot \boldsymbol{S}_j \\
- \frac{3}{2} \sum_{\langle i,j,k \rangle,\sigma} V_j a_{i\sigma}^\dagger a_{k\sigma} n_j.
\end{aligned}
\tag{7.7}
$$

Here

$$
J_{\text{ex}} = \frac{4J^2 U}{U^2 - \Delta^2} \qquad V_j = \frac{J^2}{U - \kappa_j \Delta},
\tag{7.8}
$$

and $\kappa_j = +1$ or $\kappa_j = -1$ depending on whether j is contained in the A or B sub lattice, respectively. For all of the data in Fig. 4 of the manuscript, $\Delta \gg J$. As a result, terms which change the sub lattice population (i.e. the remaining hopping processes which move a single atom between two adjacent and otherwise empty lattice sites) can also be integrated out at second order in the small parameter J/Δ,

yielding

$$H = -J_{\text{ex}} \sum_{\langle i,j \rangle} \boldsymbol{S}_i \cdot \boldsymbol{S}_j - \sum_{\langle i,j,k \rangle, \sigma\sigma'} \tilde{V}_j \left(a_{i\sigma}^\dagger \boldsymbol{\tau}_{\sigma\sigma'} a_{k\sigma'} \right) \cdot \boldsymbol{S}_j$$
$$- \frac{3}{2} \sum_{\langle i,j,k \rangle, \sigma} \tilde{V}_j a_{i\sigma}^\dagger a_{k\sigma} n_j + \sum_{\langle i,j,k \rangle, \sigma} \frac{J^2}{\kappa_j \Delta} a_{i\sigma}^\dagger a_{k\sigma}. \tag{7.9}$$

Here $\tilde{V}_j = J^2/(U - \kappa_j \Delta) + J^2/(\kappa_j \Delta)$ is modified from the previously defined V_j to account for second order hole motion consistent with the hardcore constraint. We note that the first two terms couple states with different sub lattice magnetization, while the second two do not.

A priori, for a finite hole density (i.e. when the demagnetization channel associated with the second term in 7.9 is active), the demagnetization rate at short times does not need to scale with J_{ex}. However, we find that over a broad range of densities, the short-time demagnetization rate does indeed scale with J_{ex} to a good approximation, as we now show. Because the initial state is an eigenstate of the staggered magnetization operator

$$\hat{M}_s = 2 \left(\sum_{j \in A} S_j^z - \sum_{j \in B} S_j^z \right)/N, \tag{7.10}$$

with N the total number of atoms, the initial decay of the magnetization must be quadratic in time. Defining $M_s(t) = \langle \psi(t) | \hat{M}_s | \psi(t) \rangle$, we can choose to expand the magnetization as $M_s(t) = \exp[-m_2 t^2 + \mathcal{O}(t^3)]$, where

$$m_2 = \frac{1}{2} \langle [H, [H, \hat{M}_s]] \rangle / \hbar^2. \tag{7.11}$$

159
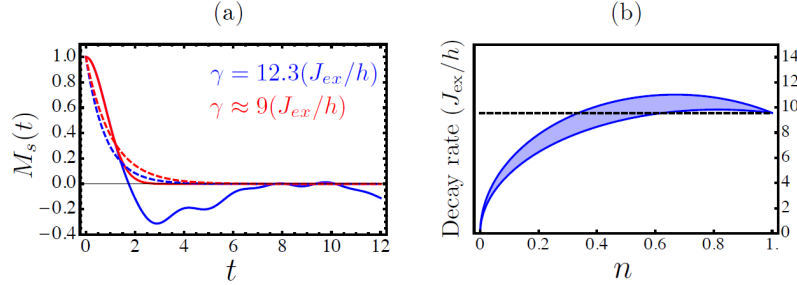
Figure 7.6: (a) Demagnitezation dynamics from a unit-filled Neél state. The blue solid line is from exact diagonalization of a 4×4 plaquette with periodic boundary conditions, and the blue dotted line is a fit to an exponential $e^{-\gamma t}$. The red solid line is from perturbation theory, and the red dotted line is once again a fit to an exponential (this procedure gives the slope of the gray line plotted in Fig. 4b). (b) Demagnetization rate calculated at second-order in short-time perturbation theory, as a function of density. The blue shaded region reflects a range of the ratio $1 < \Delta/U < 5$, which encompasses all data points shown in Fig. 4 of the manuscript, while the black-dashed line shows the superexchange time-scale at unit filling.

Working to second order, we then extract a time-scale by fitting $e^{-m_2 t^2}$ to an exponential $e^{-\gamma t}$, giving $\gamma \approx \sqrt{m_2}$. This approximation is only expected to give a qualitative estimate of the decay time scale, valid under the assumption that a significant portion of the decay occurs at or below the timescale $\hbar/J_{\text{ex}}$. However, this estimate is fairly accurate when compared to exact diagonalization results for a superexchange model on a 4×4 plaquette (see Fig. 7.6a).

Under the assumption that holes are distributed randomly, extensive but straightforward algebra leads to

$$\gamma \approx \frac{1}{\hbar} \sqrt{\frac{nz}{2} \times J_{\text{ex}}^2 + 2n(1-n)z(z-1) \times \left((\tilde{V}_+)^2 + (\tilde{V}_-)^2 \right)}, \qquad (7.12)$$

where n is the density, $z = 4$ is the lattice coordination number, and $\tilde{V}_+(\tilde{V}_-)$ is equal to $\tilde{V}_j$ when j is contained in the $B(A)$ sub lattice. This result is plotted (in units of J_{ex}/h) for a range of values of U/Δ in Fig. 7.6b, where we see that for a broad range of densities $(n \gtrsim 0.3)$ the rate is in good quantitative agreement with the one extracted at unit filling $\left(\gamma \approx (J_{\text{ex}}/\hbar)\sqrt{z/2}\text{, dashed line}\right)$, where J_{ex} is the only relevant energy scale in the Hamiltonian.

7.6.4   The $\Delta = U$ population imbalance resonance

When $U \gg J$ and the staggered offset is near $\Delta = U$, all dynamics occurs within the subspace where the A sub lattice has either one or two atoms on each site, while every site of the B sub lattice has either one or zero atoms. If, for simplicity, we ignore the spin degrees of freedom, and consider doubly occupied A sites to be particles and singly occupied A sites to be holes, the density degrees of freedom map onto hardcore spinless bosons hopping with strength J,

$$H_{\text{res}} = -J\sum_{\langle i,j \rangle} b_i^\dagger b_j + \tilde{\Delta}\sum_{j\in A} b_j^\dagger b_j. \tag{7.13}$$

Here the operator b $(b^\dagger)$ annihilates (creates) a hardcore boson, the sub lattice offset is related to the actually staggered offset by $\tilde{\Delta} = U - \Delta$, and the initial state contains a single boson on every site of the B sub lattice and none on the A sub lattice. Note that the tunneling energy for the hardcore bosons in this model is ambiguous up to a factor of $\sqrt{2}$, since the matrix element for an atom to hop from the B to the A sub lattice depends on whether the "hole" on the A sub lattice has

the same spin as the hopping particle. Assuming a translationally invariant lattice with $\mathcal{N}$ sites, the average hardcore boson density on the $A(B)$ sub lattice is given by $\tilde{n}_{A(B)} = (2/\mathcal{N}) \sum_{j \in A(B)} \langle b_j^\dagger b_j \rangle$. The tilde in $\tilde{n}_{A(B)}$ indicates that these are not the densities of the physical atoms, which we denote by n_A and n_B, and are related by $n_A = \tilde{n}_A + 1$ and $n_B = \tilde{n}_B$. At unit filling $(n_A + n_B = 2)$, the experimentally-measured population difference, $P_{A-B}(t) = \frac{1}{2}[n_A(t) - n_B(t)]$, can be expressed as $P_{A-B}(t) = 1 - n_B(t) = 1 - \tilde{n}_B(t)$. As described above, the initial state in the hardcore boson picture has $\tilde{n}_B(0) = 1$, and hence $P_{A-B}(0) = 0$. The steady-state (at $\tilde{\Delta} = 0$, i.e. on resonance) must have $\tilde{n}_A = \tilde{n}_B = 1/2$, and hence $P_{A-B} = 1/2$.

The steady-state population imbalance is given by $P_{A-B}^{\text{ss}}(\tilde{\Delta}) = 1 - \tilde{n}_B$ for $t \gg \hbar/J$, and we would like to know how $P_{A-B}^{\text{ss}}(\tilde{\Delta})$ depends on the sub lattice detuning $\tilde{\Delta}$ (this is what is measured experimentally (blue data points) in Fig. 3(b) of the manuscript). A simple estimate can be obtained by just relaxing the hardcore constraint, in which case the problem becomes non-interacting. We can then obtain $\tilde{n}_B(t)$ by solving the dynamics of a single atom starting on the B sub lattice. Working in quasi-momentum space, the single-particle eigenstates in a staggered lattice can be obtained by diagonalizing the matrix

$$\mathcal{H}(\boldsymbol{q}) = \begin{pmatrix} \tilde{\Delta}/2 & \varepsilon(\boldsymbol{q}) \\ \varepsilon(\boldsymbol{q}) & -\tilde{\Delta}/2 \end{pmatrix}, \tag{7.14}$$

where $\varepsilon(\boldsymbol{q}) = 2J(\cos q_x a + \cos q_y a)$ is the single-particle spectrum at zero detuning. Our initial state is evenly distributed across the Brillouin zone, but at every $\boldsymbol{q}$ it

162

will be decomposed differently onto the eigenvectors of the above matrix. Obtaining $\tilde{n}_B(t)$ simply requires solving a standard off-resonant Rabi problem at each $\boldsymbol{q}$, with generalized Rabi frequency $\Omega(\boldsymbol{q}) = \sqrt{\tilde{\Delta}^2 + 4\varepsilon(\boldsymbol{q})^2}$. Integrating such solutions over the first Brillouin zone, we obtain

$$\tilde{n}_B(t) = \frac{1}{A_{\mathrm{bz}}} \int_{\mathrm{bz}} d^2q \frac{\Omega(\boldsymbol{q})^2 + 2\varepsilon(\boldsymbol{q})^2 \left(\cos \Omega(\boldsymbol{q})t - 1\right)}{\Omega(\boldsymbol{q})^2}, \qquad (7.15)$$

where A_{bz} is the first Brillouin zone area. The size of the time-dependent term in this integral decreases at large t as $1/\sqrt{t}$ (as can be seen from a stationary phase approximation), and so only the time-independent piece survives at long time, giving

$$P_{A-B}^{\mathrm{ss}}(\tilde{\Delta}) = \frac{1}{A_{\mathrm{bz}}} \int_{\mathrm{bz}} d^2q \frac{2\varepsilon(\boldsymbol{q})^2}{\Omega(\boldsymbol{q})^2}. \qquad (7.16)$$

Taking the integral numerically, we find that the full-width at half-max of this resonance is approximately $5J$, which is significantly narrower than the experimentally measured feature.

7.6.5 Fractional U sublattice population transfer resonances

In addition to first order tunneling resonance, we also observe two second order resonances at $\Delta = U/2$ and $\Delta = 3U/2$. These resonances are shown in fig. 7.7. The resonance at $\Delta = U/2$ can be understood by considering three sites, where two occupied sites in the high energy sublattice neighboring an unoccupied site in the low energy sublattice. The two particles may tunnel to the lower sublattice

163
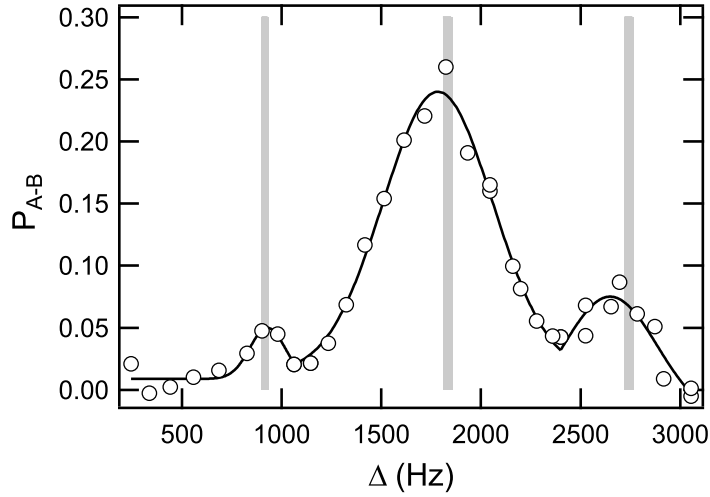
Figure 7.7: Fractional U tunneling resonances, the gray bands are the calculated values of $\Delta = U/2, U, 3U/2$.

but conserve energy because of the on-site interaction. Likewise, the resonance at

$\Delta = 3U/2$ can be understood by considering three sites, where two occupied sites in

the high energy sublattice neighboring an occupied site in the low energy sublattice.

The two particles may tunnel to the lower sublattice but conserve energy with a

larger applied offset because there are not 3 units of on-site interaction.

Chapter 8: Conclusion and Outlook

We have discussed three distinct projects. At the present time two of the three projects have ended, nevertheless we believe there are still many paths forward for each topic.

In the atomic spectroscopy project we identified and quantified a systematic effect common to transitions with unresolvable structure. Its application to atomic lithium represents a sweet spot in research where the required technology is widely available and the resolution of the discrepancy has impacts on both electronic structure calculations and determinations of nuclear charge radii. In the future it, this analysis can applied more systems including excited states, more fundamental and technically demanding H, as well as, to other widely studied species such as K.

While investigating excited-to-excited state transitions for laser cooling we demonstrated multiphoton cooling and trapping processes and proposed a dressed dissipative lattice for the cooling of H. One immediate extension of this work would be to further investigate the sub-Doppler temperatures and cooling processes observed in Cesium. More generally, we hope that some variant of these techniques finds applicability in quantum gas research. Perhaps a natural context for this would be in Rydberg atoms with a two photon excitation process. While the long

lifetime of Rydberg states would impede traditional cooling, we have demonstrated that the highest excited (Rydberg) state may be adiabatically eliminated. Thinking about this also led to ideas to use the D1 transition to subDoppler cool atoms with unresovable hyperfine structure such as Li and K.

Finally, the program of quantum emulation/simulation is likely to continue for the foreseeable future, due to both the diversity of the field and the fundamental difficulty of the underlying manybody problem. Using ultracold atoms in a state-dependent checkerboard optical lattice, we were able to prepare and readout staggered magnetic order. Critically, we were also able to tune the strength of nearest neighbor superexchange interactions in an extended system. This enabled us to observe dynamics governed by either tunneling or superexchange. It will be very exciting to observe the competition of these energy scales in a controlled setting as these mechanisms are believed give rise to pairing in cuprate superconductors. It would also be interesting to add microwave dressing control over the superexchange energy scales to realize a controllable XXZ Heisenberg model.

The two main experimental avenues of searching for emergent quantum phenomena are engineering more exotic single particle states and realizing long range interactions. Currently, lattices of optical flux represent one of the most exciting paths in optical potential control of ultracold atoms. On the interaction side Superexchange can be optimized by using light atoms (eg. Li) to achieve a larger J tunneling energy scale, while maintaining tunability with a double well lattice (the lattice for Li cannot be state-dependent b/c the detuning implied by the fine-structure splitting would limit the lifetime). There are a number of other paths to-

wards long range interactions including: Feshbach resonance, mixtures of ultracold atoms where one species could be used to mediate longrange interactions between the other, Rydberg state dressing, atoms with permanent magnetic moments (such as Cr, Er, and Dy), polar molecules with permanent electric dipole moments (such as RbK and the promising endothermic NaK), and BEC in optical cavities creating effectively infinite range interactions. Going forward it will be exciting to see how rapidly these approaches are implemented in order to realize progressively more exotic quantum states and dynamics.

Bibliography

[1] H. C. Urey, F. G. Brickwedde, and G. M. Murphy, "A Hydrogen Isotope of Mass 2," Phys. Rev. **39**, 164–165 (1932).
http://link.aps.org/doi/10.1103/PhysRev.39.164
(Cited on page 1.)

[2] R. Pohl et al., "The size of the proton," Nature **466**, 213–216 (2010).
http://www.nature.com/nature/journal/v466/n7303/abs/nature09250.html
(Cited on pages 1 and 17.)

[3] C. J. Sansonetti, C. E. Simien, J. D. Gillaspy, J. N. Tan, S. M. Brewer, R. C. Brown, S. Wu, and J. V. Porto, "Absolute Transition Frequencies and Quantum Interference in a Frequency Comb Based Measurement of the ^{6,7}Li D Lines," Phys. Rev. Lett. **107**, 023 001 (2011).
http://link.aps.org/doi/10.1103/PhysRevLett.107.023001
(Cited on pages 2, 7, 8, 13, 18, 19, 23, 24, 26, 27, 28, 30, and 31.)

[4] C. J. Sansonetti, C. E. Simien, J. D. Gillaspy, J. N. Tan, S. M. Brewer, R. C. Brown, S. Wu, and J. V. , "Absolute Transition Frequencies and Quantum Interference in a Frequency Comb Based Measurement of the ^{6,7}Li D Lines," Phys. Rev. Lett. **109**, 023 001 (2012).
http://link.aps.org/doi/10.1103/PhysRevLett.107.023001
(Cited on pages 2, 7, 8, 13, 18, 23, 24, 26, 27, 28, 30, and 31.)

[5] R. C. Brown, S. Wu, J. V. Porto, C. J. Sansonetti, C. E. Simien, S. M. Brewer, J. N. Tan, and J. D. Gillaspy, "Quantum interference and light polarization effects in unresolvable atomic lines: Application to a precise measurement of the ^{6,7}Li D_2 lines," Phys. Rev. A **87**, 032 504 (2013).
http://link.aps.org/doi/10.1103/PhysRevA.87.032504
(Cited on pages 2 and 7.)

[6] R. C. Brown, S. Wu, J. V. Porto, C. J. Sansonetti, C. E. Simien, S. M. Brewer, J. N. Tan, and J. D. Gillaspy, "Erratum: Quantum interference and light polarization effects in unresolvable atomic lines: Application to a precise

measurement of the ^{6,7}Li D_2 lines [Phys. Rev. A **87**, 032504 (2013)]," Phys. Rev. A **88**, 069 902 (2013).
http://link.aps.org/doi/10.1103/PhysRevA.88.069902
(Cited on pages 2 and 7.)

[7] S. Wu, T. Plisson, R. C. Brown, W. D. Phillips, and J. V. Porto, "Multiphoton Magnetooptical Trap," Phys. Rev. Lett. **103**, 173 003 (2009).
http://link.aps.org/doi/10.1103/PhysRevLett.103.173003
(Cited on pages 3, 38, and 46.)

[8] S. Wu, R. C. Brown, W. D. Phillips, and J. V. Porto, "Pulsed Sisyphus Scheme for Laser Cooling of Atomic (Anti)Hydrogen," Phys. Rev. Lett. **106**, 213 001 (2011).
http://link.aps.org/doi/10.1103/PhysRevLett.106.213001
(Cited on pages 3 and 38.)

[9] R. C. Brown, S. Olmschenk, S. Wu, A. M. Dyckovsky, R. Wyllie, and J. V. Porto, "Note: Pneumatically actuated and kinematically positioned optical mounts compatible with laser-cooling experiments," Review of Scientific Instruments **84**, – (2013).
http://scitation.aip.org/content/aip/journal/rsi/84/9/10.1063/1.4819744
(Cited on pages 5 and 75.)

[10] R. C. Brown, R. Wyllie, S. B. Koller, E. A. Goldschmidt, M. Foss-Feig, and J. V. Porto, "2D Superexchange mediated magnetization dynamics in an optical lattice," ArXiv e-prints (2014).
(Cited on pages 5, 138, and 152.)

[11] A. L. Schawlow, "Spectroscopy in a New Light," Science **217**, 9–16 (1982).
http://www.sciencemag.org/content/217/4554/9.short
(Cited on page 6.)

[12] W. Demtroder, *Laser spectroscopy : basic concepts and instrumentation 3rd Ed.* (Springer-Verlag, Berlin ; New York :, 2003).
(Cited on pages 6 and 14.)

[13] Z.-C. Yan and G. W. F. Drake, "Lithium isotope shifts as a measure of nuclear size," Phys. Rev. A **61**, 022 504 (2000).
http://link.aps.org/doi/10.1103/PhysRevA.61.022504
(Cited on pages 6 and 28.)

[14] C. J. Sansonetti, B. Richou, R. Engleman, and L. J. Radziemski, "Measurements of the resonance lines of ^{6}Li and ^{7}Li by Doppler-free frequency-modulation spectroscopy," Phys. Rev. A **52**, 2682–2688 (1995).
http://link.aps.org/doi/10.1103/PhysRevA.52.2682
(Cited on pages 6, 18, and 28.)

169

[15] W. Scherf, O. Khait, H. Jger, and L. Windholz, "Re-measurement of the transition frequencies, fine structure splitting and isotope shift of the resonance lines of lithium, sodium and potassium," Z. Phys. D-Atom Mol. Cl. **36**, 31–33 (1996).
http://dx.doi.org/10.1007/BF01437417
(Cited on pages 6, 18, and 28.)

[16] J. Walls, R. Ashby, J. Clarke, B. Lu, and W. van Wijngaarden, "Measurement of isotope shifts, fine and hyperfine structure splittings of the lithium D lines," Eur. Phys. J. D **22**, 159–162 (2003).
http://dx.doi.org/10.1140/epjd/e2003-00001-5
(Cited on pages 6, 18, 28, and 30.)

[17] G. A. Noble, B. E. Schultz, H. Ming, and W. A. van Wijngaarden, "Isotope shifts and fine structures of ^{6,7}Li D lines and determination of the relative nuclear charge radius," Phys. Rev. A **74**, 012 502 (2006).
http://link.aps.org/doi/10.1103/PhysRevA.74.012502
(Cited on pages 6, 18, 28, and 30.)

[18] D. Das and V. Natarajan, "Absolute frequency measurement of the lithium D lines: Precise determination of isotope shifts and fine-structure intervals," Phys. Rev. A **75**, 052 508 (2007).
http://link.aps.org/doi/10.1103/PhysRevA.75.052508
(Cited on pages 6, 28, and 30.)

[19] Y.-H. Lien, K.-J. Lo, H.-C. Chen, J.-R. Chen, J.-Y. Tian, J.-T. Shy, and Y.-W. Liu, "Absolute frequencies of the ^{6,7}Li 2S ^{2}S$_{1/2}$ → **3**S $^2S_{1/2}$ transitions," Phys. Rev. A **84**, 042 511 (2011).
http://link.aps.org/doi/10.1103/PhysRevA.84.042511
(Cited on pages 6 and 28.)

[20] R. Sánchez, M. Žáková, Z. Andjelkovic, B. A. Bushaw, K. Dasgupta, G. Ewald, C. Geppert, H.-J. Kluge, J. Krämer, M. Nothhelfer, D. Tiedemann, D. F. A. Winters, and W. Nörtershäuser, "Absolute frequency measurements on the 2S-3S transition of lithium-6,7," New Journal of Physics **11**, 073 016 (2009).
http://stacks.iop.org/1367-2630/11/i=7/a=073016
(Cited on pages 6 and 28.)

[21] B. A. Bushaw, W. Nörtershäuser, G. Ewald, A. Dax, and G. W. F. Drake, "Hyperfine Splitting, Isotope Shift, and Level Energy of the 3S States of ^{6,7}Li," Phys. Rev. Lett. **91**, 043 004 (2003).
http://link.aps.org/doi/10.1103/PhysRevLett.91.043004
(Cited on pages 6 and 28.)

[22] G. Ewald, W. Nörtershäuser, A. Dax, S. Götte, R. Kirchner, H.-J. Kluge, T. Kühl, R. Sanchez, A. Wojtaszek, B. A. Bushaw, G. W. F. Drake, Z.-C. Yan, and C. Zimmermann, "Nuclear Charge Radii of ^{8,9}Li Determined by

Laser Spectroscopy," Phys. Rev. Lett. **93**, 113 002 (2004).
http://link.aps.org/doi/10.1103/PhysRevLett.93.113002
(Cited on pages 6 and 28.)

[23] W. Nörtershäuser, R. Sánchez, G. Ewald, A. Dax, J. Behr, P. Bricault, B. A. Bushaw, J. Dilling, M. Dombsky, G. W. F. Drake, S. Götte, H.-J. Kluge, T. Kühl, J. Lassen, C. D. P. Levy, K. Pachucki, M. Pearson, M. Puchalski, A. Wojtaszek, Z.-C. Yan, and C. Zimmermann, "Isotope-shift measurements of stable and short-lived lithium isotopes for nuclear-charge-radii determination," Phys. Rev. A **83**, 012 516 (2011).
http://link.aps.org/doi/10.1103/PhysRevA.83.012516
(Cited on pages 6 and 31.)

[24] Z.-C. Yan, W. Nörtershäuser, and G. W. F. Drake, "High Precision Atomic Theory for Li and Be$^+$: QED Shifts and Isotope Shifts," Phys. Rev. Lett. **100**, 243 002 (2008).
http://link.aps.org/doi/10.1103/PhysRevLett.100.243002
(Cited on pages 6, 27, and 30.)

[25] L. J. LeBlanc and J. H. Thywissen, "Species-specific optical lattices," Phys. Rev. A **75**, 053 612 (2007).
http://link.aps.org/doi/10.1103/PhysRevA.75.053612
(Cited on page 6.)

[26] B. Arora, M. S. Safronova, and C. W. Clark, "Tune-out wavelengths of alkali-metal atoms and their applications," Phys. Rev. A **84**, 043 401 (2011).
http://link.aps.org/doi/10.1103/PhysRevA.84.043401
(Cited on page 6.)

[27] M. S. Safronova, U. I. Safronova, and C. W. Clark, "Magic wavelengths for optical cooling and trapping of lithium," Phys. Rev. A **86**, 042 505 (2012).
http://link.aps.org/doi/10.1103/PhysRevA.86.042505
(Cited on page 6.)

[28] V. Weisskopf and E. Wigner, "Berechnung der natrlichen Linienbreite auf Grund der Diracschen Lichttheorie," Z. Phys. A-Hadron Nuc. **63**, 54–73 (1930).
http://dx.doi.org/10.1007/BF01336768
(Cited on page 7.)

[29] P. A. Franken, "Interference Effects in the Resonance Fluorescence of "Crossed" Excited Atomic States," Phys. Rev. **121**, 508–512 (1961).
http://link.aps.org/doi/10.1103/PhysRev.121.508
(Cited on page 7.)

[30] T. Bergeman, "Intensities, line shifts, and resonance interference in zero-field optical double resonance," J. Chem. Phys. **61**, 4515–4526 (1974).

http://link.aip.org/link/?JCP/61/4515/1
(Cited on page 7.)

[31] R. Walkup, A. L. Migdall, and D. E. Pritchard, "Frequency-dependent polarization of light scattered near the $NaD2$ resonance line," Phys. Rev. A **25**, 3114–3120 (1982).
(Cited on page 7.)

[32] M. Horbatsch and E. A. Hessels, "Shifts from a distant neighboring resonance," Phys. Rev. A **82**, 052 519 (2010).
(Cited on pages 7 and 16.)

[33] K. S. E. Eikema, J. Walz, and T. W. Hänsch, "Continuous Coherent Lyman-α Excitation of Atomic Hydrogen," Phys. Rev. Lett. **86**, 5679–5682 (2001).
http://link.aps.org/doi/10.1103/PhysRevLett.86.5679
(Cited on page 8.)

[34] S. Falke, E. Tiemann, C. Lisdat, H. Schnatz, and G. Grosche, "Transition frequencies of the D lines of ^{39}K , ^{40}K , and ^{41}K measured with a femtosecond laser frequency comb," Phys. Rev. A **74**, 032 503 (2006).
(Cited on pages 8, 18, and 24.)

[35] A. Coc, C. Thibault, F. Touchard, H. Duong, P. Juncar, S. Liberman, J. Pinard, J. Lerm, J. Vialle, S. Bttgenbach, A. Mueller, and A. Pesnelle, "Hyperfine structures and isotope shifts of $^{207-213,220-228}$Fr; Possible evidence of octupolar deformation," Phys. Lett. B **163**, 66 – 70 (1985).
http://www.sciencedirect.com/science/article/pii/0370269385901935
(Cited on page 8.)

[36] M. Žáková, Z. Andjelkovic, M. L. Bissell, K. Blaum, G. W. F. Drake, C. Geppert, M. Kowalska, J. Krämer, A. Krieger, M. Lochmann, T. Neff, R. Neugart, W. Nörtershäuser, R. Sánchez, F. Schmidt-Kaler, D. Tiedemann, Z.-C. Yan, D. T. Yordanov, and C. Zimmermann, "Isotope shift measurements in the 2 s 1/2 2 p 3/2 transition of Be + and extraction of the nuclear charge radii for 7, 10, 11 Be," J. Phys. G - Nucl. Partic. **37**, 055 107 (2010).
http://stacks.iop.org/0954-3899/37/i=5/a=055107
(Cited on page 8.)

[37] C. Sur, B.K. Sahoo, R.K. Chaudhuri, B.P. Das, and D. Mukherjee, "Comparative studies of the magnetic dipole and electric quadrupole hyperfine constants for the ground and low lying excited states of $^{25}Mg^+$," Eur. Phys. J. D **32**, 25–31 (2005).
http://dx.doi.org/10.1140/epjd/e2004-00176-1
(Cited on page 8.)

[38] A. Beyer, C. G. Parthey, N. Kolachevsky, J. Alnis, K. Khabarova, R. Pohl, E. Peters, D. C. Yost, A. Matveev, K. Predehl, S. Droste, T. Wilken,

R. Holzwarth, T. W. Hnsch, M. Abgrall, D. Rovera, C. Salomon, P. Laurent, and T. Udem, "Precision Spectroscopy of Atomic Hydrogen," Journal of Physics: Conference Series **467**, 012 003 (2013).
http://stacks.iop.org/1742-6596/467/i=1/a=012003
(Cited on page 8.)

[39] R. Loudon, *The Quantum Theory of Light* (Oxford University Press, New York, 2000), 3rd ed. edn.
(Cited on pages 8 and 9.)

[40] P. A. M. Dirac, "The Quantum Theory of the Emission and Absorption of Radiation," P. Roy. Soc. Lond. A Mat. **114**, 243–265 (1927).
http://rspa.royalsocietypublishing.org/content/114/767/243.short
(Cited on page 8.)

[41] J. F. Kielkopf, "New approximation to the Voigt function with applications to spectral-line profile analysis," J. Opt. Soc. Am. **63**, 987–995 (1973).
http://www.opticsinfobase.org/abstract.cfm?URI=josa-63-8-987
(Cited on page 11.)

[42] A. Corney, *Atomic and laser spectroscopy* (Oxford, New York, 1977).
(Cited on page 11.)

[43] G. B. Arfken and H.-J. Weber, *Mathematical Methods For Physicists* (Elsevier, New York, 2005), 6 edn.
(Cited on page 13.)

[44] J. S. Deech, R. Luypaert, and G. W. Series, "Determination of lifetimes and hyperfine structures of the 8, 9 and 10 2 D 3/2 states of 133 Cs by quantum-beat spectroscopy," J Phys. B-At. Mol. Opt. **8**, 1406 (1975).
http://stacks.iop.org/0022-3700/8/i=9/a=007
(Cited on page 14.)

[45] A. Marsman, M. Horbatsch, and E. A. Hessels, "Shifts due to distant neighboring resonances for laser measurements of $2\,^3S_1$-to-$2\,^3P_J$ transitions of helium," Phys. Rev. A **86**, 040 501 (2012).
http://link.aps.org/doi/10.1103/PhysRevA.86.040501
(Cited on page 16.)

[46] P. J. Mohr, B. N. Taylor, and D. B. Newell, "CODATA recommended values of the fundamental physical constants: 2006," Rev. Mod. Phys. **80**, 633–730 (2008).
http://link.aps.org/doi/10.1103/RevModPhys.80.633
(Cited on page 17.)

[47] J. Ye, S. Swartz, P. Jungner, and J. L. Hall, "Hyperfine structure and absolute frequency of the 87Rb 5P3/2 state," Opt. Lett. **21**, 1280–1282 (1996).

http://ol.osa.org/abstract.cfm?URI=ol-21-16-1280
(Cited on page 17.)

[48] V. Gerginov, C. E. Tanner, S. Diddams, A. Bartels, and L. Hollberg, "Optical frequency measurements of $6s\,^2S_{1?2}\,\breve{}\,6p\,^2P_{3?2}$ transition in a ^{133}Cs atomic beam using a femtosecond laser frequency comb," Phys. Rev. A **70**, 042 505 (2004).
http://link.aps.org/doi/10.1103/PhysRevA.70.042505
(Cited on page 17.)

[49] C. E. Simien, S. M. Brewer, J. N. Tan, J. D. Gillaspy, and C. J. Sansonetti, "Progress at NIST in measuring the D-lines of Li isotopes using an optical frequency synthesizer," Can. J. Phys. **89**, 59–62 (2011).
http://www.ingentaconnect.com/content/nrc/cjp/2011/00000089/00000001/art00010

(Cited on page 18.)

[50] M. Puchalski and K. Pachucki, "Fine and hyperfine splitting of the $2P$ state in Li and Be$^+$," Phys. Rev. A **79**, 032 510 (2009).
http://link.aps.org/doi/10.1103/PhysRevA.79.032510
(Cited on pages 20, 27, and 30.)

[51] V. A. Yerokhin, "Hyperfine structure of Li and Be$^+$," Phys. Rev. A **78**, 012 513 (2008).
http://link.aps.org/doi/10.1103/PhysRevA.78.012513
(Cited on page 20.)

[52] A. Beckmann, K. D. Böklen, and D. Elke, "Precision measurements of the nuclear magnetic dipole moments," Z. Phys. A-Hadron Nuc. **270**, 173–186 (1974).
(Cited on pages 24, 26, 27, and 28.)

[53] C. Cohen-Tannoudji, J. Dupont-Roc, and G. Grynberg, *Optical Bloch Equations* (Wiley-VCH Verlag GmbH, 2008), pp. 353–405.
http://dx.doi.org/10.1002/9783527617197.ch5
(Cited on page 24.)

[54] S. M. Tan, "A computational toolbox for quantum and atomic optics," J. Opt. B-Quantum S. O. **1**, 424 (1999).
http://stacks.iop.org/1464-4266/1/i=4/a=312
(Cited on page 24.)

[55] K. C. Brog, T. G. Eck, and H. Wieder, "Fine and Hyperfine Structure of the $2\,^2P$ Term of Li^6 and Li^7," Phys. Rev. **153**, 91–103 (1967).
http://link.aps.org/doi/10.1103/PhysRev.153.91
(Cited on page 30.)

[56] H. Orth, H. Ackermann, and E. W. Otten, "Fine and hyperfine structure of the X; term of X Li; determination of the nuclear quadrupole moment," Z.

Phys. A-Hadron Nuc. **273**, 221–232 (1975).
http://dx.doi.org/10.1007/BF01410002
(Cited on page 30.)

[57] C. D. Jager, H. D. Vries, and C. D. Vries, "Nuclear charge- and magnetization-density-distribution parameters from elastic electron scattering," Atom. Data Nucl. Data **14**, 479 – 508 (1974).
http://www.sciencedirect.com/science/article/pii/S0092640X74800021
(Cited on pages 28 and 31.)

[58] E. Riis, A. G. Sinclair, O. Poulsen, G. W. F. Drake, W. R. C. Rowley, and A. P. Levick, "Lamb shifts and hyperfine structure in ^{6}Li$^+$ and ^{7}Li$^+$: Theory and experiment," Phys. Rev. A **49**, 207–220 (1994).
http://link.aps.org/doi/10.1103/PhysRevA.49.207
(Cited on pages 28 and 31.)

[59] K. Pachucki, Private Communication (2012).
(Cited on page 31.)

[60] Z. Lin, K. Shimizu, M. Zhan, F. Shimizu, and H. Takuma, "Laser Cooling and Trapping of Li," Japanese Journal of Applied Physics **30**, L1324–L1326 (1991).
http://jjap.jsap.jp/link?JJAP/30/L1324/
(Cited on page 38.)

[61] E. L. Raab, M. Prentiss, A. Cable, S. Chu, and D. E. Pritchard, "Trapping of Neutral Sodium Atoms with Radiation Pressure," Phys. Rev. Lett. **59**, 2631–2634 (1987).
http://link.aps.org/doi/10.1103/PhysRevLett.59.2631
(Cited on pages 38 and 45.)

[62] R. S. Williamson and T. Walker, "Magneto-optical trapping and ultracold collisions of potassium atoms," J. Opt. Soc. Am. B **12**, 1393–1397 (1995).
http://josab.osa.org/abstract.cfm?URI=josab-12-8-1393
(Cited on page 38.)

[63] T. Walker, D. Hoffmann, P. Feng, and R. W. III, "A vortex-force atom trap," Physics Letters A **163**, 309 – 312 (1992).
http://www.sciencedirect.com/science/article/pii/037596019291017L
(Cited on page 38.)

[64] D. Sesko, T. Walker, C. Monroe, A. Gallagher, and C. Wieman, "Collisional losses from a light-force atom trap," Phys. Rev. Lett. **63**, 961–964 (1989).
http://link.aps.org/doi/10.1103/PhysRevLett.63.961
(Cited on page 38.)

[65] J. E. Simsarian, A. Ghosh, G. Gwinner, L. A. Orozco, G. D. Sprouse, and P. A. Voytas, "Magneto-Optic Trapping of ^{210}Fr," Phys. Rev. Lett. **76**, 3522–3525 (1996).
http://link.aps.org/doi/10.1103/PhysRevLett.76.3522
(Cited on page 38.)

[66] K. Sengstock, U. Sterr, G. Hennig, D. Bettermann, J. Mller, and W. Ertmer, "Optical Ramsey interferences on laser cooled and trapped atoms, detected by electron shelving," Optics Communications **103**, 73 – 78 (1993).
http://www.sciencedirect.com/science/article/pii/003040189390645L
(Cited on page 38.)

[67] T. Kurosu and F. Shimizu, "Laser Cooling and Trapping of Calcium and Strontium," Japanese Journal of Applied Physics **29**, L2127–L2129 (1990).
http://jjap.jsap.jp/link?JJAP/29/L2127/
(Cited on page 38.)

[68] S. De, U. Dammalapati, K. Jungmann, and L. Willmann, "Magneto-optical trapping of barium," Phys. Rev. A **79**, 041 402 (2009).
http://link.aps.org/doi/10.1103/PhysRevA.79.041402
(Cited on page 38.)

[69] J. R. Guest, N. D. Scielzo, I. Ahmad, K. Bailey, J. P. Greene, R. J. Holt, Z.-T. Lu, T. P. O'Connor, and D. H. Potterveld, "Laser Trapping of ^{225}Ra and ^{226}Ra with Repumping by Room-Temperature Blackbody Radiation," Phys. Rev. Lett. **98**, 093 001 (2007).
http://link.aps.org/doi/10.1103/PhysRevLett.98.093001
(Cited on page 38.)

[70] F. Bardou, O. Emile, J.-M. Courty, C. I. Westbrook, and A. Aspect, "Magneto-Optical Trapping of Metastable Helium: Collisions in the Presence of Resonant Light," EPL (Europhysics Letters) **20**, 681 (1992).
http://stacks.iop.org/0295-5075/20/i=8/a=003
(Cited on page 38.)

[71] F. Shimizu, K. Shimizu, and H. Takuma, "Laser cooling and trapping of Ne metastable atoms," Phys. Rev. A **39**, 2758–2760 (1989).
http://link.aps.org/doi/10.1103/PhysRevA.39.2758
(Cited on page 38.)

[72] H. Katori and F. Shimizu, "Laser Cooling and Trapping of Argon and Krypton Using Diode Lasers," Japanese Journal of Applied Physics **29**, L2124–L2126 (1990).
http://jjap.jsap.jp/link?JJAP/29/L2124/
(Cited on page 38.)

[73] M. Walhout, H. J. L. Megens, A. Witte, and S. L. Rolston, "Magneto-optical trapping of metastable xenon: Isotope-shift measurements," Phys. Rev. A **48**,

R879–R882 (1993).
http://link.aps.org/doi/10.1103/PhysRevA.48.R879
(Cited on page 38.)

[74] A. S. Bell, J. Stuhler, S. Locher, S. Hensler, J. Mlynek, and T. Pfau, "A magneto-optical trap for chromium with population repumping via intercombination lines," EPL (Europhysics Letters) **45**, 156 (1999).
http://stacks.iop.org/0295-5075/45/i=2/a=156
(Cited on page 38.)

[75] K. Honda, Y. Takahashi, T. Kuwamoto, M. Fujimoto, K. Toyoda, K. Ishikawa, and T. Yabuzaki, "Magneto-optical trapping of Yb atoms and a limit on the branching ratio of the $^1P_1$ state," Phys. Rev. A **59**, R934–R937 (1999).
http://link.aps.org/doi/10.1103/PhysRevA.59.R934
(Cited on page 38.)

[76] G. Uhlenberg, J. Dirscherl, and H. Walther, "Magneto-optical trapping of silver atoms," Phys. Rev. A **62**, 063 404 (2000).
http://link.aps.org/doi/10.1103/PhysRevA.62.063404
(Cited on page 38.)

[77] J. J. McClelland and J. L. Hanssen, "Laser Cooling without Repumping: A Magneto-Optical Trap for Erbium Atoms," Phys. Rev. Lett. **96**, 143 005 (2006).
http://link.aps.org/doi/10.1103/PhysRevLett.96.143005
(Cited on pages 38 and 46.)

[78] K.-A. Brickman, M.-S. Chang, M. Acton, A. Chew, D. Matsukevich, P. C. Haljan, V. S. Bagnato, and C. Monroe, "Magneto-optical trapping of cadmium," Phys. Rev. A **76**, 043 411 (2007).
http://link.aps.org/doi/10.1103/PhysRevA.76.043411
(Cited on page 38.)

[79] H. Hachisu, K. Miyagishi, S. G. Porsev, A. Derevianko, V. D. Ovsiannikov, V. G. Pal'chikov, M. Takamoto, and H. Katori, "Trapping of Neutral Mercury Atoms and Prospects for Optical Lattice Clocks," Phys. Rev. Lett. **100**, 053 001 (2008).
http://link.aps.org/doi/10.1103/PhysRevLett.100.053001
(Cited on page 38.)

[80] M. Lu, S. H. Youn, and B. L. Lev, "Trapping Ultracold Dysprosium: A Highly Magnetic Gas for Dipolar Physics," Phys. Rev. Lett. **104**, 063 001 (2010).
http://link.aps.org/doi/10.1103/PhysRevLett.104.063001
(Cited on page 38.)

[81] D. Sukachev, A. Sokolov, K. Chebakov, A. Akimov, S. Kanorsky, N. Kolachevsky, and V. Sorokin, "Magneto-optical trap for thulium atoms," Phys.

Rev. A **82**, 011 405 (2010).
http://link.aps.org/doi/10.1103/PhysRevA.82.011405
(Cited on page 38.)

[82] J. Miao, J. Hostetter, G. Stratis, and M. Saffman, "Magneto-optical trapping of holmium atoms," Phys. Rev. A **89**, 041 401 (2014).
http://link.aps.org/doi/10.1103/PhysRevA.89.041401
(Cited on page 38.)

[83] E. S. Shuman, J. F. Barry, D. R. Glenn, and D. DeMille, "Radiative Force from Optical Cycling on a Diatomic Molecule," Phys. Rev. Lett. **103**, 223 001 (2009).
http://link.aps.org/doi/10.1103/PhysRevLett.103.223001
(Cited on page 38.)

[84] M. T. Hummon, M. Yeo, B. K. Stuhl, A. L. Collopy, Y. Xia, and J. Ye, "2D Magneto-Optical Trapping of Diatomic Molecules," Phys. Rev. Lett. **110**, 143 001 (2013).
http://link.aps.org/doi/10.1103/PhysRevLett.110.143001
(Cited on page 38.)

[85] M. Zeppenfeld, B. G. U. Englert, R. Glöckner, A. Prehn, M. Mielenz, C. Sommer, L. D. van Buuren, M. Motsch, and G. Rempe, "Sisyphus cooling of electrically trapped polyatomic molecules," Nature **491**, 570–573 (2012).
(Cited on page 38.)

[86] T. Hänsch and A. Schawlow, Opt. Comm. **13** (1975).
(Cited on page 38.)

[87] D. Wineland and H. Dehmelt, Bull.Am.Phys.Soc. **20** (1975).
(Cited on page 38.)

[88] J. Dalibard and C. Cohen-Tannoudji, "Laser cooling below the Doppler limit by polarization gradients: simple theoretical models," J. Opt. Soc. Am. B **6**, 2023–2045 (1989).
http://josab.osa.org/abstract.cfm?URI=josab-6-11-2023
(Cited on pages 38, 47, and 55.)

[89] S. Chu, J. E. Bjorkholm, A. Ashkin, and A. Cable, "Experimental Observation of Optically Trapped Atoms," Phys. Rev. Lett. **57**, 314–317 (1986).
http://link.aps.org/doi/10.1103/PhysRevLett.57.314
(Cited on page 38.)

[90] P. D. Lett, W. D. Phillips, S. L. Rolston, C. E. Tanner, R. N. Watts, and C. I. Westbrook, "Optical molasses," J. Opt. Soc. Am. B **6**, 2084–2107 (1989).
http://josab.osa.org/abstract.cfm?URI=josab-6-11-2084
(Cited on pages 38 and 41.)

[91] A. Aspect, E. Arimondo, R. Kaiser, N. Vansteenkiste, and C. Cohen-Tannoudji, "Laser Cooling below the One-Photon Recoil Energy by Velocity-Selective Coherent Population Trapping," Phys. Rev. Lett. **61**, 826–829 (1988).
http://link.aps.org/doi/10.1103/PhysRevLett.61.826
(Cited on page 39.)

[92] S. E. Hamann, D. L. Haycock, G. Klose, P. H. Pax, I. H. Deutsch, and P. S. Jessen, "Resolved-Sideband Raman Cooling to the Ground State of an Optical Lattice," Phys. Rev. Lett. **80**, 4149–4152 (1998).
http://link.aps.org/doi/10.1103/PhysRevLett.80.4149
(Cited on page 39.)

[93] H. Perrin, A. Kuhn, I. Bouchoule, and C. Salomon, "Sideband cooling of neutral atoms in a far-detuned optical lattice," EPL (Europhysics Letters) **42**, 395 (1998).
http://stacks.iop.org/0295-5075/42/i=4/a=395
(Cited on page 39.)

[94] V. Vuletić, C. Chin, A. J. Kerman, and S. Chu, "Degenerate Raman Sideband Cooling of Trapped Cesium Atoms at Very High Atomic Densities," Phys. Rev. Lett. **81**, 5768–5771 (1998).
http://link.aps.org/doi/10.1103/PhysRevLett.81.5768
(Cited on page 39.)

[95] A. Aspect, J. Dalibard, A. Heidmann, C. Salomon, and C. Cohen-Tannoudji, "Cooling Atoms with Stimulated Emission," Phys. Rev. Lett. **57**, 1688–1691 (1986).
http://link.aps.org/doi/10.1103/PhysRevLett.57.1688
(Cited on page 39.)

[96] D. E. Pritchard, "Cooling Neutral Atoms in a Magnetic Trap for Precision Spectroscopy," Phys. Rev. Lett. **51**, 1336–1339 (1983).
http://link.aps.org/doi/10.1103/PhysRevLett.51.1336
(Cited on page 39.)

[97] J. J. Tollett, J. Chen, J. G. Story, N. W. M. Ritchie, C. C. Bradley, and R. G. Hulet, "Observation of velocity-tuned multiphoton "Doppleron" resonances in laser-cooled atoms," Phys. Rev. Lett. **65**, 559–562 (1990).
http://link.aps.org/doi/10.1103/PhysRevLett.65.559
(Cited on page 39.)

[98] E. A. Curtis, C. W. Oates, and L. Hollberg, "Quenched narrow-line laser cooling of ^{40}Ca to near the photon recoil limit," Phys. Rev. A **64**, 031 403 (2001).
http://link.aps.org/doi/10.1103/PhysRevA.64.031403
(Cited on page 39.)

[99] T. Binnewies, G. Wilpers, U. Sterr, F. Riehle, J. Helmcke, T. E. Mehlstäubler, E. M. Rasel, and W. Ertmer, "Doppler Cooling and Trapping on Forbidden Transitions," Phys. Rev. Lett. **87**, 123 002 (2001).
http://link.aps.org/doi/10.1103/PhysRevLett.87.123002
(Cited on page 39.)

[100] N. Malossi, S. Damkjær, P. L. Hansen, L. B. Jacobsen, L. Kindt, S. Sauge, J. W. Thomsen, F. C. Cruz, M. Allegrini, and E. Arimondo, "Two-photon cooling of magnesium atoms," Phys. Rev. A **72**, 051 403 (2005).
http://link.aps.org/doi/10.1103/PhysRevA.72.051403
(Cited on page 39.)

[101] S. Stellmer, B. Pasquiou, R. Grimm, and F. Schreck, "Laser Cooling to Quantum Degeneracy," Phys. Rev. Lett. **110**, 263 003 (2013).
http://link.aps.org/doi/10.1103/PhysRevLett.110.263003
(Cited on page 39.)

[102] M. Kumakura and N. Morita, "Visible Observation of Metastable Helium Atoms Confined in an Infrared/Visible Double Resonance Trap," Japanese Journal of Applied Physics **31**, L276–L279 (1992).
http://jjap.jsap.jp/link?JJAP/31/L276/
(Cited on page 39.)

[103] W. S. Bakr, A. Peng, M. E. Tai, R. Ma, J. Simon, J. I. Gillen, S. Foelling, L. Pollet, and M. Greiner, "Probing the superfluid–to–mott insulator transition at the single-atom level," Science **329**, 547–550 (2010).
(Cited on pages 39 and 110.)

[104] C. Y. Chen, Y. M. Li, K. Bailey, T. P. O'Connor, L. Young, and Z.-T. Lu, "Ultrasensitive Isotope Trace Analyses with a Magneto-Optical Trap," Science **286**, 1139–1141 (1999).
http://www.sciencemag.org/content/286/5442/1139.abstract
(Cited on page 39.)

[105] C. Cohen-Tannoudji, *"Fundamental Systems in Quantum Optics"* (Wiley, New York, 1990).
(Cited on pages 41 and 43.)

[106] C. Cohen-Tannoudji, J. Dupont-Roc, and G. Grynberg, *Atom-Photon Interactions* (Wiley, New York, 1992).
(Cited on page 43.)

[107] J. P. Gordon and A. Ashkin, "Motion of atoms in a radiation trap," Phys. Rev. A **21**, 1606–1617 (1980).
http://link.aps.org/doi/10.1103/PhysRevA.21.1606
(Cited on page 43.)

[108] R. Chang, L. Hoendervanger, Q. Bouton, Y. Fang, T. Klafka, K. Audo, A. Aspect, C. I. Westbrook, and D. Clément, "Three-dimensional laser cooling at the Doppler limit," ArXiv e-prints (2014).
(Cited on page 45.)

[109] H. Metcalf and P. van der Straten, *Laser Cooling and Trapping* (Springer-Verlag, New York, 1999).
(Cited on page 46.)

[110] P. D. Lett, R. N. Watts, C. I. Westbrook, W. D. Phillips, P. L. Gould, and H. J. Metcalf, "Observation of Atoms Laser Cooled below the Doppler Limit," Phys. Rev. Lett. **61**, 169–172 (1988).
http://link.aps.org/doi/10.1103/PhysRevLett.61.169
(Cited on page 46.)

[111] I. D. Setija, H. G. C. Werij, O. J. Luiten, M. W. Reynolds, T. W. Hijmans, and J. T. M. Walraven, "Optical cooling of atomic hydrogen in a magnetic trap," Phys. Rev. Lett. **70**, 2257–2260 (1993).
http://link.aps.org/doi/10.1103/PhysRevLett.70.2257
(Cited on page 55.)

[112] G. B. Andresen et al., "Trapped antihydrogen," Nature **468**, 673–676 (2010).
(Cited on page 56.)

[113] Y. Enomoto, N. Kuroda, K. Michishio, C. H. Kim, H. Higaki, Y. Nagata, Y. Kanai, H. A. Torii, M. Corradini, M. Leali, E. Lodi-Rizzini, V. Mascagna, L. Venturelli, N. Zurlo, K. Fujii, M. Ohtsuka, K. Tanaka, H. Imao, Y. Nagashima, Y. Matsuda, B. Juhász, A. Mohri, and Y. Yamazaki, "Synthesis of Cold Antihydrogen in a Cusp Trap," Phys. Rev. Lett. **105**, 243 401 (2010).
http://link.aps.org/doi/10.1103/PhysRevLett.105.243401
(Cited on page 56.)

[114] G. Gabrielse, R. Kalra, W. S. Kolthammer, R. McConnell, P. Richerme, D. Grzonka, W. Oelert, T. Sefzick, M. Zielinski, D. W. Fitzakerley, M. C. George, E. A. Hessels, C. H. Storry, M. Weel, A. Müllers, and J. Walz, "Trapped Antihydrogen in Its Ground State," Phys. Rev. Lett. **108**, 113 002 (2012).
http://link.aps.org/doi/10.1103/PhysRevLett.108.113002
(Cited on page 56.)

[115] M. Allegrini and E. Arimondo, "Pulsed laser cooling of hydrogen atoms," Physics Letters A **172**, 271 – 276 (1993).
http://www.sciencedirect.com/science/article/pii/0375960193910206
(Cited on page 56.)

[116] V. Zehnlé and J. C. Garreau, "Continuous-wave Doppler cooling of hydrogen atoms with two-photon transitions," Phys. Rev. A **63**, 021 402 (2001).
http://link.aps.org/doi/10.1103/PhysRevA.63.021402
(Cited on page 56.)

[117] D. Kielpinski, "Laser cooling of atoms and molecules with ultrafast pulses," Phys. Rev. A **73**, 063 407 (2006).
http://link.aps.org/doi/10.1103/PhysRevA.73.063407
(Cited on page 56.)

[118] L. P. Yatsenko, B. W. Shore, T. Halfmann, K. Bergmann, and A. Vardi, "Source of metastable H(2s) atoms using the Stark chirped rapid-adiabatic-passage technique," Phys. Rev. A **60**, R4237–R4240 (1999).
http://link.aps.org/doi/10.1103/PhysRevA.60.R4237
(Cited on page 57.)

[119] M. H. Anderson, J. R. Ensher, M. R. Matthews, C. E. Wieman, and E. A. Cornell, "Observation of Bose-Einstein Condensation in a Dilute Atomic Vapor," Science **269**, 198–201 (1995).
http://www.sciencemag.org/content/269/5221/198.abstract
(Cited on page 60.)

[120] K. B. Davis, M. O. Mewes, M. R. Andrews, N. J. van Druten, D. S. Durfee, D. M. Kurn, and W. Ketterle, "Bose-Einstein Condensation in a Gas of Sodium Atoms," Phys. Rev. Lett. **75**, 3969–3973 (1995).
http://link.aps.org/doi/10.1103/PhysRevLett.75.3969
(Cited on page 60.)

[121] B. DeMarco and D. S. Jin, "Onset of Fermi Degeneracy in a Trapped Atomic Gas," Science **285**, 1703–1706 (1999).
http://www.sciencemag.org/content/285/5434/1703.abstract
(Cited on page 60.)

[122] C. A. Regal, M. Greiner, and D. S. Jin, "Observation of Resonance Condensation of Fermionic Atom Pairs," Phys. Rev. Lett. **92**, 040 403 (2004).
http://link.aps.org/doi/10.1103/PhysRevLett.92.040403
(Cited on page 60.)

[123] M. W. Zwierlein, C. A. Stan, C. H. Schunck, S. M. F. Raupach, A. J. Kerman, and W. Ketterle, "Condensation of Pairs of Fermionic Atoms near a Feshbach Resonance," Phys. Rev. Lett. **92**, 120 403 (2004).
http://link.aps.org/doi/10.1103/PhysRevLett.92.120403
(Cited on page 60.)

[124] M. Bartenstein, A. Altmeyer, S. Riedl, S. Jochim, C. Chin, J. H. Denschlag, and R. Grimm, "Collective Excitations of a Degenerate Gas at the BEC-BCS Crossover," Phys. Rev. Lett. **92**, 203 201 (2004).
http://link.aps.org/doi/10.1103/PhysRevLett.92.203201
(Cited on page 60.)

[125] M. Greiner, O. Mandel, T. Esslinger, T. W. Hänsch, and I. Bloch, "Quantum phase transition from a superfluid to a Mott insulator in a gas of ultracold

atoms," Nature **415**, 39–44 (2002).
(Cited on pages 60 and 108.)

[126] Y.-J. Lin, K. Jimenez-Garcia, and I. Spielman, "Spin-orbit-coupled Bose-Einstein condensates," Nature **471**, 83–86 (2011).
(Cited on page 60.)

[127] N. R. Cooper, "Optical Flux Lattices for Ultracold Atomic Gases," Phys. Rev. Lett. **106**, 175 301 (2011).
http://link.aps.org/doi/10.1103/PhysRevLett.106.175301
(Cited on page 60.)

[128] A. V. Gorshkov, M. Hermele, V. Gurarie, C. Xu, P. S. Julienne, J. Ye, P. Zoller, E. Demler, M. D. Lukin, and A. M. Rey, "Two-orbital SU(N) magnetism with ultracold alkaline-earth atoms," Nature Physics **6**, 289–295 (2010).
(Cited on page 60.)

[129] S. Taie, Y. Takasu, S. Sugawa, R. Yamazaki, T. Tsujimoto, R. Murakami, and Y. Takahashi, "Realization of a SU(2) × SU(6) System of Fermions in a Cold Atomic Gas," Phys. Rev. Lett. **105**, 190 401 (2010).
http://link.aps.org/doi/10.1103/PhysRevLett.105.190401
(Cited on page 60.)

[130] M. Foss-Feig, M. Hermele, and A. M. Rey, "Probing the Kondo lattice model with alkaline-earth-metal atoms," Phys. Rev. A **81**, 051 603 (2010).
http://link.aps.org/doi/10.1103/PhysRevA.81.051603
(Cited on page 60.)

[131] A. de Paz, A. Sharma, A. Chotia, E. Maréchal, J. H. Huckans, P. Pedri, L. Santos, O. Gorceix, L. Vernac, and B. Laburthe-Tolra, "Nonequilibrium Quantum Magnetism in a Dipolar Lattice Gas," Phys. Rev. Lett. **111**, 185 305 (2013).
http://link.aps.org/doi/10.1103/PhysRevLett.111.185305
(Cited on pages 60 and 139.)

[132] Y.-J. Lin, A. R. Perry, R. L. Compton, I. B. Spielman, and J. V. Porto, "Rapid production of ^{87}Rb Bose-Einstein condensates in a combined magnetic and optical potential," Phys. Rev. A **79**, 063 631 (2009).
http://link.aps.org/doi/10.1103/PhysRevA.79.063631
(Cited on pages 61, 70, 76, 83, and 95.)

[133] W. D. Phillips and H. Metcalf, "Laser Deceleration of an Atomic Beam," Phys. Rev. Lett. **48**, 596–599 (1982).
http://link.aps.org/doi/10.1103/PhysRevLett.48.596
(Cited on page 63.)

[134] S. C. Bell, M. Junker, M. Jasperse, L. D. Turner, Y.-J. Lin, I. B. Spielman, and R. E. Scholten., "A slow atom source using a collimated effusive oven and

a single-layer variable pitch coil Zeeman slower," Rev. Sci. Inst. **81**, 013 105 (2010).
(Cited on page 63.)

[135] K. Odaka and S. Ueda, "Dependence of outgassing rate on surface oxide layer thickness in type 304 stainless steel before and after surface oxidation in air," Vacuum **47**, 689 – 692 (1996), proceedings of the 13th International Vacuum Congress and the 9th International Conference on Solid Surfaces.
http://www.sciencedirect.com/science/article/pii/0042207X96000486
(Cited on page 66.)

[136] J. C. Maxwell, Scientific Papers **2**, 505 (1890).
(Cited on page 77.)

[137] ISO Standard 11670, Lasers and laser-related equipment - Test methods for laser beam parameters - Beam positional stability.
(Cited on page 79.)

[138] R. Paschotta, "Noise in Laser Technology," Optik and Photonik **5**, 55–57 (2010).
http://dx.doi.org/10.1002/opph.201190083
(Cited on page 79.)

[139] K. B. MacAdam, A. Steinbach, and C. Wieman, "A narrow band tunable diode laser system with grating feedback, and a saturated absorption spectrometer for Cs and Rb," American Journal of Physics **60**, 1098–1111 (1992).
http://scitation.aip.org/content/aapt/journal/ajp/60/12/10.1119/1.16955
(Cited on page 83.)

[140] U. Schnemann, H. Engler, R. Grimm, M. Weidemller, and M. Zielonkowski, "Simple scheme for tunable frequency offset locking of two lasers," Review of Scientific Instruments **70**, 242–243 (1999).
http://scitation.aip.org/content/aip/journal/rsi/70/1/10.1063/1.1149573
(Cited on page 83.)

[141] R. Grimm, M. Weidemueller, and Y. B. Ovchinnikov, "Optical Dipole Traps for Neutral Atoms," **42**, 95 – 170 (2000).
http://www.sciencedirect.com/science/article/pii/S1049250X0860186X
(Cited on page 83.)

[142] V. Letokhov, "Doppler line narrowing in a standing light wave," JETP Lett. **7**, 272–274 (1968).
(Cited on page 99.)

[143] C. I. Westbrook, R. N. Watts, C. E. Tanner, S. L. Rolston, W. D. Phillips, P. D. Lett, and P. L. Gould, "Localization of atoms in a three-dimensional standing wave," Phys. Rev. Lett. **65**, 33–36 (1990).

http://link.aps.org/doi/10.1103/PhysRevLett.65.33
(Cited on page 99.)

[144] S. K. Dutta, B. K. Teo, and G. Raithel, "Tunneling Dynamics and Gauge Potentials in Optical Lattices," Phys. Rev. Lett. **83**, 1934–1937 (1999).
http://link.aps.org/doi/10.1103/PhysRevLett.83.1934
(Cited on page 99.)

[145] R. Feynman, "Simulating physics with computers," International Journal of Theoretical Physics **21**, 467–488 (1982).
http://dx.doi.org/10.1007/BF02650179
(Cited on page 99.)

[146] M. Greiner, O. Mandel, T. Esslinger, T. W. Hänsch, and I. Bloch, "Quantum phase transition from a superfluid to a Mott insulator in a gas of ultracold atoms," Nature **415**, 39–44 (2002).
(Cited on page 100.)

[147] D. Bitko, T. F. Rosenbaum, and G. Aeppli, "Quantum Critical Behavior for a Model Magnet," Phys. Rev. Lett. **77**, 940–943 (1996).
http://link.aps.org/doi/10.1103/PhysRevLett.77.940
(Cited on page 100.)

[148] R. Coldea, D. A. Tennant, E. M. Wheeler, E. Wawrzynska, D. Prabhakaran, M. Telling, K. Habicht, P. Smeibidl, and K. Kiefer, "Quantum Criticality in an Ising Chain: Experimental Evidence for Emergent E8 Symmetry," Science **327**, 177–180 (2010).
http://www.sciencemag.org/content/327/5962/177.abstract
(Cited on page 100.)

[149] P. Medley, D. M. Weld, H. Miyake, D. E. Pritchard, and W. Ketterle, "Spin Gradient Demagnetization Cooling of Ultracold Atoms," Phys. Rev. Lett. **106**, 195 301 (2011).
http://link.aps.org/doi/10.1103/PhysRevLett.106.195301
(Cited on page 100.)

[150] R. A. Hart, P. M. Duarte, T.-L. Yang, X. Liu, T. Paiva, E. Khatami, R. T. Scalettar, N. Trivedi, D. A. Huse, and R. G. Hulet, "Observation of antiferromagnetic correlations in the Hubbard model with ultracold atoms," ArXiv e-prints (2014).
(Cited on pages 100 and 139.)

[151] S. Trotzky, P. Cheinet, S. Flling, M. Feld, U. Schnorrberger, A. M. Rey, A. Polkovnikov, E. A. Demler, M. D. Lukin, and I. Bloch, "Time-Resolved Observation and Control of Superexchange Interactions with Ultracold Atoms in Optical Lattices," Science **319**, 295–299 (2008).
http://www.sciencemag.org/content/319/5861/295.abstract
(Cited on pages 101, 139, and 142.)

[152] Y.-A. Chen, S. Nascimbène, M. Aidelsburger, M. Atala, S. Trotzky, and I. Bloch, "Controlling Correlated Tunneling and Superexchange Interactions with ac-Driven Optical Lattices," Phys. Rev. Lett. **107**, 210 405 (2011).
http://link.aps.org/doi/10.1103/PhysRevLett.107.210405
(Cited on page 101.)

[153] D. Greif, T. Uehlinger, G. Jotzu, L. Tarruell, and T. Esslinger, "Short-Range Quantum Magnetism of Ultracold Fermions in an Optical Lattice," Science **340**, 1307–1310 (2013).
(Cited on pages 101 and 139.)

[154] L. Esaki and R. Tsu, "Superlattice and negative differential conductivity in semiconductors," IBM Journal of Research and Development **14**, 61–65 (1970).
(Cited on page 101.)

[155] N. Strohmaier, D. Greif, R. Jördens, L. Tarruell, H. Moritz, T. Esslinger, R. Sensarma, D. Pekker, E. Altman, and E. Demler, "Observation of elastic doublon decay in the Fermi-Hubbard model," Physical review letters **104**, 080 401 (2010).
(Cited on pages 101, 140, and 150.)

[156] S. Trotzky, Y.-A. Chen, A. Flesch, I. P. McCulloch, U. Schollwöck, J. Eisert, and I. Bloch, "Probing the relaxation towards equilibrium in an isolated strongly correlated one-dimensional Bose gas," Nature Physics **8**, 325–330 (2012).
(Cited on page 101.)

[157] P. Barmettler, A. M. Rey, E. Demler, M. D. Lukin, I. Bloch, and V. Gritsev, "Quantum many-body dynamics of coupled double-well superlattices," Phys. Rev. A **78**, 012 330 (2008).
http://link.aps.org/doi/10.1103/PhysRevA.78.012330
(Cited on page 101.)

[158] S. Peil, J. V. Porto, B. L. Tolra, J. M. Obrecht, B. E. King, M. Subbotin, S. L. Rolston, and W. D. Phillips, "Patterned loading of a Bose-Einstein condensate into an optical lattice," Phys. Rev. A **67**, 051 603 (2003).
http://link.aps.org/doi/10.1103/PhysRevA.67.051603
(Cited on page 101.)

[159] O. Mandel, M. Greiner, A. Widera, T. Rom, T. W. Hänsch, and I. Bloch, "Coherent Transport of Neutral Atoms in Spin-Dependent Optical Lattice Potentials," Phys. Rev. Lett. **91**, 010 407 (2003).
http://link.aps.org/doi/10.1103/PhysRevLett.91.010407
(Cited on page 101.)

[160] P. Soltan-Panahi, J. Struck, P. Hauke, A. Bick, W. Plenkers, G. Meineke, C. Becker, P. Windpassinger, M. Lewenstein, and K. Sengstock, "Multi-component quantum gases in spin-dependent hexagonal lattices," Nature Physics **7**, 434–440 (2011).
(Cited on page 101.)

[161] G.-B. Jo, J. Guzman, C. K. Thomas, P. Hosur, A. Vishwanath, and D. M. Stamper-Kurn, "Ultracold Atoms in a Tunable Optical Kagome Lattice," Phys. Rev. Lett. **108**, 045 305 (2012).
http://link.aps.org/doi/10.1103/PhysRevLett.108.045305
(Cited on page 101.)

[162] M. Anderlini, P. J. Lee, B. L. Brown, J. Sebby-Strabley, W. D. Phillips, and J. Porto, "Controlled exchange interaction between pairs of neutral atoms in an optical lattice," Nature **448**, 452–456 (2007).
(Cited on page 101.)

[163] A. S. Sørensen, E. Altman, M. Gullans, J. V. Porto, M. D. Lukin, and E. Demler, "Adiabatic preparation of many-body states in optical lattices," Phys. Rev. A **81**, 061 603 (2010).
http://link.aps.org/doi/10.1103/PhysRevA.81.061603
(Cited on pages 101 and 140.)

[164] M. Lubasch, V. Murg, U. Schneider, J. I. Cirac, and M.-C. Bañuls, "Adiabatic Preparation of a Heisenberg Antiferromagnet Using an Optical Superlattice," Phys. Rev. Lett. **107**, 165 301 (2011).
http://link.aps.org/doi/10.1103/PhysRevLett.107.165301
(Cited on pages 101 and 140.)

[165] L. Van Hove, "Time-Dependent Correlations between Spins and Neutron Scattering in Ferromagnetic Crystals," Phys. Rev. **95**, 1374–1384 (1954).
http://link.aps.org/doi/10.1103/PhysRev.95.1374
(Cited on page 101.)

[166] W. H. Zurek, U. Dorner, and P. Zoller, "Dynamics of a Quantum Phase Transition," Phys. Rev. Lett. **95**, 105 701 (2005).
http://link.aps.org/doi/10.1103/PhysRevLett.95.105701
(Cited on page 101.)

[167] P. Barmettler, M. Punk, V. Gritsev, E. Demler, and E. Altman, "Relaxation of Antiferromagnetic Order in Spin-1/2 Chains Following a Quantum Quench," Phys. Rev. Lett. **102**, 130 603 (2009).
http://link.aps.org/doi/10.1103/PhysRevLett.102.130603
(Cited on pages 101 and 140.)

[168] I. H. Deutsch and P. S. Jessen, "Quantum-state control in optical lattices," Phys. Rev. A **57**, 1972–1986 (1998).

http://link.aps.org/doi/10.1103/PhysRevA.57.1972
(Cited on page 102.)

[169] N. Marzari, A. A. Mostofi, J. R. Yates, I. Souza, and D. Vanderbilt, "Maximally localized Wannier functions: Theory and applications," Rev. Mod. Phys. **84**, 1419–1475 (2012).
http://link.aps.org/doi/10.1103/RevModPhys.84.1419
(Cited on page 103.)

[170] J. Hubbard, "Electron Correlations in Narrow Energy Bands," Proceedings of the Royal Society of London. Series A. Mathematical and Physical Sciences **276**, 238–257 (1963).
http://rspa.royalsocietypublishing.org/content/276/1365/238.abstract
(Cited on page 104.)

[171] H. A. Gersch and G. C. Knollman, "Quantum Cell Model for Bosons," Phys. Rev. **129**, 959–967 (1963).
http://link.aps.org/doi/10.1103/PhysRev.129.959
(Cited on page 104.)

[172] M. P. A. Fisher, P. B. Weichman, G. Grinstein, and D. S. Fisher, "Boson localization and the superfluid-insulator transition," Phys. Rev. B **40**, 546–570 (1989).
http://link.aps.org/doi/10.1103/PhysRevB.40.546
(Cited on pages 104 and 105.)

[173] D. Jaksch, C. Bruder, J. I. Cirac, C. W. Gardiner, and P. Zoller, "Cold bosonic atoms in optical lattices," Physical Review Letters **81**, 3108 (1998).
(Cited on pages 104, 139, and 140.)

[174] N. F. Mott and R. Peierls, "Discussion of the paper by de Boer and Verwey," Proceedings of the Physical Society **49**, 72 (1937).
http://stacks.iop.org/0959-5309/49/i=4S/a=308
(Cited on page 105.)

[175] N. F. Mott, "The Basis of the Electron Theory of Metals, with Special Reference to the Transition Metals," Proceedings of the Physical Society. Section A **62**, 416 (1949).
http://stacks.iop.org/0370-1298/62/i=7/a=303
(Cited on page 105.)

[176] T. D. Kühner, S. R. White, and H. Monien, "One-dimensional Bose-Hubbard model with nearest-neighbor interaction," Phys. Rev. B **61**, 12 474–12 489 (2000).
http://link.aps.org/doi/10.1103/PhysRevB.61.12474
(Cited on page 105.)

[177] L. D. Carr, M. L. Wall, D. G. Schirmer, R. C. Brown, J. E. Williams, and C. W. Clark, "Mesoscopic effects in quantum phases of ultracold quantum gases in optical lattices," Phys. Rev. A **81**, 013 613 (2010).
http://link.aps.org/doi/10.1103/PhysRevA.81.013613
(Cited on page 105.)

[178] F. Gerbier, "Boson Mott Insulators at Finite Temperatures," Phys. Rev. Lett. **99**, 120 405 (2007).
http://link.aps.org/doi/10.1103/PhysRevLett.99.120405
(Cited on page 106.)

[179] A. Auerbach, *Interacting electrons and quantum magnetism* (Springer, 1994).
(Cited on pages 106 and 139.)

[180] L.-M. Duan, E. Demler, and M. D. Lukin, "Controlling Spin Exchange Interactions of Ultracold Atoms in Optical Lattices," Phys. Rev. Lett. **91**, 090 402 (2003).
http://link.aps.org/doi/10.1103/PhysRevLett.91.090402
(Cited on pages 107, 139, and 141.)

[181] C. D. Fertig, K. M. O'Hara, J. H. Huckans, S. L. Rolston, W. D. Phillips, and J. V. Porto, "Strongly Inhibited Transport of a Degenerate 1D Bose Gas in a Lattice," Phys. Rev. Lett. **94**, 120 403 (2005).
http://link.aps.org/doi/10.1103/PhysRevLett.94.120403
(Cited on page 109.)

[182] J. Stenger, S. Inouye, A. P. Chikkatur, D. M. Stamper-Kurn, D. E. Pritchard, and W. Ketterle, "Bragg Spectroscopy of a Bose-Einstein Condensate," Phys. Rev. Lett. **82**, 4569–4573 (1999).
http://link.aps.org/doi/10.1103/PhysRevLett.82.4569
(Cited on page 109.)

[183] J. Stenger, S. Inouye, A. P. Chikkatur, D. M. Stamper-Kurn, D. E. Pritchard, and W. Ketterle, "Erratum: Bragg Spectroscopy of a Bose-Einstein Condensate [Phys. Rev. Lett. 82, 4569 (1999)]," Phys. Rev. Lett. **84**, 2283–2283 (2000).
http://link.aps.org/doi/10.1103/PhysRevLett.84.2283
(Cited on page 109.)

[184] T. Stöferle, H. Moritz, C. Schori, M. Köhl, and T. Esslinger, "Transition from a strongly interacting 1D superfluid to a Mott insulator," Physical review letters **92**, 130 403 (2004).
(Cited on page 109.)

[185] A. Tokuno and T. Giamarchi, "Spectroscopy for cold atom gases in periodically phase-modulated optical lattices," Physical Review Letters **106**, 205 301 (2011).
(Cited on page 109.)

[186] S. Fölling, F. Gerbier, A. Widera, O. Mandel, T. Gericke, and I. Bloch, "Spatial quantum noise interferometry in expanding ultracold atom clouds," Nature **434**, 481–484 (2005).
(Cited on page 109.)

[187] G. K. Campbell, J. Mun, M. Boyd, P. Medley, A. E. Leanhardt, L. G. Marcassa, D. E. Pritchard, and W. Ketterle, "Imaging the Mott Insulator Shells by Using Atomic Clock Shifts," Science **313**, 649–652 (2006).
(Cited on pages 110, 136, 151, and 152.)

[188] C. Weitenberg, M. Endres, J. F. Sherson, M. Cheneau, P. Schauß, T. Fukuhara, I. Bloch, and S. Kuhr, "Single-spin addressing in an atomic Mott insulator," Nature **471**, 319–324 (2011).
(Cited on page 110.)

[189] J. Sebby-Strabley, M. Anderlini, P. S. Jessen, and J. V. Porto, "Lattice of double wells for manipulating pairs of cold atoms," Phys. Rev. A **73**, 033 605 (2006).
http://link.aps.org/doi/10.1103/PhysRevA.73.033605
(Cited on pages 111, 126, 140, 153, and 154.)

[190] P. J. Lee, M. Anderlini, B. L. Brown, J. Sebby-Strabley, W. D. Phillips, and J. V. Porto, "Sublattice Addressing and Spin-Dependent Motion of Atoms in a Double-Well Lattice," Phys. Rev. Lett. **99**, 020 402 (2007).
http://link.aps.org/doi/10.1103/PhysRevLett.99.020402
(Cited on pages 111, 130, 140, 144, and 154.)

[191] J. Sebby-Strabley, B. L. Brown, M. Anderlini, P. J. Lee, W. D. Phillips, J. V. Porto, and P. R. Johnson, "Preparing and Probing Atomic Number States with an Atom Interferometer," Phys. Rev. Lett. **98**, 200 405 (2007).
http://link.aps.org/doi/10.1103/PhysRevLett.98.200405
(Cited on pages 111, 126, 133, and 154.)

[192] G. Grynberg, B. Lounis, P. Verkerk, J.-Y. Courtois, and C. Salomon, "Quantized motion of cold cesium atoms in two- and three-dimensional optical potentials," Phys. Rev. Lett. **70**, 2249–2252 (1993).
http://link.aps.org/doi/10.1103/PhysRevLett.70.2249
(Cited on page 113.)

[193] A. Hemmerich and T. W. Hänsch, "Radiation pressure vortices in two crossed standing waves," Phys. Rev. Lett. **68**, 1492–1495 (1992).
http://link.aps.org/doi/10.1103/PhysRevLett.68.1492
(Cited on page 113.)

[194] A. Rauschenbeutel, H. Schadwinkel, V. Gomer, and D. Meschede, "Standing light fields for cold atoms with intrinsically stable and variable time phases," Optics Communications **148**, 45 – 48 (1998).

http://www.sciencedirect.com/science/article/pii/S003040189700669X
(Cited on page 113.)

[195] S. S. Natu, D. C. McKay, B. DeMarco, and E. J. Mueller, "Evolution of condensate fraction during rapid lattice ramps," Phys. Rev. A **85**, 061 601 (2012).
http://link.aps.org/doi/10.1103/PhysRevA.85.061601
(Cited on page 127.)

[196] L. Deng, E. W. Hagley, J. Denschlag, J. E. Simsarian, M. Edwards, C. W. Clark, K. Helmerson, S. L. Rolston, and W. D. Phillips, "Temporal, Matter-Wave-Dispersion Talbot Effect," Phys. Rev. Lett. **83**, 5407–5411 (1999).
http://link.aps.org/doi/10.1103/PhysRevLett.83.5407
(Cited on page 128.)

[197] N. Lundblad, M. Schlosser, and J. V. Porto, "Experimental observation of magic-wavelength behavior of ^{87}Rb atoms in an optical lattice," Phys. Rev. A **81**, 031 611 (2010).
http://link.aps.org/doi/10.1103/PhysRevA.81.031611
(Cited on page 136.)

[198] R. Chicireanu, K. D. Nelson, S. Olmschenk, N. Lundblad, A. Derevianko, and J. V. Porto, "Differential Light-Shift Cancellation in a Magnetic-Field-Insensitive Transition of ^{87}Rb," Phys. Rev. Lett. **106**, 063 002 (2011).
http://link.aps.org/doi/10.1103/PhysRevLett.106.063002
(Cited on page 136.)

[199] D. M. Harber, H. J. Lewandowski, J. M. McGuirk, and E. A. Cornell, "Effect of cold collisions on spin coherence and resonance shifts in a magnetically trapped ultracold gas," Phys. Rev. A **66**, 053 616 (2002).
http://link.aps.org/doi/10.1103/PhysRevA.66.053616
(Cited on page 136.)

[200] E. G. M. van Kempen, S. J. J. M. F. Kokkelmans, D. J. Heinzen, and B. J. Verhaar, "Interisotope Determination of Ultracold Rubidium Interactions from Three High-Precision Experiments," Phys. Rev. Lett. **88**, 093 201 (2002).
http://link.aps.org/doi/10.1103/PhysRevLett.88.093201
(Cited on page 136.)

[201] K. R. A. Hazzard and E. J. Mueller, "Hyperfine spectra of trapped bosons in optical lattices," Phys. Rev. A **76**, 063 612 (2007).
http://link.aps.org/doi/10.1103/PhysRevA.76.063612
(Cited on page 137.)

[202] D. J. Scalapino, "A common thread: The pairing interaction for unconventional superconductors," Rev. Mod. Phys. **84**, 1383–1417 (2012).
http://link.aps.org/doi/10.1103/RevModPhys.84.1383
(Cited on page 139.)

[203] T. Fukuhara, P. Schauß, M. Endres, S. Hild, M. Cheneau, I. Bloch, and C. Gross, "Microscopic observation of magnon bound states and their dynamics," Nature (London) **502**, 76–79 (2013).
(Cited on pages 139 and 150.)

[204] S. Hild, T. Fukuhara, P. Schauß, J. Zeiher, M. Knap, E. Demler, I. Bloch, and C. Gross, "Far-from-Equilibrium Spin Transport in Heisenberg Quantum Magnets," Phys. Rev. Lett. **113**, 147 205 (2014).
http://link.aps.org/doi/10.1103/PhysRevLett.113.147205
(Cited on pages 139 and 141.)

[205] B. Yan, S. A. Moses, B. Gadway, J. P. Covey, K. R. Hazzard, A. M. Rey, D. S. Jin, and J. Ye, "Observation of dipolar spin-exchange interactions with lattice-confined polar molecules," Nature (London) **501**, 521 (2013).
(Cited on page 139.)

[206] A. V. Gorshkov, S. R. Manmana, G. Chen, J. Ye, E. Demler, M. D. Lukin, and A. M. Rey, "Tunable Superfluidity and Quantum Magnetism with Ultracold Polar Molecules," Phys. Rev. Lett. **107**, 115 301 (2011).
http://link.aps.org/doi/10.1103/PhysRevLett.107.115301
(Cited on page 139.)

[207] M. Boninsegni, "Phase Separation in Mixtures of Hard Core Bosons," Phys. Rev. Lett. **87**, 087 201 (2001).
http://link.aps.org/doi/10.1103/PhysRevLett.87.087201
(Cited on page 140.)

[208] A. B. Kuklov and B. V. Svistunov, "Counterflow Superfluidity of Two-Species Ultracold Atoms in a Commensurate Optical Lattice," Phys. Rev. Lett. **90**, 100 401 (2003).
http://link.aps.org/doi/10.1103/PhysRevLett.90.100401
(Cited on page 140.)

[209] E. Altman, W. Hofstetter, E. Demler, and M. D. Lukin, "Phase diagram of two-component bosons on an optical lattice," New Journal of Physics **5**, 113 (2003).
http://stacks.iop.org/1367-2630/5/i=1/a=113
(Cited on page 140.)

[210] Y. Nakano, T. Ishima, N. Kobayashi, K. Sakakibara, I. Ichinose, and T. Matsui, "Finite-temperature phase diagram of the three-dimensional hard-core bosonic t-J model," Phys. Rev. B **83**, 235 116 (2011).
http://link.aps.org/doi/10.1103/PhysRevB.83.235116
(Cited on page 140.)

[211] Y. Kuno, K. Kataoka, and I. Ichinose, "Effective field theories for two-component repulsive bosons on lattice and their phase diagrams," Phys. Rev.

B **87**, 014 518 (2013).
http://link.aps.org/doi/10.1103/PhysRevB.87.014518
(Cited on page 140.)

[212] M. Cheneau, P. Barmettler, D. Poletti, M. Endres, P. Schausz, T. Fukuhara, C. Gross, I. Bloch, C. Kollath, and S. Kuhr, "Light-cone-like spreading of correlations in a quantum many-body system," Nature (London) **481**, 484–487 (2012).
(Cited on page 140.)

[213] M. Gring, M. Kuhnert, T. Langen, T. Kitagawa, B. Rauer, M. Schreitl, I. Mazets, D. A. Smith, E. Demler, and J. Schmiedmayer, "Relaxation and Prethermalization in an Isolated Quantum System," Science **337**, 1318–1322 (2012).
http://www.sciencemag.org/content/337/6100/1318.abstract
(Cited on page 140.)

[214] T. Langen, R. Geiger, M. Kuhnert, B. Rauer, and J. Schmiedmayer, "Local emergence of thermal correlations in an isolated quantum many-body system," Nature Physics **9**, 640–643 (2013).
(Cited on page 140.)

[215] T. Kinoshita, T. Wenger, and D. S. Weiss, "A quantum Newton's cradle," Nature **440**, 900–903 (2006).
(Cited on page 140.)

[216] P. Richerme, Z.-X. Gong, A. Lee, C. Senko, J. Smith, M. Foss-Feig, S. Michalakis, A. V. Gorshkov, and C. Monroe, "Non-local propagation of correlations in long-range interacting quantum systems," Nature (London) **511**, 198 (2014).
(Cited on page 140.)

[217] P. Jurcevic, B. P. Lanyon, P. Hauke, C. Hempel, P. Zoller, R. Blatt, and C. F. Roos, "Quasiparticle engineering and entanglement propagation in a quantum many-body system," Nature (London) **511**, 202–205 (2014).
(Cited on page 140.)

[218] Strictly speaking the validity of Eq. 1 also requires $|\Delta - U/2| \gg J^2/\Delta$ and $|\Delta - 3U/2| \gg J^2/|U - \Delta|$, to avoid narrower second order resonances which are associated with double and triple occupancy, respectively.
(Cited on page 141.)

[219] S. Fölling, S. Trotzky, P. Cheinet, M. Feld, R. Saers, A. Widera, T. Müller, and I. Bloch, "Direct observation of second-order atom tunnelling," Nature (London) **448**, 1029–1032 (2007).
(Cited on page 142.)

[220] F. Meinert, M. J. Mark, E. Kirilov, K. Lauber, P. Weinmann, M. Groebner, A. J. Daley, and H.-C. Naegerl, "Observation of many-body dynamics in long-range tunneling after a quantum quench," Science **344**, 1259–1262 (2014). (Cited on page 142.)

[221] See materials and methods. (Cited on pages 142, 143, 144, 146, 147, and 148.)

[222] I. B. Spielman, W. D. Phillips, and J. V. Porto, "Condensate Fraction in a 2D Bose Gas Measured across the Mott-Insulator Transition," Phys. Rev. Lett. **100**, 120 402 (2008). http://link.aps.org/doi/10.1103/PhysRevLett.100.120402 (Cited on page 146.)

[223] I. H. Deutsch and P. S. Jessen, "Quantum-state control in optical lattices," Phys. Rev. A **57**, 1972–1986 (1998). (Cited on page 153.)

[224] S. Gupta, A. E. Leanhardt, A. D. Cronin, and D. E. Pritchard, "Coherent manipulation of atoms with standing light waves," C.R. Acad. Sci. Paris **2**, 1–17 (2001). (Cited on page 154.)